THE UNIVERSITY OF CHICAGO

MULTISCALE METHODS FOR QUANTUM MANY-BODY SYSTEMS

A DISSERTATION SUBMITTED TO
THE FACULTY OF THE DIVISION OF THE PHYSICAL SCIENCES
IN CANDIDACY FOR THE DEGREE OF
DOCTOR OF PHILOSOPHY

DEPARTMENT OF CHEMISTRY

BY

NAN SHENG

CHICAGO, ILLINOIS
DECEMBER 2023

To my family

CONTENTS

LIST OF FIGURES

LIST OF TABLES

ACKNOWLEDGMENTS

I express sincere appreciation to my PhD advisor Prof. Yuehaw Khoo for his helping hand during the hardest period of my life. I express appreciation to my pro forma advisor Prof. Greg Voth, committee member Prof. Aaron Dinner and advisors at the Flatiron Institute Dr. Jason Kaye as well as Dr. Kun Chen for their generous assistance and support.

I express appreciation to Dr. He Ma for his kind tutorship during the early days of my graduate study. I appreciate friendship with Dr. Siyao Yang, Dr. Yian Chen, Dr. Han Yang, Yu Jin, Jiawei Zhan, Zifan Ye, Yinxuan Zhu, and many other.

I express great love to my wife Can Cao, who is also pursuing her PhD in the US, as well as great appreciation to my parents Wen Sheng and Neixin Du who brought me to this world and fed me up.

ABSTRACT

Quantum many-body system is principally a complicated problem with high complexity, where emergent phenomena are hidden behind strong correlations beyond the mean-field. Due to its exponential scaling, direct solution is beyond our ability and multiscale methods provide a natural framework for conquering strong correlations within the system with cost being reduced to an affordable level. In Ch. 1 I will briefly summarize the definition of quantum many-body systems and the ongoing efforts to the problems. After that, I will approach quantum many-body systems from three different aspects: two novel multiscale initialization methods inspired by multigrid method and mean-field theory respectively to solve quantum ground-state problems in Ch. 2, a fast Green's function representation applied to dynamical mean-field theory in Ch. 3, and a novel Green's function embedding framework called quantum defect embedding theory to approach strongly correlated electronic states in solids in Ch. 4. Finally, I will summarize what have been done and propose future steps in Ch. 5. The new methods developed allow a combination of low computational cost and good accuracy, helping people understand novel physical phenomena from their many-body nature.

CHAPTER 1

INTRODUCTION

The behavior of a system composed of a large number of interacting quantum particles is governed by quantum physics. When the system size is small, the quantum equations for the system could be solved exactly. However, when the system size is mid-level or large, the quantum equations become intractable and can no longer be solved exactly, as the quantum complexity grows exponentially w.r.t. the system size, different from the linear scaling of classical physics. Although the exponential scaling is beyond our computational abilities, in many cases the physical essence allow us to treat every single particle as separate within a mean-field medium, and as a result the scaling is greatly reduced but key information is still kept. Famous examples include Hartree-Fock theory (HF), density functional theory (DFT) under its Kohn-Sham implementation [124, 155, 216, 192, 134, 36], the GW method (GW) [9, 94] etc.

However, mean-field approximations are not omnipotent and in general these methods fail when the interactions (attraction, repulsion, correlation), or quantum entanglement between the particles are very strong, *i.e.* where strong interactions exist. These problems are generally called quantum many-body problems. Usually interesting emergent phenomena are originated from and hidden behind these strong correlations, *e.g.* Mott phase transition [126], high-temperature superconductivity [169], spin liquid [346] etc.

Specific strategies and methods need to be implemented to obtain as accurate as possible information from a large-scale but strongly correlated system [195]. Particularly, multiscale methods provide a bridge to keep pivotal information but simultaneously reducing the computational cost to an acceptable level [72]. In applied mathematics, multiscale methods refer to the technique that the systems or computational tasks are separated into different levels of scales, from which we keep information being focused on at a fine level but reducing computational cost at a coarse level. In the case of quantum many-body systems, scientists

have been approaching the problems from different perspectives using multiscale techniques. From wavefunction perspective, the many-body wavefunction of a strongly correlated system is far beyond a single Slater determinant. Apart from including the contributions from high order Slater determinants into many-body Hamiltonian explicitly, *i.e.* the so-called exact diagonalization or configuration interaction [292], scientists design tensor networks as ansatz of the many-body wavefunction to include the high order contributions implicitly. In tensor networks, the many-body interaction is separated into local parts where interactions with other parts are incorporated into tensor contractions. This allows for optimizing local tensors only in a systematic manner until convergence, *i.e.* the so-called density-matrix renormalization group [329, 330, 263, 264]. In this technique people replace solving the full many-body Hamiltonian by solving a group of local optimization problems while keeping descent accuracy. Apart from wavefunction perspective, scientists have been developing quantum embedding methods [289]. As the name suggests, in quantum embedding the full system is separated into two accuracy levels based on either real space or some other strategies such as Feynmann diagrams in Green's function theories, two famous examples of which are many-body perturbation theory (MBPT) [286] and dynamical mean-field theory (DMFT) [82, 81]. For the one we are focusing on a higher level of theory is applied, while for the one we do not care much about a lower level of theory is applied instead. Examples include DFT embedding [173, 95, 96] where a higher level of DFT/wavefunction method is embedded in a lower level of DFT, density-matrix embedding theory [335, 153, 154] where an exact diagonalization is embedded in a Hartree-Fock mean-field, DFT+DMFT [8, 156] where DMFT local diagrams are embedded in a DFT mean-field, and GW+DMFT [24] where DMFT local diagrams are embedded in GW non-local diagrams etc.

In this thesis I aim to develop advanced multiscale methods for a few types of quantum many-body systems. Specifically, I will discuss two tensor network based multiscale initialization method for solving quantum-ground state problems in Ch. 2, low-rank Green's

function applied to dynamical mean-field theory in Ch. 3, and Green's function formulation of quantum defect embedding theory in Ch. 4.

CHAPTER 2

MULTISCALE INITIALIZATION METHODS FOR QUANTUM GROUND-STATE PROBLEMS

2.1 Introduction

Tensor networks [226] provide a mathematical framework for representing and manipulating high-dimensional data structures, such as quantum states in physics [227] or large-scale data in machine learning [53]. They allow for the decomposition of complex structures into a network of simpler tensors connected by edges. Tensor networks enable efficient calculations and extractions of information by contracting or summing over shared indices. One popular type of tensor network is the tensor-train (TT) [228], or matrix product state (MPS) [264], which is particularly useful for describing one-dimensional systems. In combination with density matrix renormalization group (DMRG) [264], which is a numerical method based on tensor networks, primarily used for studying one-dimensional quantum systems, it allows for efficient approximations of ground states and low-lying excited states of quantum systems, especially those with strong correlations. To use DMRG, a TT ansatz is initially given and randomly initialized as the many-body ground state. By optimizing each tensor node of the TT iteratively, DMRG captures the most important correlations while keeping computational costs manageable. DMRG is a powerful tool for understanding strongly correlated systems, such as spin chains or one-dimensional lattice models.

Recently researchers at Chicago proposed a new density estimation framework using tensor networks called tensor sketching [125]. Inspired by the randomized SVD, this technique introduces a group of left and right sketching functions as a tool to capture the row and column information of the tensor respectively, with which an iteration of conpressed equations can be built up for tensor cores and solved based on the density samples. Different from using tensor networks as an ansatz, this technique committed to generating an approximation

tensor network to the true density distribution. So far this technique has been applied to TT [125] as well as the tree tensor network (TTN) [293, 231]. Among these algorithms, one algorithm called hierarchical tensor sketching [231] is particularly interesting. In hierarchical tensor sketching, a hierarchical tree tensor network is aimed for an approximate density and each tensor cores are solved hierarchically from the top node to each layer of the tree until the bottom layer, while the sketching functions are built up based on a set of cluster basis to capture information from the samples.

In this work we focus on building an approximate solution to quantum ground-state problems. Different from density estimation, in this case there is no sampled data as a priori. As such, instead of using sketching functions to capture information from the sampled tensor, *i.e.* the so called tensor sketching, we develop a systematic multiscale initialization framework (MI) including two methods called top-down initialization and bottom-up initialization respectively to construct an approximate solution of the problem in a TTN format. Specifically, the top-down method allows a systematic refinement of the solution using a progressively finer Galerkin space built up from cluster sketch functions at different levels. This strategy follows the same spirit as multigrid methods in solving eigenvalue problems and PDEs. The bottom-up method constructs the solution in the spirit of but as a generalization of mean-field theory. We find that both of the methods are stable and the accuracy is not compromised, even though we choose a small number of basis set at each step.

2.2 Background

In this section, we give a concise summary of background knowledge for our new algorithms. Specifically, we describe our target problem, the quantum ground-state problem in Subsec. 2.2.1, tensor-train representation in Subsec. 2.2.2, tree tensor network representation in Subsec. 2.2.3, and density-matrix renormalization group algorithm in Subsec. 2.2.4.

2.2.1 Quantum ground-state problem as an optimization problem

Mathematically, the quantum ground-state problem is formulated by the following eigenvalue problem, *i.e.*,

$$H\psi = E\psi. \tag{2.1}$$

Here H is the quantum Hamiltonian under a many-body basis. E as well as ψ are its eigenvalue and eigenfunction respectively. We are interested in the lowest eigenvalue and the corresponding eigenvector, which is also the solution of the following optimization problem, *i.e.*,

$$\min_{\psi} \langle \psi, H\psi \rangle, \quad \langle \psi, \psi \rangle = 1. \tag{2.2}$$

2.2.2 Tensor-train representation

For a d-dimensional tensor $\psi : n_1 \times n_2 \times \cdots \times n_d \longrightarrow \mathbb{R}$, a TT/MPS decomposition corresponds to the following low-rank approximation, *i.e.*,

$$\psi(i_1, i_2, \ldots, i_d) \approx \sum_{\alpha_1=1}^{r_1} \sum_{\alpha_2=1}^{r_2} \cdots \sum_{\alpha_{d-1}=1}^{r_{d-1}} G_1(i_1, \alpha_1) G_2(\alpha_1, i_2, \alpha_2) \cdots G_d(\alpha_{d-1}, i_d). \tag{2.3}$$

Here G_k is called the k-th tensor core of the TT/MPS. In Fig. 2.1 we introduce a tensor diagram as a concise representation of the above TT/MPS.

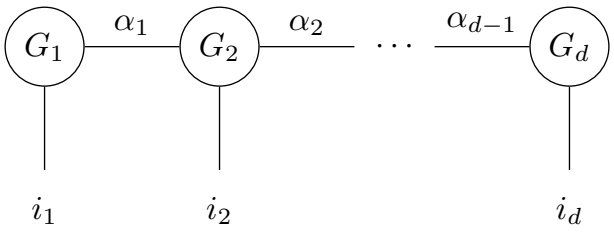

Figure 2.1: Tensor diagram for a matrix product state (MPS). $\{G_k\}_{k=1}^{d}$ corresponds to the d tensor cores. $\{i_k = 1, \ldots, n_k\}_{k=1}^{d}$ corresponds to the d tensor indices. $\{\alpha_k = 1, \ldots, r_k\}_{k=1}^{d-1}$ corresponds to the $d-1$ contraction indices between the tensor cores.

For a $2 \times d$-dimensional tensor $H : n_1 \times n_1' \times n_2 \times n_2' \times \cdots \times n_d \times n_d' \longrightarrow \mathbb{R}$, a MPO decomposition corresponds to the following low-rank approximation, *i.e.*,

$$H(i_1, i_1', i_2, i_2', \ldots, i_8, i_8') \approx \sum_{\alpha_1=1}^{r_1} \sum_{\alpha_2=1}^{r_2} \cdots \sum_{\alpha_{d-1}=1}^{r_{d-1}} G_1(i_1, i_1', \alpha_1) G_2(\alpha_1, i_2, i_2', \alpha_2) \cdots G_d(\alpha_{d-1}, i_d, i_d'). \tag{2.4}$$

Here G_k is called the k-th tensor core of the MPO. In Fig. 2.2 we introduce a tensor diagram as a concise representation of the above MPO.

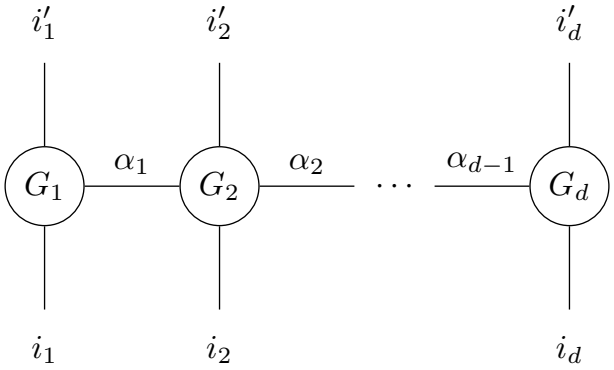

Figure 2.2: Tensor diagram for a matrix product operator (MPO). $\{G_k\}_{k=1}^d$ corresponds to the d tensor cores. $\{i_k = 1, \ldots, n_k\}_{k=1}^d$ and $\{i_k' = 1, \ldots, n_k\}_{k=1}^d$ corresponds to the $2 \times d$ tensor indices. $\{\alpha_k = 1, \ldots, r_k\}_{k=1}^{d-1}$ corresponds to the $d-1$ contraction indices between the tensor cores.

2.2.3 Tree tensor network representation

In general a d-dimensional tensor $\psi : n_1 \times n_2 \times \cdots \times n_d \longrightarrow \mathbb{R}$ can be decomposed into tree-like structure. We denote the number of levels by M. For simplicity, here we discuss a $M = 3$ level specific binary tree tensor network as an example. The low-rank decomposition

of this TTN is

$$\begin{aligned}\psi(i_1, i_2, \ldots, i_8) \approx & \sum_{\alpha_1^1 \alpha_2^1 = 1}^{r_1} \sum_{\alpha_1^2 \alpha_2^2 \alpha_3^2 \alpha_4^2 = 1}^{r_2} G_1^0(\alpha_1^1, \alpha_2^1) \\ & G_1^1(\alpha_1^1, \alpha_1^2, \alpha_2^2) G_2^1(\alpha_2^1, \alpha_3^2, \alpha_4^2) \\ & G_1^2(\alpha_1^2, i_1, i_2) G_2^2(\alpha_2^2, i_3, i_4) G_3^2(\alpha_3^2, i_5, i_6) G_4^2(\alpha_4^2, i_7, i_8).\end{aligned} \tag{2.5}$$

Here G_n^m is the tensor core of TTN with indices (m, n). In Fig. 2.2 we introduce a tensor diagram as a concise representation of this TTN.

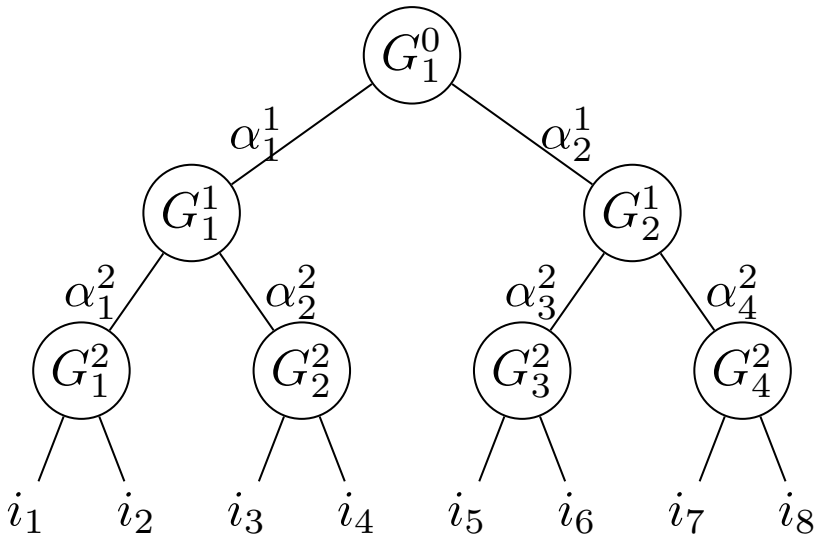

Figure 2.3: Tensor diagram for a tree tensor network (TTN). $\{G_n^m\}$ corresponds to the tensor cores. $\{i_k\}_{k=1}^8$ corresponds to the d tensor indices. $\{\alpha_n^m\}$ corresponds to the contraction indices between the tensor cores.

2.2.4 Density-matrix renormalization group

Under tensor-train representation, the optimization problem in Eq. 2.2 can be denoted by a tensor diagram shown in Fig. 2.4. Instead of optimizing the whole tensor-train, the density-matrix renormalization group (DMRG) aims at optimizing each tensor core sequentially and approach the global minimum after sets of iterations. There are two types of algorithms

called 1-site and 2-site DMRG respectively. In the following we give an example of how 1-site DMRG iterations work, schematically described in Figs. 2.5 and 2.6.

At the beginning each tensor nodes of ψ are randomly initialized. If we minimize over ψ_1 node with other tensor nodes fixed in Fig. 2.4, we can obtain a local eigenvalue problem w.r.t. ψ_1 shown in Fig. 2.5. We note that this step requires that the environment of ψ_1 donoted by R_1 made up of all other nodes of ψ but ψ_1, are orthogonalized and thus ψ is in a form of Schmidt decomposition, *i.e.* $\psi(i_1, \ldots, i_d) = \sum_{\alpha_1=1}^{r_1} \lambda_{\alpha_1} \times \psi_1(i_1, \alpha_1) \times R_1(\alpha_1; i_2, \ldots, i_d)$. Here R_1 satisfies $R_1 R_1' = I$ and can be computed by a pre-orthogonalization process such as a series of RQ decompositions from ψ_d to ψ_2. The lowest eigenvector of the local problem yields newly computed ψ_1.

Similarly, minimization over ψ_2 with other nodes fixed (including the newly computed ψ_1) in Fig. 2.4 leads to a local problem w.r.t. ψ_2, as shown in Fig. 2.6. This step requires that the environment of ψ_2 donoted by E_2 made up of all other nodes of ψ but ψ_2, are orthogonalized and thus ψ is in a form of Schmidt decomposition, *i.e.* $\psi(i_1, \ldots, i_d) = \sum_{\alpha_1=1}^{r_1} \sum_{\alpha_2=1}^{r_2} \lambda_{\alpha_1\alpha_2} \times L_2(i_1; \alpha_1) \times \psi_2(\alpha_1, i_2, \alpha_2) \times R_2(\alpha_2; i_3, \ldots, i_d)$. Here L_1 satisfies $L_1' L_1 = I$ and can be computed by a QR decomposition of ψ_1. R_2 satisfies $R_2 R_2' = I$ and can be computed by a pre-orthogonalization process from ψ_d to ψ_3. The lowest eigenvector of the local problem yields newly computed ψ_2.

Following this procedure, DMRG gradually optimizes each tensor node from left to right (called right sweeping), and from right to left (called left sweeping) until the lowest eigen energy from local eigenvalue problem converges.

2.3 Multiscale initialization methods for quantum ground-state problems

We aim at generating an approximate solution of Eq. 2.2 in TTN format with H in MPO format. First we consider a simple case where H is a matrix and the solution is a vector. Inspired

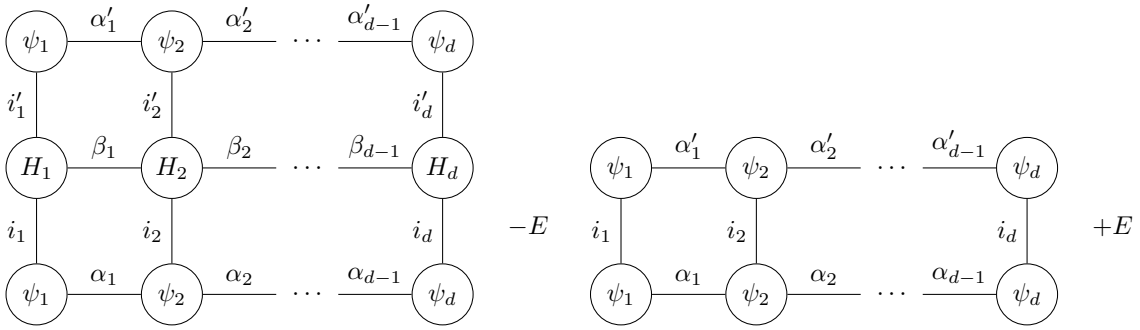

Figure 2.4: Tensor-train format of minimization problem Eq. 2.2. $\{H_i\}_{i=1}^d$ corresponds to the tensor cores of H. $\{\psi_i\}_{i=1}^d$ corresponds to the tensor cores of ψ. $\{i_i\}_{i=1}^d$ and $\{x'_i\}_{i=1}^d$ corresponds to the d tensor indices. $\{\alpha_i\}_{i=1}^{d-1}$, $\{\alpha'_i\}_{i=1}^{d-1}$ and $\{\beta_i\}_{i=1}^{d-1}$ corresponds to the contraction indices between the tensor cores. E denotes the Lagrangian multiplier.

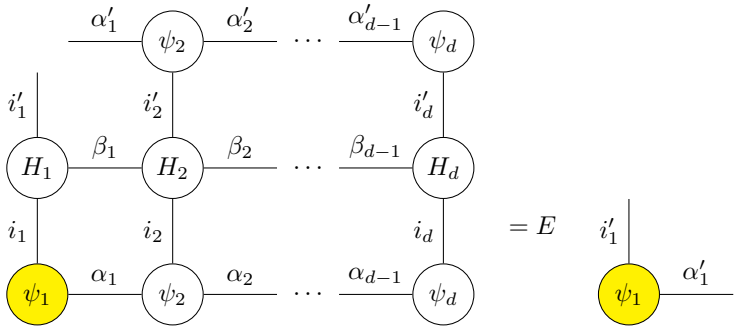

Figure 2.5: Local eigenvalue problem for ψ_1 in DMRG. E is the lowest eigenvalue.

by the randomized SVD algorithm, we can build up approximate local core optimization problems by discretizing H in a way such that the Galerkin space is spanned by a fixed group of basis functions, which are used to capture both row and column space of H.

Supposing Q is the matrix composing of basis functions in its column, we have

$$H \approx QQ'HQQ' = QH^{\text{eff}}Q'. \tag{2.6}$$

Here the approximate equal sign would be strictly established if Q can capture the range space of H completely. By diagonalizing H^{eff} instead of H, we obtain a rough spectral

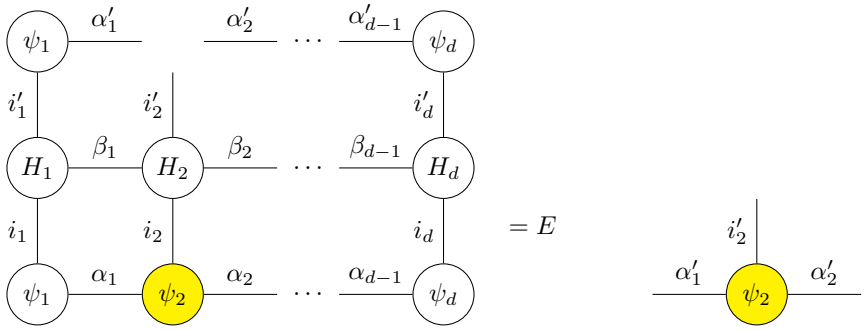

Figure 2.6: Local eigenvalue problem for ψ_2 in DMRG. E is the lowest eigenvalue.

solution of H, *i.e.*,

$$H \approx Q(G'DG)Q' = (GQ')'D(GQ'). \tag{2.7}$$

In principle, we can express the true solution ψ for each TTN tensor node $\{G_n^m\}$ by the following formula, *i.e.*,

$$\psi = Q_n^m G_n^m \coloneqq (C_{2\times n-1}^{m+1} \otimes C_{2\times n}^{m+1} \otimes E_n^m) G_n^m. \tag{2.8}$$

Here Q_n^m denotes the Galerkin matrix contructed for G_n^m, which is further expressed as a tensor product of three parts including two sub-branches $C_{2\times n-1}^{m+1}$ as well as $C_{2\times n}^{m+1}$ and on environment E_n^m. A schematic diagram is presented in Fig. 2.7. In the figure we show that the environment tensor E_n^m contains all information outside of the two sub-branches.

To obtain an approximate G_n^m with low cost, a must do strategy is to obtain approximate $C_{2\times n-1}^{m+1}$, $C_{2\times n}^{m+1}$ and E_n^m tensor nodes with α_n^m, $\alpha_{2\times n-1}^{m+1}$ and $\alpha_{2\times n}^{m+1}$ in low bond dimensions. For this purpose, we can either approximate the two sub-branches, or approximate the environment. In the following two subsections (Subsec. 2.3.1 and 2.3.2), I will present two different algorithms, called top-down initialization and bottom-up initialization respectively, corresponding to the two approximation strategies mentioned above.

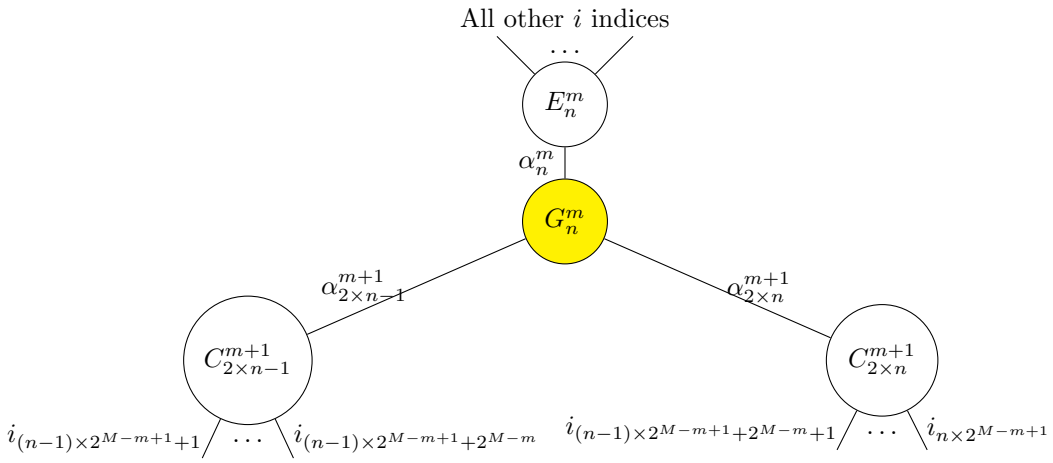

Figure 2.7: Left and right sub-matrices $C_{2\times n-1}^{m+1}$ as well as $C_{2\times n}^{m+1}$ and environment tensor E_n^m for the target node G_n^m. "All other i indices" represents i indices not included in the left and right sketching sub-matrices.

2.3.1 Top-down initialization

Considering that the root node G_1^0 has no environment, we can generate an approximate tree from the root to the leaves with the two sub-branches approximated for each node, *i.e.*,

$$C_n^m \approx S_n^m. \tag{2.9}$$

Here S_n^m is called a sketching matrix. We note that the two sketching matrices are aimed at reducing the global degrees of freedom, the left of which is reduced from $n^{2^{M-m}}$ (assuming $n_1 = n_2 = \ldots = n_d = n$) to $\alpha_{2\times n-1}^m$ under $S_{2\times n-1}^m$ and the right of which is reduced from $n^{2^{M-m}}$ to $\alpha_{2\times n}^m$ under $S_{2\times n}^m$.

We use a graphic figure shown in Fig. 2.8 to illustrate the definition of a sketching matrix S_n^m. The corresponding MPO fragment of S_n^m is denoted by $\tilde{H}_n^m$. From the figure we see that S_n^m can be defined in a way that some specific sequences of indices of $\tilde{H}_n^m$ are kept and the others are ignored. The contraction of S_n^m and $\tilde{H}_n^m$ yields a four-dimension tensor ($\beta_{l-1} = 1$ if $l = 1$ and $\beta_r = 1$ if $r = d$). Essentially, we use S_n^m to keep only a set of the indices and

reduce the dimension subsequently.

Below we give a few examples on how sketching matrices can be defined. The first example is called k-cluster sketching matrix, which keeps the k-cluster basis only, *i.e.* all k-combinations from $r - l + 1$ indices and fixing all other indices to be 1, from all basis. As such, $\alpha_n^m = \alpha'^m_n = C(n,k) \times n^2$ (assuming $n_1 = n_2 = \ldots = n_d = n$). Here $C(n,k)$ is the binomial coefficient. As an example, the 1-cluster sketching matrix keeps the following sequences, which reads

$$\begin{aligned}
&\tilde{H}_n^m(\beta_{l-1}, i_l, i'_l, 1, 1, \ldots, 1, 1, \beta_r) \\
&\qquad \text{where } i_l, i'_l = 1, \ldots, n_l, \\
&\tilde{H}_n^m(\beta_{l-1}, 1, 1, i_{l+1}, i'_{l+1}, \ldots, 1, 1, \beta_r) \\
&\qquad \text{where } i_{l+1}, i'_{l+1} = 1, \ldots, n_{l+1}, \\
&\ldots \\
&\tilde{H}_n^m(\beta_{l-1}, 1, 1, 1, 1, \ldots, i_r, i'_r, \beta_r) \\
&\qquad \text{where } i_{r-1}, i'_{r-1} = 1, \ldots, n_{r-1}.
\end{aligned} \tag{2.10}$$

Another example is called nearest-neighbor sketching matrix, which keeps the nearest-neighbor 2-cluster basis only from from all basis. As such, the following sequences of indices

of $\tilde{H}_n^m$ is kept, *i.e.*,

$$\begin{aligned}
&\tilde{H}_n^m(\beta_{l-1}, i_l, i'_l, i_{l+1}, i'_{l+1}, 1, 1, 1, 1, \ldots, 1, 1, 1, 1, \beta_r) \\
&\qquad \text{where } i_l, i'_l = 1, \ldots, n_l, \text{ and } i_{l+1}, i'_{l+1} = 1, \ldots, n_{l+1}, \\
&\tilde{H}_n^m(\beta_{l-1}, 1, 1, i_{l+1}, i'_{l+1}, i_{l+2}, i'_{l+2}, 1, 1, \ldots, 1, 1, 1, 1, \beta_r) \\
&\qquad \text{where } i_{l+1}, i'_{l+1} = 1, \ldots, n_{l+1}, \text{ and } i_{l+2}, i'_{l+2} = 1, \ldots, n_{l+2}, \\
&\tilde{H}_n^m(\beta_{l-1}, 1, 1, 1, 1, i_{l+2}, i'_{l+2}, i_{l+3}, i'_{l+3}, \ldots, 1, 1, 1, 1, \beta_r) \\
&\qquad \text{where } i_{l+2}, i'_{l+2} = 1, \ldots, n_{l+2}, \text{ and } i_{l+3}, i'_{l+3} = 1, \ldots, n_{l+3}, \\
&\ldots \\
&\tilde{H}_n^m(\beta_{l-1}, 1, 1, 1, 1, 1, 1, 1, 1, \ldots, i_{r-1}, i'_{r-1}, l_r, l'_r, \beta_r) \\
&\qquad \text{where } i_{r-1}, i'_{r-1} = 1, \ldots, n_{r-1}, \text{ and } i_r, i'_r = 1, \ldots, n_r.
\end{aligned} \tag{2.11}$$

As a result, $\alpha_n^m = \alpha'^m_n = (r-l) \times n^2$ (assuming $n_1 = n_2 = \ldots = n_d = n$).

For simplicity we consider a 3-level binary tree network as an example where $L = 3$ and $d = 2^L = 8$. In Fig. 2.9 we show a representation of the approximate solution ψ using G_1^0 and its two sketching sub-matrices, *i.e.*,

$$\psi = Q_1^0 G_1^0 \approx (S_1^1 \otimes S_2^1) G_1^0. \tag{2.12}$$

We can obtain G_1^0 by solving the core determining equation (CDE), *i.e.* a local eigenvalue problem similar to that in DMRG,

$$(S_1^1 \otimes S_2^1)^T H (S_1^1 \otimes S_1^2) G_1^0 \coloneqq H_1^0 G_1^0 = E G_1^0. \tag{2.13}$$

Similarly, we can obtain a an iterative set of CDEs using H as well as sketching functions for the second level G_1^1 and G_2^1 and the third level G_1^2, G_2^2, G_3^2 as well as G_4^2. The corresponding graphics of ψ are shown in Fig. 2.10 and Fig. 2.11 respectively. Accordingly, each core

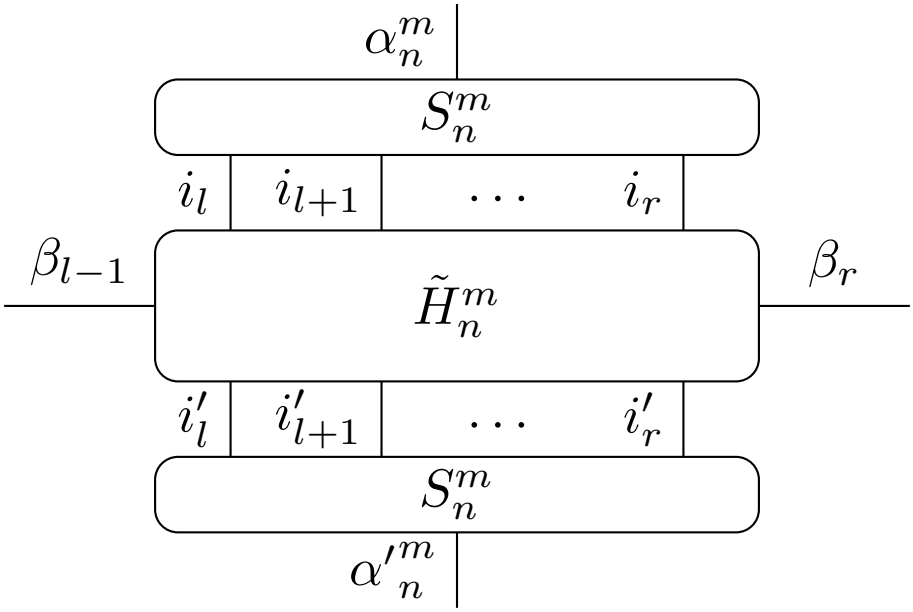

Figure 2.8: Dimension reduction of MPO fragment $\tilde{H}_n^m$ by sketching sub-matrix S_n^m. $\beta_{l-1}, i_l, i'_l, i_{l+1}, i'_{l+1}, \ldots, i_r, i'_r, \beta_r$ are tensor indices of $\tilde{H}_n^m$. $\beta_{l-1}, \alpha_n^m, \alpha'^m_n, \beta_r$ are new tensor indices after dimension reduction by S_n^m.

determining equations is a local eigenvalue problem, *i.e.*,

$$H_n^m G_n^m = E G_n^m. \tag{2.14}$$

Here H_n^m is the local Hamiltonian where $S_{2\times n-1}^{m+1}$, $S_{2\times n}^{m+1}$ and E_n^m have been contracted with the global H. This procedure is exactly the same as that in density-matrix renormalization group (DMRG) algorithm. G_n^m corresponds to the lowest eigenvector of this local problem.

By solving these equations hierarchically and iteratively, we can finally obtain a full TTN as an approximation to ψ. This procedure resembles multigrid method to extract more information from finer and finer grid at each level and obtain the final result at the last step. For this reason, we expect that the lowest eigenvalue from Eq. 2.14 decreases monotonically after each CDE step. Also, we expect that the results would be better when increasing the size of basis set, such as replacing 1-cluster basis by 2-cluster basis.

It is noteworthy that at each step we can keep all nodes but the one to be determined orthogonal using QR as well as RQ techniques, and we can use SVD to reduce the dimension of each node, *i.e.* α_n^m, after solving each CDE.

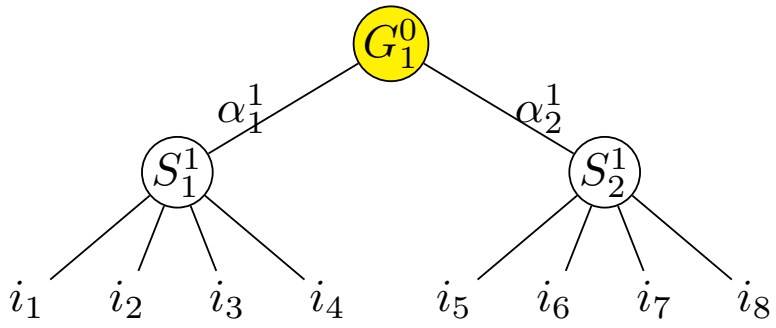

Figure 2.9: Approximate wavefunction ψ for the first level. Target node G_1^0 is marked yellow.

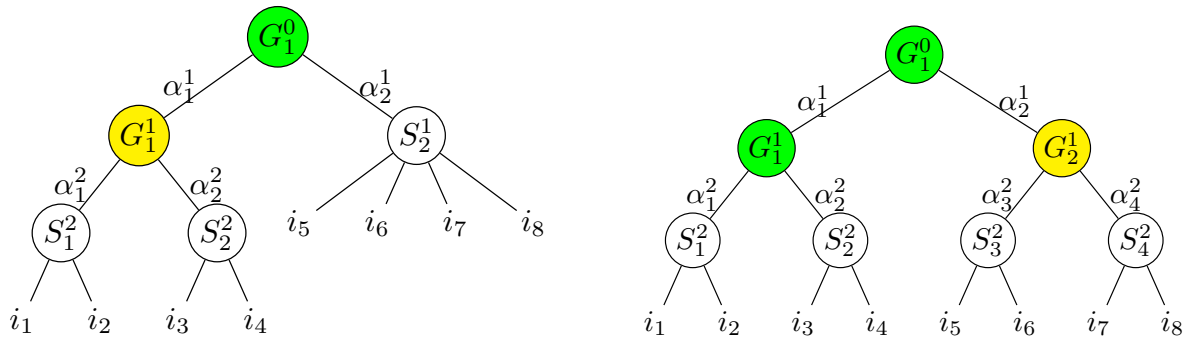

Figure 2.10: Approximate wavefunction ψ for the second level. Nodes marked yellow are to be determined. Nodes marked green are known.

2.3.2 Bottom-up initialization

Considering that the sub-branches of leaf nodes are known, we can generate an approximate tree from bottom to up with the environment approximated for each node, *i.e.*,

$$E_n^m \approx S_n^m. \tag{2.15}$$

Here sketching sub-matrix S_n^m is aimed at reducing the environment degrees of freedom to α_n^m. For simplicity again we consider a 3-level binary tree network. In Fig. 2.12 we show a representation of the approximate solution ψ using each of the leaf nodes and the corresponding sketching sub-matrices. For instance, the formula for G_1^2 node is given by

$$\psi = Q_1^2 G_1^2 \approx S_1^2 G_1^2, \tag{2.16}$$

and the corresponding CDE is given by

$$S_1^2 H S_1^2 G_1^2 \coloneqq H_1^2 G_1^2 = E G_1^2. \tag{2.17}$$

Similarly, we can obtain a an iterative set of CDEs using H as well as sketching functions

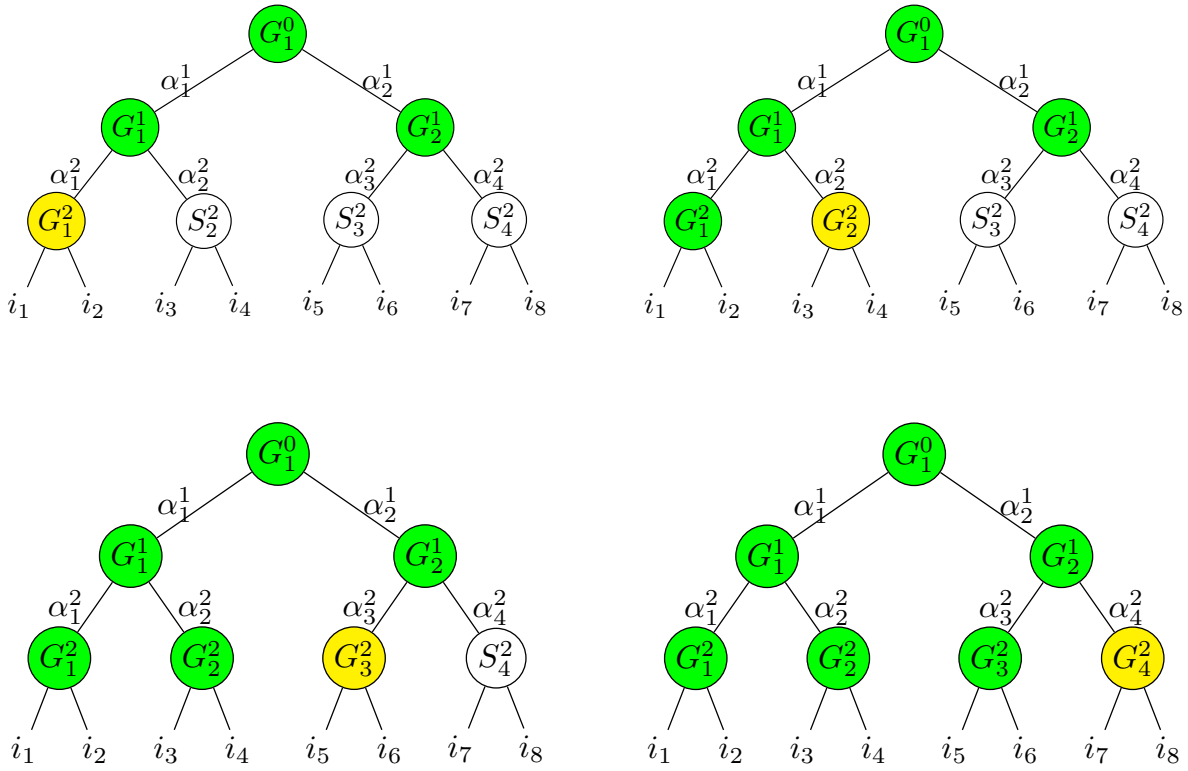

Figure 2.11: Approximate wavefunction ψ for the third level. Nodes marked yellow are to be determined. Nodes marked green are known.

for the other leaf nodes, the second level G_1^1 and G_2^1 and the first level G_1^0. The corresponding graphics of ψ are shown in Fig. 2.13 and Fig. 2.14 respectively. Accordingly, each core determining equations is again a local eigenvalue problem defined in Eq. 2.14 but H_n^m is the local Hamiltonian where $C_{2\times n-1}^{m+1}$, $C_{2\times n}^{m+1}$ and S_n^m have been contracted with the global H.

Again, after solving each local problems iteratively, we can obtain a full TTN as an approximation to ψ. Different from top-down algorithm, in this approach there does not exist a gradual Galerkin space expansion. The full Galerkin space expanded by the MPO would be completely used after solving all leaf nodes. As such, instead of expecting a gradual refinement of eigenvalue we expect that the lowest eigenvalue would be relatively stable after solving the last leaf node. Similarly, we expect that the results would be better when

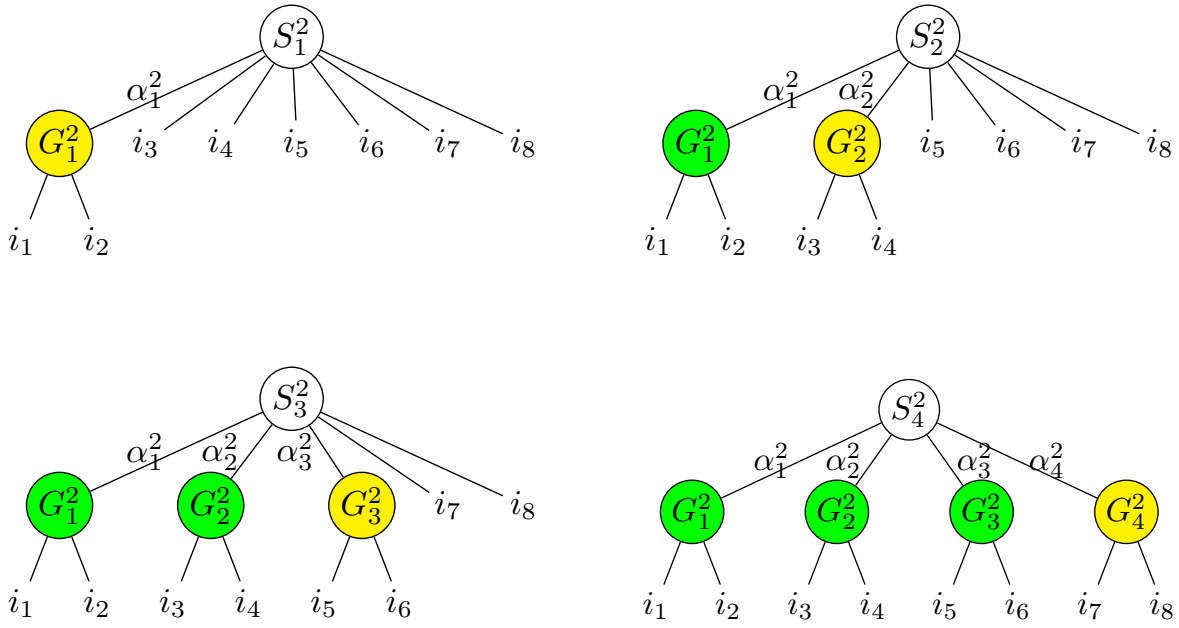

Figure 2.12: Approximate wavefunction ψ for the third level. Nodes marked yellow are to be determined. Nodes marked green are known.

increasing the size of basis set only for the leaf nodes.

2.4 Numerical examples

2.4.1 1D transverse-field Ising model

In this section, we benchmark the accuracy and complexity of the method using periodic 1D transverse-field Ising model (1D-TFI), *i.e.*,

$$H_{\text{1D-TFI}} = g\sum_{i=1}^{d}\sigma_x^i + J(\sum_{i=1}^{d-1}\sigma_z^i\sigma_z^{i+1} + \sigma_z^d\sigma_z^1). \tag{2.18}$$

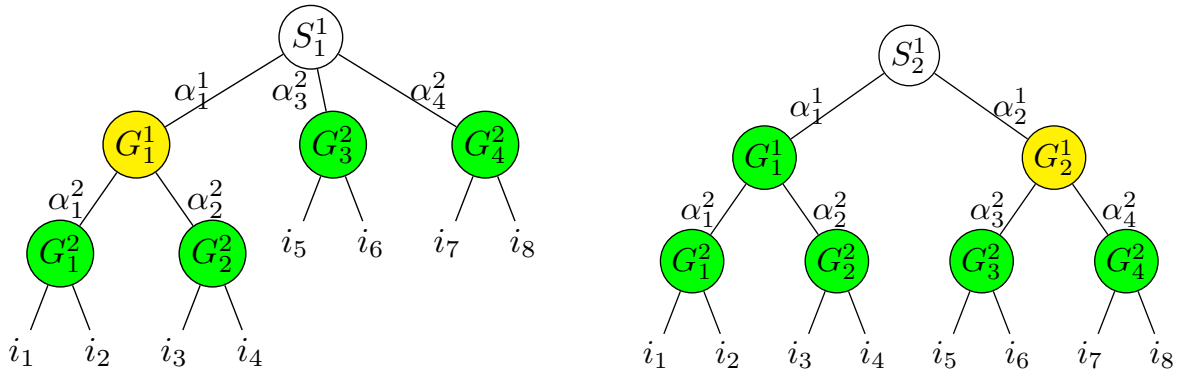

Figure 2.13: Approximate wavefunction ψ for the second level. Nodes marked yellow are to be determined. Nodes marked green are known.

Here σ_x^i and σ_z^i are Pauli matrices for the i-th site on the x and z directions respectively, where

$$\sigma_x = \begin{pmatrix} 0 & 1 \\ 1 & 0 \end{pmatrix}, \sigma_y = \begin{pmatrix} 0 & -i \\ i & 0 \end{pmatrix}, \sigma_z = \begin{pmatrix} 1 & 0 \\ 0 & -1 \end{pmatrix}. \tag{2.19}$$

MPO is built up using the finite automata method [264].

We note that our experiments show that 1-cluster sketching basis is good enough to produce converged results w.r.t. the set of basis set. As such, below we present results obtained from 1-cluster sketching matrices. Besides, we use exact diagonalization to solve CDEs and fix all bond dimensions within the TTN to be 2.

In Fig. 2.15 we show the energy per site (lowest eigenvalue divided by the number of sites) for a 32-site system after determining each tensor core from Eq. 2.14. We can see that the lowest eigenvalue from the top-down algorithm is gradually decreasing, in accordance with the Galerkin space expansion. Besides, it is noteworthy that the curve is composed of 5 linear segments, corresponding to the 5 layers of the TTN. The lowest eigenvalue from bottom-up is gradually decreasing before reaching a plateau until the 16^{th} step corresponding to the last leaf node. This also meets our expectation of the algorithm.

In Fig. 2.16 we show the comparison of the energy per site from MI (both top-down and

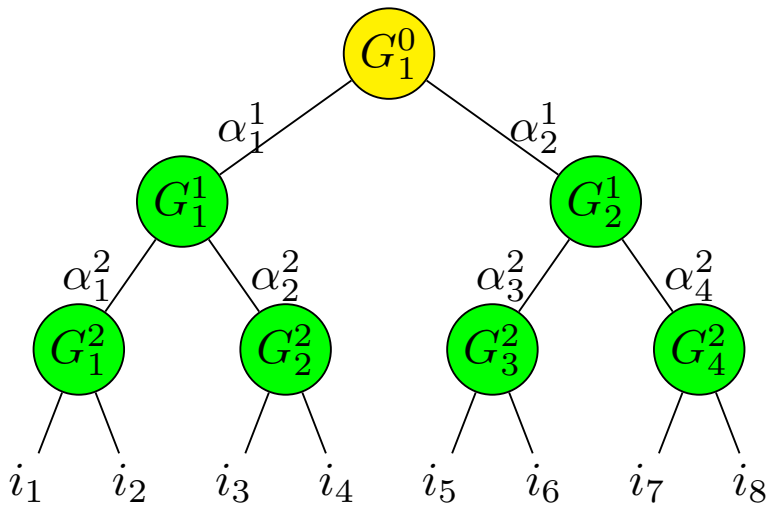

Figure 2.14: Approximate wavefunction ψ for the first level. Target node G_1^0 is marked yellow.

bottom-up), DMRG (both 1-site and 2-site) and analytical method for a 32-site system with different magnetic fields (g). In DMRG calculations we also set MPS bond dimensions to be 2. We can see that the values obtained from MI are close to those obtained from analyatical method and DMRG.

In Fig. 2.17 we show the comparison of eigenvalues from MI (both top-down and bottom-up), DMRG and analytical method at the critical point ($J = g = 1$) with different number of sites. From here we can see that DMRG produces data very close to true values, indicating excellent performance for 1D system. Results converge quickly at around 32 sites. Although discrepancies exist between results from MI and true values, the results are not bad. The discrepancy can be understood from the insufficiency of basis set using MI, especially at large system size.

In Tab. 2.1 we show the overlap between the final wavefunction from MI and true wavefunction from exact diagonalization for a 8-site system and a 12-site system respectively. Here we also consider the critical point. From the figure we learn that the overlap is generally around 70%, close to the results from DMRG. This indicates considerable accuracy and

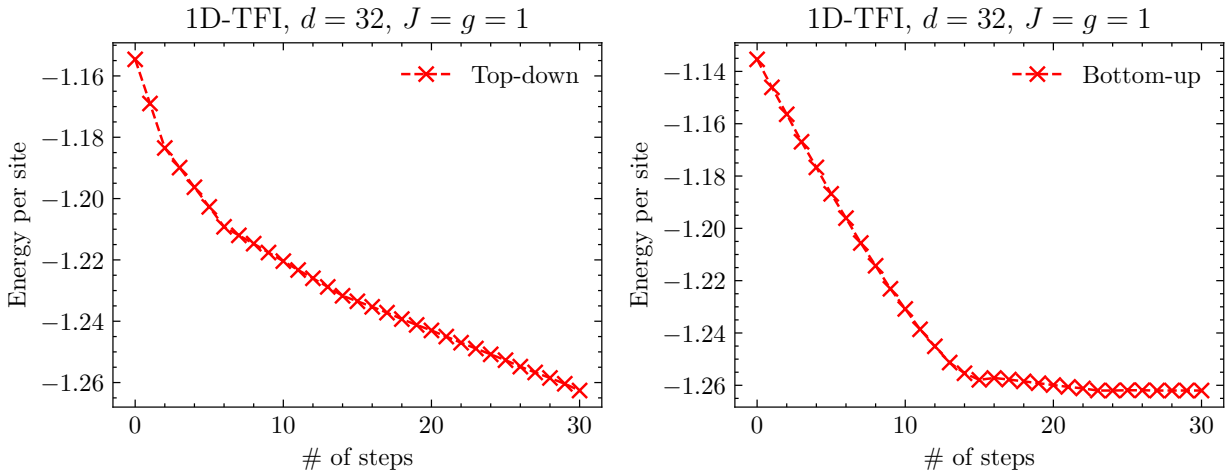

Figure 2.15: Energy per site (lowest eigenvalue divided by the number of sites) obtained from Eq. 2.14 after solving each core determining equation for a 32-site 1D transverse-field Ising model using the top-down algorithm (left figure) and the bottom-up algorithm (right figure). We set $J = g = 1$ in Eq. 2.18, which is also the most challenging case, corresponding to the critical point of this model. There exist 4 levels for a 32-site model. Thus, the total number of sites is $1 + 2 + 4 + 8 + 16 = 31$.

quality of the final eigenvector.

	$d = 8$	$d = 12$
1-site DMRG	0.7520	0.7308
2-site DMRG	0.7532	0.7320
top-down	0.7101	0.6727
bottom-up	0.7079	0.6631

Table 2.1: Overlap between the final wavefunction from MI (both top-down and bottom-up) and the true wavefunction from exact diagonalization for a 8-site and a 12-site 1D transverse-field Ising model respectively. We set $J = g = 1$ in Eq. 2.18. The results are compared with those from DMRG.

2.4.2 Stationary Fokker-Planck equation

In this section, we benchmark the accuracy and complexity of the method by solving a high-dimensional stationary Fokker-Planck equation (FP). FP is originally a PDE in the following form, *i.e.*,

$$L\rho = 0, \quad \rho \geq 0, \quad \int \rho(\mathbf{x}) \mathrm{d}\mathbf{x} = 1. \tag{2.20}$$

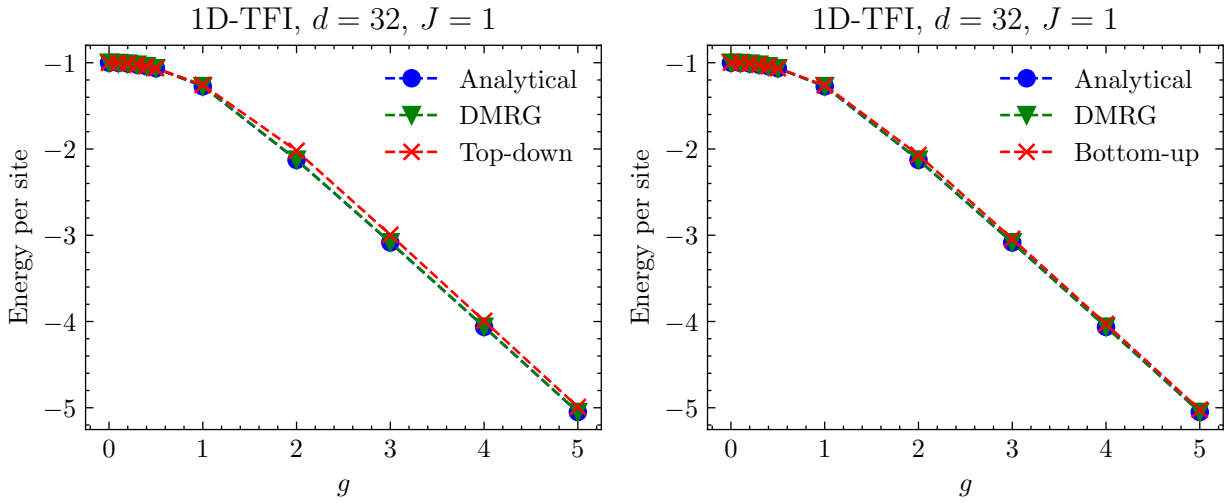

Figure 2.16: Final Energy per site obtained from MI (top-down on the left and bottom-up on the right), DMRG and analytical method for a 32-site periodic 1D-TFI with different magnetic fields. We set $J = 1$ in Eq. 2.18.

L is called Fokker-Planck operator, which is defined by

$$L = \frac{1}{T}\nabla^2 + \nabla V \cdot \nabla + \nabla^2 V. \tag{2.21}$$

Here T is the temperature and $V \in C^2(\mathbb{R}^d)$ is a smooth confining potential. L is a real non-positive operator in $C_0^2(\mathbb{R}^d) \cap L^2(\mathbb{R}^d; \rho_\beta^{-1})$. For this reason, finding the solution of Eq. 2.21 is equivalent to solving the following eigenvalue problem, *i.e.*,

$$\min_{\rho} \langle \rho, -L\rho \rangle, \quad \langle \rho, \rho \rangle = 1. \tag{2.22}$$

It is straightforward to verify that the equilibrium density distribution $\rho_\beta = e^{-\beta V}$ is the solution of Eq. 2.20. More importantly, ρ_β is the only vector in the null space of L and serves as the ground truth of the problem Eq. 2.22.

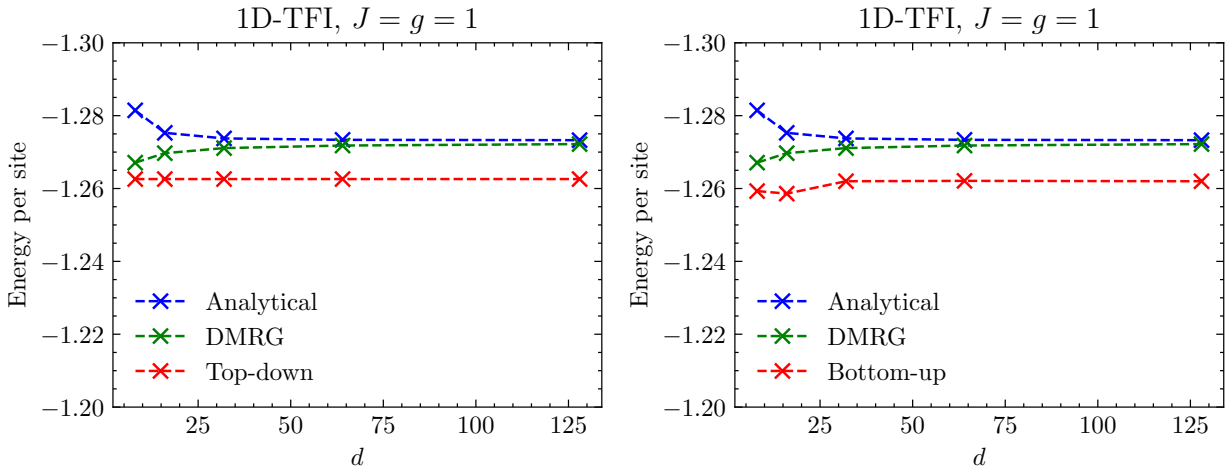

Figure 2.17: Final Energy per site obtained from MI (top-down on the left and bottom-up on the right), DMRG and analytical method for periodic 1D-TFI with different number of sites. We set $J = g = 1$ in Eq. 2.18.

Double well potential In this work we fix $T = 1$, and test a simple case where V is completely separable, *i.e.*,

$$V = V_1 \otimes V_2 \otimes V_2 \otimes \ldots \otimes V_2. \tag{2.23}$$

Here $V_1(x) = (x^2 - 1)^2$ and $V_2(x) = 3x^2$. Accordingly, L can be written in the following form, *i.e.*,

$$L = L_1 \otimes I \otimes \ldots \otimes I + I \otimes L_2 \otimes \ldots \otimes I + \ldots + I \otimes I \otimes \ldots \otimes L_2. \tag{2.24}$$

Here $L_1 = \beta \frac{\mathrm{d}^2}{\mathrm{d}x^2} + \frac{\mathrm{d}V_1}{\mathrm{d}x}\frac{\mathrm{d}}{\mathrm{d}x} + \frac{\mathrm{d}^2 V_1}{\mathrm{d}x^2}$ and $L_2 = \beta \frac{\mathrm{d}^2}{\mathrm{d}x^2} + \frac{\mathrm{d}V_2}{\mathrm{d}x}\frac{\mathrm{d}}{\mathrm{d}x} + \frac{\mathrm{d}^2 V_2}{\mathrm{d}x^2}$. Since x is a continuous extended variable, numerically we fix the space to be $[-2, 2]$ for each dimension, discretize L_1 and L_2 using the top 20 eigenfunctions of Laplace operator with Dirichlet boundary conditions on the space in the spirit of spectral method, and build up L using the finite automata method.

Similar to 1D-TFI case, here we adopt 1-cluster sketching basis. We use exact diagonalization to solve CDEs and fix all bond dimensions within the TTN to be 2. Also, we note that to reduce the computational cost we control every environment indices to be 2 in the

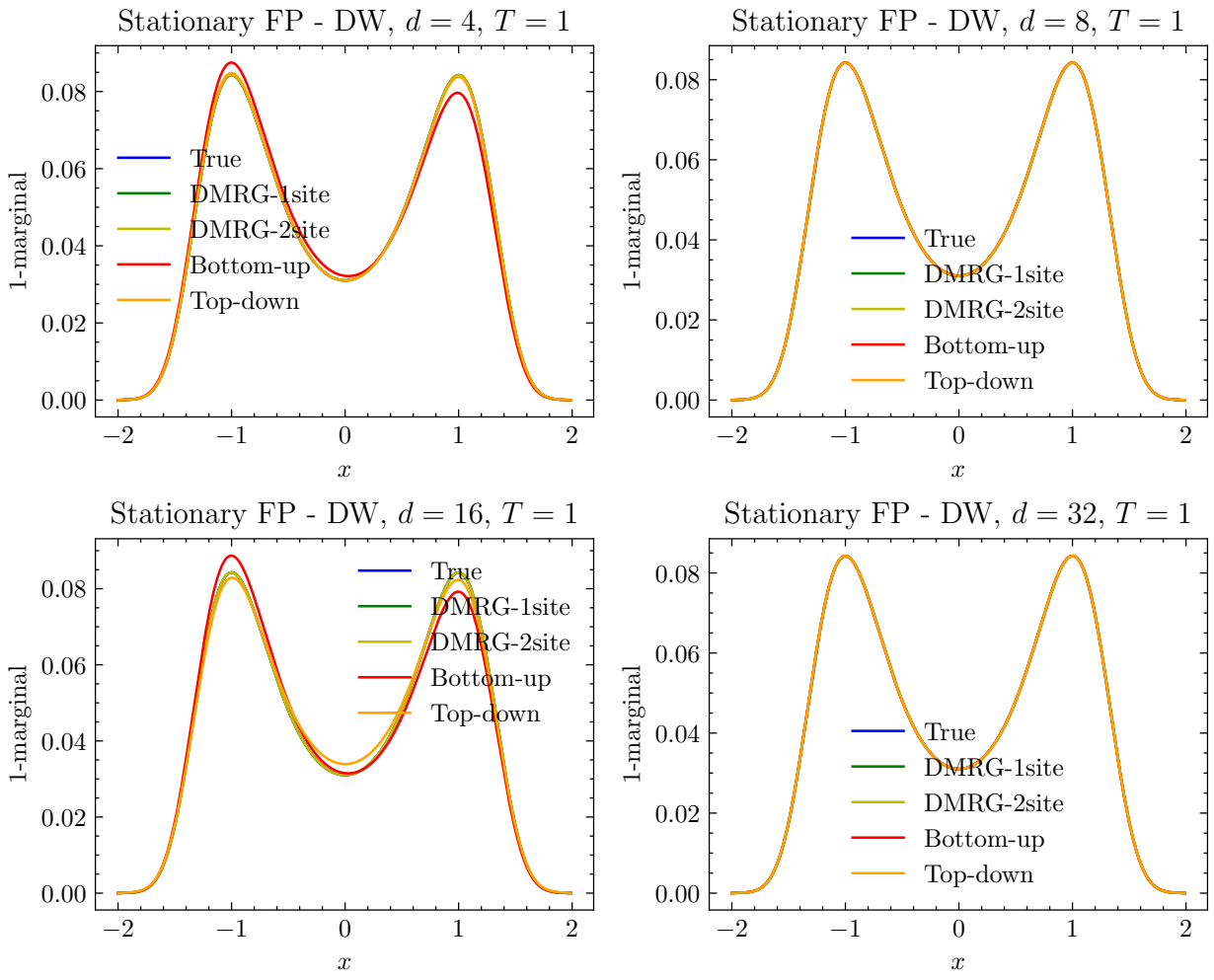

Figure 2.18: 1-marginal obtained from MI, DMRG and analytical method for stationary Fokker-Planck equation with double well potential.

bottom-up algorithm when building up local problems. For example, the sketching matrix S_1^2 shown in first subplot of Fig. 2.12 only selects indices where $i_3, i_4, \ldots, i_8 \in \{1, 2\}$, *i.e.* the first 2 basis functions.

In Fig. 2.18 we show the comparison of 1-marginal of the solution ρ, which is defined by $\int \rho(x_1, x_2, \ldots, x_d) \mathrm{d}x_2 \ldots \mathrm{d}x_d$, between ground truth, DMRG (both 1-site and 2-site), and MI (both top-down and bottom-up) with four different dimensions $d = 4, 8, 16, 32$. From the figures we see although some discrepancies appear in $d = 4$ and $d = 16$ cases, in general MI produces data very close to ground truth and DMRG, indicating excellent performance.

Ginzburg-Landau potential The Ginzburg-Landau theory (GL) was developed to provide a mathematical description of superconductivity [123]. In GL theory, V has the following form

$$V(x_1, x_2, \ldots, x_d) = \sum_{i=1}^{d+1} \frac{\lambda}{2}(\frac{x_i - x_{i-1}}{h}) + \frac{1}{4\lambda}(1 - x_i^2)^2, \tag{2.25}$$

with boundary conditions $x_0 = x_{d+1} = 0$. We fix $T = 1$, $h = 1/(d+1)$ and $\lambda = 0.03$. We take the exact discretization as well as the computational setup to the double well case.

Same to double well case, we fix the space to be $[-2, 2]$ for each dimension, discretize L_1 and L_2 using the top 20 eigenfunctions of Laplace operator with Dirichlet boundary conditions on the space in the spirit of spectral method, and build up L using the finite automata method.

In Fig. 2.19 we show the comparison of 1-marginal for this system. We use 1-marginal computed from DMRG-cross algorithm [258] as an approximation to the ground truth. From the figures we see that different from double well case, DMRG encounters difficulties finding true solution of this system. On the contrary, MI still performs outstandingly well. The example shows the bottleneck of DMRG and an exceptional advantage of MI.

2.5 Conclusion

In this work we propose two multiscale initialization methods top-down and bottom-up for quantum ground-state problems (large-scale eigenvalue problems). The proposed methods follow the spirit of multigrid method and mean-field theory respectively. We demonstrate the accuracy of the methods using 1D periodic transverse-field Ising model and stationary Fokker-Planck equation. In general, our results suggest that multiscale initialization method can be used to solve eigenvalue problems to certain accuracy. Also, our results on high-dimensional stationary Fokker-Planck equation with Ginzburg-Landau potential indicates that density-matrix renormalization group faces difficulties in certain high-dimensional problems

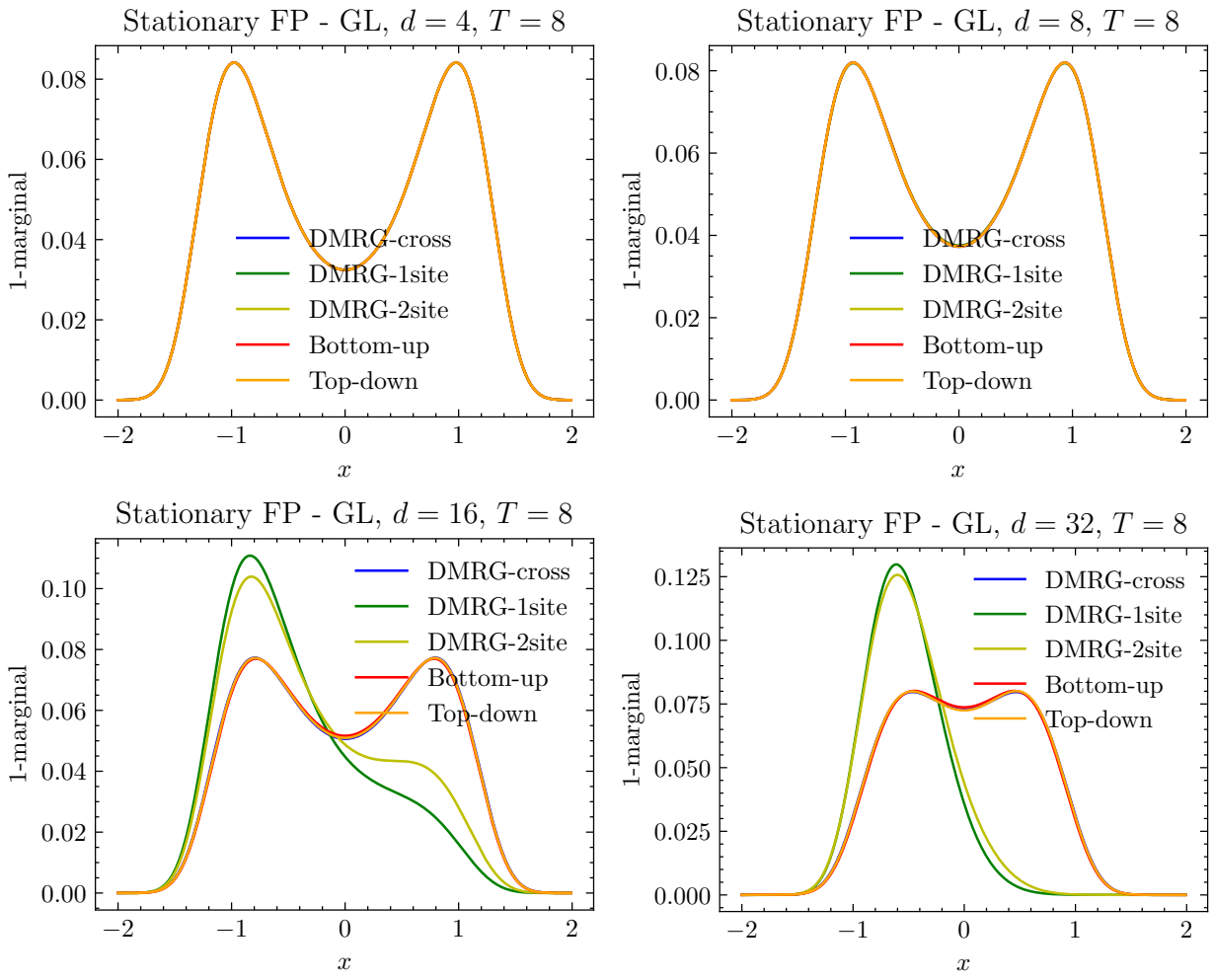

Figure 2.19: 1-marginal obtained from MI, DMRG and analytical method for stationary Fokker-Planck equation with Ginzburg-Landau potential.

and the new methods proposed are advantageous. We believe that the algorithms have broader prospects in 2D/3D problems and can be very promising in solving high-dimensional partial differential equations.

CHAPTER 3

LOW-RANK GREEN'S FUNCTION REPRESENTATIONS APPLIED TO DYNAMICAL MEAN-FIELD THEORY

This chapter was previously published as Ref. 272.

3.1 Introduction

In the past several decades, dynamical mean-field theory (DMFT) [83] has become a standard method for studying interacting fermionic lattice problems. In combination with first-principles methods [156, 114], it has been widely adopted to calculate properties of strongly correlated materials. In such DMFT calculations of real materials, the low temperature regime is of particular importance, as numerous experimental examples show: the critical temperature T_C for superconductivity in Sr_2RuO_4 is as low as approximately $1.5\,K \approx 10^{-4}$eV [182]; the magnetic ordering in double-perovskite iridates sets is below $2\,K$ [294]. In these cases, the ordering temperature energy scale differs by about five orders of magnitude from the high energy cutoff of approximately $10\,eV$.

The single-particle Green's function, a central quantity in DMFT, is often calculated in the imaginary time or Matsubara frequency domain. The standard representation on an equispaced grid in imaginary time, or on Matsubara frequencies up to a cutoff, is low-order accurate, and requires

$$N = \mathcal{O}\left(\beta\omega_{\max}\right) \tag{3.1}$$

degrees of freedom. Here, β is the inverse temperature, and $\omega_{\max}$ is the high energy cutoff of the spectral function (i.e., $\rho(\omega) = 0$ outside $[-\omega_{\max}, \omega_{\max}]$). In typical DMFT calculations, computing the local Green's function requires a possibly expensive Brillouin zone (BZ) integration for each Matsubara frequency grid point and each iteration of a self-consistency loop determining the chemical potential. This cost can become substantial as the temperature

is decreased.

A significant research effort has recently focused on developing compact and generic representations of imaginary time and Matsubara frequency Green's functions, beginning with orthogonal polynomial bases [26, 138, 103, 67] and adaptive grid representations in imaginary time [161, 138]. More recently, optimized basis sets obtained from low-rank compression of the Lehmann integral representation have been developed, along with associated stable interpolation grids allowing recovery of Green's functions from a small number of samples in either the imaginary time or Matsubara frequency domains. This began with the introduction of the orthogonal intermediate representation (IR) basis [275, 48]. Interpolation grids for the IR were later developed using the sparse sampling method [170]. Recently, some of the authors introduced the DLR [143], which uses a non-orthogonal but explicit basis of exponentials, with associated DLR interpolation grids. Both the IR and DLR bases, and their interpolation grids, contain only

$$N = \mathcal{O}\left(\log(\beta\omega_{\max})\log\left(\epsilon^{-1}\right)\right) \tag{3.2}$$

degrees of freedom, with ϵ a user-provided error tolerance. They therefore yield exceptionally compact representations with controllable, high-order accuracy. Fortran, Python, and Julia libraries are available for both the IR with sparse sampling [314] and the DLR [144]. Low-rank Green's function representations have been used to solve self-consistent diagrammatic equations in a variety of applications, including the SYK model [143, 144, 145], the self-consistent finite temperature GW method [170, 338], Eliashberg-type equations for superconductivity [319, 38, 318, 214], and Bethe-Salpeter-type equations for Hubbard models [316].

In this work we investigate the applicability and robustness of the DLR in self-consistent DMFT calculations. Specifically, we replace the standard Matsubara frequency grid with the compact DLR grid in the calculation of the local Green's function and all subsequent expressions in the DMFT equations. We find that this method is stable, even in the

presence of noisy Green's function data as obtained from continuous-time quantum Monte Carlo (CTQMC) impurity solvers, and that neither the convergence nor the accuracy of self-consistent iteration is compromised. We demonstrate a reduction in computational effort and memory required to calculate the local Green's function by over two orders of magnitude for the correlated Hund's metal Sr_2RuO_4 at $T = 50\,\mathrm{K}$. Although the expensive solution of the impurity problem remains a barrier in many DMFT calculations, our approach therefore dramatically reduces the other significant cost in the DMFT loop, and leads to a more automated procedure.

3.2 Background

3.2.1 The dynamical mean-field theory loop

We briefly outline the DMFT equations, and refer the reader to Refs. [83, 156] for a more comprehensive overview. The central quantity of interest is the local Green's function,

$$G_{\mathrm{loc}}(i\nu_n) = \int_{\mathrm{BZ}} \frac{d\mathbf{k}}{V_{\mathrm{BZ}}} \left[i\nu_n - \epsilon_{\mathbf{k}} + \mu - \Sigma(\mathbf{k}, i\nu_n)\right]^{-1}. \tag{3.3}$$

Here $i\nu_n = i(2n+1)\pi/\beta$ is the Matsubara frequency variable (for fermionic Green's functions), $\epsilon_{\mathbf{k}}$ is the non-interacting lattice Hamiltonian, μ is the chemical potential, $\Sigma(\mathbf{k}, i\nu_n)$ is the lattice self-energy, and V_{BZ} is the volume of the BZ. The chemical potential can be computed self-consistently in each DMFT iteration in order to maintain the correct particle density. In DMFT, the self-energy is approximated as a local quantity, and is computed from the Green's function $G_{\mathrm{imp}}(i\nu_n)$ of an effective impurity problem via the Dyson equation

$$\Sigma(\mathbf{k}, i\nu_n) \approx \Sigma_{\mathrm{imp}}(i\nu_n) = \mathcal{G}_0^{-1}(i\nu_n) - G_{\mathrm{imp}}^{-1}(i\nu_n)\,. \tag{3.4}$$

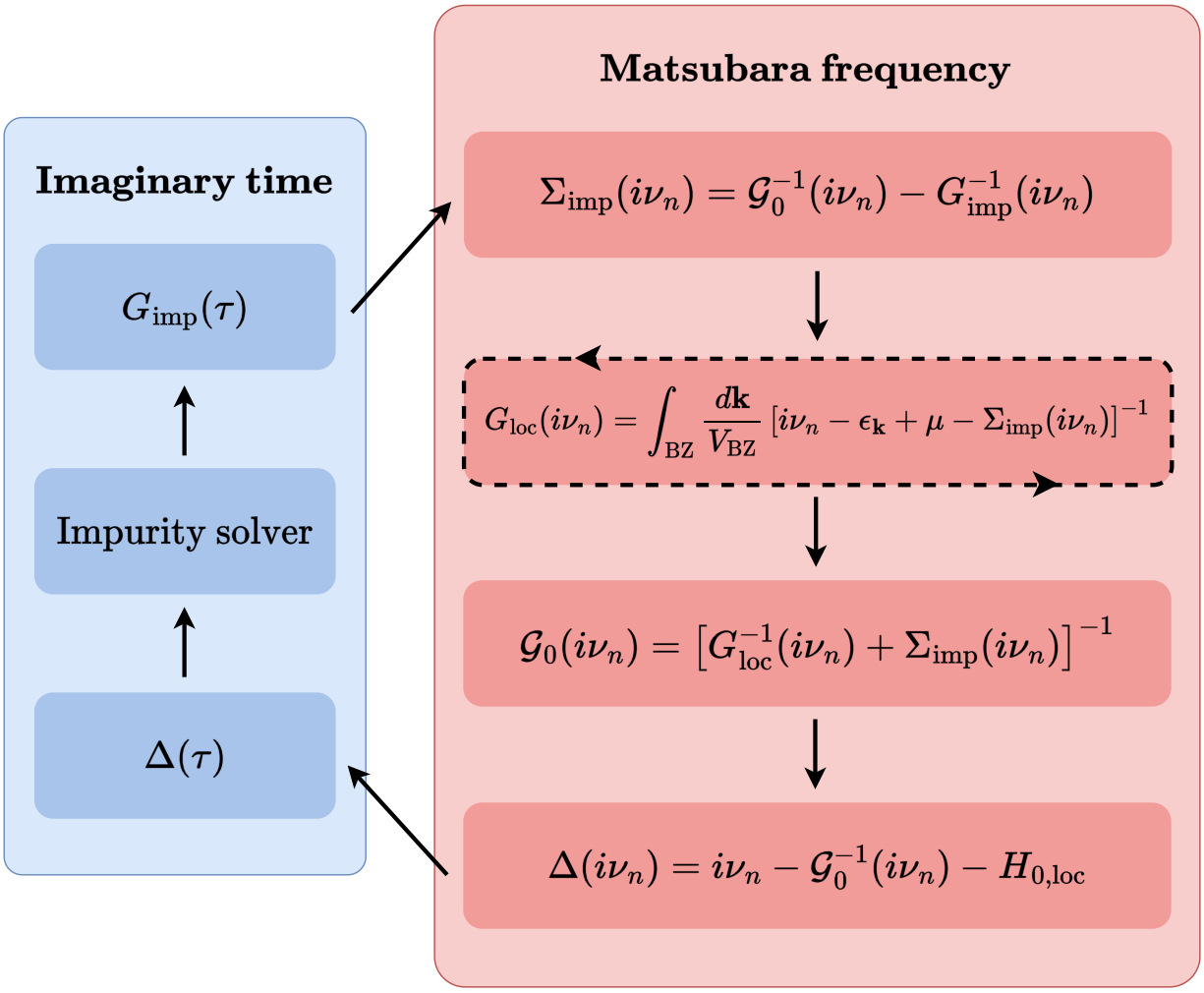

Figure 3.1: The steps of the DMFT loop. The arrows around the formula for $G_{\rm loc}$ indicate that this quantity is computed self-consistently with the chemical potential to maintain the correct particle density. Our approach improves the efficiency of the DMFT loop by making two simple changes compared with the standard algorithm: (1) All operations in the Matsubara frequency domain are carried out only at the DLR nodes $\nu_n = \nu_{n_k}$, rather than the full Matsubara frequency grid, and (2) the imaginary time hybridization function $\Delta(\tau)$ is obtained from the computed values $\Delta(i\nu_{n_k})$ by forming a DLR expansion and obtaining its Fourier transform analytically.

Here, the effective non-interacting bath is represented by the Weiss mean-field,

$$\mathcal{G}_0^{-1}(i\nu_n) = G_{\rm loc}^{-1}(i\nu_n) + \Sigma_{\rm imp}(i\nu_n)\,, \tag{3.5}$$

obtained from the local Green's function (3.3). The local Green's function is obtained self-consistently, and convergence is reached when $G_{\rm loc} = G_{\rm imp}$. For concreteness, we focus in this work on the continuous-time hybridization expansion (CTHYB) impurity solver [268], in which the impurity problem is defined through the local non-interacting Hamiltonian

$$H_{0,\rm loc} = \int_{\rm BZ} \frac{d\mathbf{k}}{V_{\rm BZ}}\, \epsilon_{\mathbf{k}} - \mu \tag{3.6}$$

and the Matsubara frequency hybridization function

$$\Delta(i\nu_n) = i\nu_n - \mathcal{G}_0^{-1}(i\nu_n) - H_{0,\rm loc}, \tag{3.7}$$

or its Fourier transform $\Delta(\tau)$ to the imaginary time domain. We emphasize, however, that compact representations of the type used here are in principle equally applicable for other types of impurity solvers.

The DMFT loop, outlined above, is summarized in Fig. 3.1. Although the solution of the impurity problem is often the most computationally intensive and technical step in the DMFT loop, it is outside the scope of our current discussion. Rather, we focus on the calculation of $G_{\rm loc}(i\nu_n)$, which requires the evaluation of a BZ integral for each Matsubara frequency grid point $i\nu_n$. In typical calculations all Matsubara frequency points are used up to a cutoff $\mathcal{O}\left(\omega_{\rm max}\right)$ (yielding $\mathcal{O}\left(\beta\omega_{\rm max}\right)$ points in total), in order to capture the effective energy scales of the system. We demonstrate here that the number of Matsubara frequency points at which $G_{\rm loc}(i\nu_n)$ must be computed can be dramatically reduced.

3.2.2 Discrete Lehmann representation and compact Matsubara frequency grids

The DLR method provides a compact, explicit basis for Matsubara Green's functions and self-energies, along with associated interpolation grids. We give a brief review of these concepts here, and refer to Ref. [143] for a detailed presentation and analysis.

Each Matsubara Green's function $G(i\nu_n)$ has a spectral Lehmann representation

$$G(i\nu_n) = -\int_{-\infty}^{\infty} K(i\nu_n, \omega)\, \rho(\omega)\, d\omega, \tag{3.8}$$

where $\rho(\omega)$ is the spectral function, and the analytic continuation kernel K is given by

$$K(i\nu_n, \omega) \equiv (\omega - i\nu_n)^{-1}. \tag{3.9}$$

In most practical applications, ρ is unknown, but $G(i\nu_n)$ can either be sampled directly or obtained from samples of the imaginary time Green's function $G(\tau)$. We assume ρ can be truncated beyond a frequency cutoff $|\omega| = \omega_{\max}$. Defining the dimensionless parameter

$$\Lambda \equiv \beta\omega_{\max},$$

and nondimensionalizing variables by $\nu_n \leftarrow \beta\nu_n$ and $\omega \leftarrow \beta\omega$, we obtain the truncated Lehmann representation

$$G(i\nu_n) = -\int_{-\Lambda}^{\Lambda} K(i\nu_n, \omega)\, \rho(\omega)\, d\omega, \tag{3.10}$$

where ν_n is given as above with $\beta = 1$, and the arguments of G, ρ have been suitably rescaled.

It can be shown that the kernel of this integral representation, $K(i\nu_n, \omega)$, has super-exponentially decaying singular values [275, 48]. This low-rank structure is indicative of the

well-known ill-conditioning of analytic continuation from the Matsubara Green's function to the spectral function on the real frequency axis [276]. However, it is advantageous for the representation of Matsubara Green's functions themselves, implying that $K(i\nu_n, \omega)$ can be approximated for any $\omega \in [-\Lambda, \Lambda]$ as a linear combination of a small number of basis functions. In particular, the DLR approach uses frequency samples of the kernel itself as basis functions:

$$K(i\nu_n, \omega) \approx \sum_{l=1}^{r} K(i\nu_n, \omega_l)\pi_l(\omega). \tag{3.11}$$

The r *DLR frequencies* ω_l can be selected automatically by the pivoted Gram-Schmidt algorithm such that the approximation in (3.11) is numerically stable, and accurate to a user-provided error tolerance [45]. Substitution of (3.11) into (3.10) demonstrates the existence of an expansion of an arbitrary Matsubara Green's function in the basis $K(i\nu_n, \omega_l)$,

$$G(i\nu_n) \approx \sum_{l=1}^{r} K(i\nu_n, \omega_l)\widehat{g}_l, \tag{3.12}$$

with $\widehat{g}_l = -\int_{-\Lambda}^{\Lambda} \pi_l(\omega)\rho(\omega)\, d\omega$.

The rapid decay of the singular values of K implies the scaling $r = \mathcal{O}\left(\log(\Lambda)\log\left(\varepsilon^{-1}\right)\right)$, yielding exceptionally compact expansions at high accuracies and low temperatures. For example, Matsubara Green's functions with $\Lambda = 100$ can be represented to 6-digit accuracy by fewer than 20 basis functions; with $\Lambda = 10^4$ to 6-digit accuracy by fewer than 50 basis functions; and with $\Lambda = 10^6$ to 10-digit accuracy by fewer than 120 basis functions. By contrast, in a typical calculation, for example with $\beta = 1000\,\mathrm{eV}^{-1}$ and $\omega_{\max} = 10\,\mathrm{eV}$ ($\Lambda = 10^4$), one would typically require on the order of tens of thousands of Matsubara frequencies. We emphasize that given Λ and ε, the representation is universal; that is, independent of the specific structure of the spectral function ρ characterizing the Green's function, which is already taken into account by the automatic compression of the kernel K.

Since ρ is typically not known and the *DLR coefficients* $\widehat{g}_l$ cannot be computed directly,

they can in practice be recovered by fitting, or by interpolation at a collection of r *DLR Matsubara frequency nodes* $\{i\nu_{n_k}\}_{k=1}^r$ [143]. These nodes can be obtained automatically, using a process similar to that used to obtain the DLR frequencies, to ensure stable interpolation. Thus, a Green's function G can be characterized, to within a controllable error, by its values $G(i\nu_{n_k})$ at the DLR nodes.

The Fourier transform of (3.12) yields an imaginary time representation,

$$G(\tau) \approx \sum_{l=1}^{r} K(\tau, \omega_l)\widehat{g}_l, \tag{3.13}$$

with

$$K(\tau, \omega) \equiv \frac{e^{-\omega\tau}}{1 + e^{-\omega}}$$

in the transformed variables $\tau \leftarrow \tau/\beta$, $\omega \leftarrow \beta\omega$. As for the Matsubara frequency expansion, $G(\tau)$ can either be recovered by least squares fitting, or by interpolation at a collection of automatically selected *DLR imaginary time nodes* $\{\tau_k\}_{k=1}^r$. We note that the DLR interpolation procedure is similar to the method of sparse sampling used in conjunction with the IR basis, in which interpolation nodes are selected based on the extrema of the highest degree IR basis function [170].

3.3 Restriction to compact Matsubara frequency grid

We propose the following procedure to improve the efficiency of the DMFT loop: Given the self-energy Σ_{imp}, the local Green's function G_{loc} is evaluated only at the r DLR Matsubara frequency nodes $\{i\nu_{n_k}\}_{k=1}^r$, as are the Weiss mean-field $\mathcal{G}_0$ from (3.5) and the hybridization function Δ from (3.7). At this point, the DLR expansion of $\Delta(i\nu_n)$ is formed by interpolation from its values at the DLR nodes using the representation in (3.12), with G replaced by Δ. $\Delta(\tau)$ is then given analytically by a DLR expansion in imaginary time, as in (3.13). The rest of the DMFT procedure can be carried out without modification.

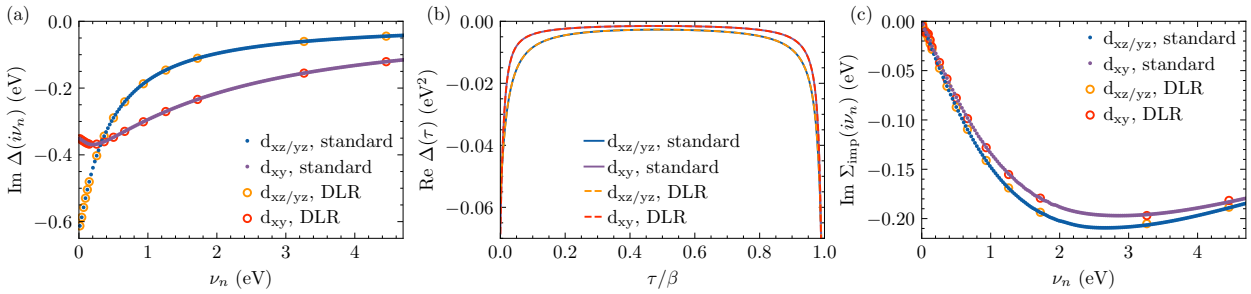

Figure 3.2: Hybridization function Δ and self-energy Σ_{imp} during the first iteration of the DMFT loop for the Sr_2RuO_4 example, demonstrating the use of the DLR procedure. (a) $\Delta(i\nu_n)$ (from initial guess with zero self-energy) given by (3.7), with DLR nodes indicated. (b) $\Delta(\tau)$ obtained using the standard method, i.e. asymptotic expansion and discrete Fourier transform, and DLR interpolation from the values $\Delta(i\nu_{n_k})$. (c) $\Sigma_{\mathrm{imp}}(i\nu_n)$ calculated after the impurity problem is solved with the hybridization function obtained using both methods.

The primary purpose of this work is to verify that systematic or statistical error generated by the quantum impurity solver does not destabilize our proposed procedure. Although this question depends on the specific choice of impurity solver, we carry out tests using the most popular solver, CTQMC. We show in the next section that the interpolation procedure is stable to Monte Carlo noise, and that the convergence of the DMFT loop is not affected by the reduction of the Matsubara frequency grid.

3.4 Numerical example: Strontium Ruthenate

We demonstrate our procedure using the correlated Hund's metal Sr_2RuO_4 [84] at low T. We compute the electronic structure using the planewave-based QUANTUM ESPRESSO package [87] using the standard Perdew–Burke–Ernzerhof exchange-correlation functional, and scalar-relativistic ultrasoft pseudopotentials [80]. After structural optimization on a $12\times12\times12$ Monkhorst-Pack grid, we obtain lattice parameters that correspond to $a = 3.880$ Å and $c = 12.887$ Å in the conventional unit cell (space group I4/mmm (139)). The primitive unit cell contains one ruthenium site with a partially filled t_{2g} shell for which we construct three maximally localized Wannier functions [211], representing the degenerate d_{xz}/d_{yz} orbitals

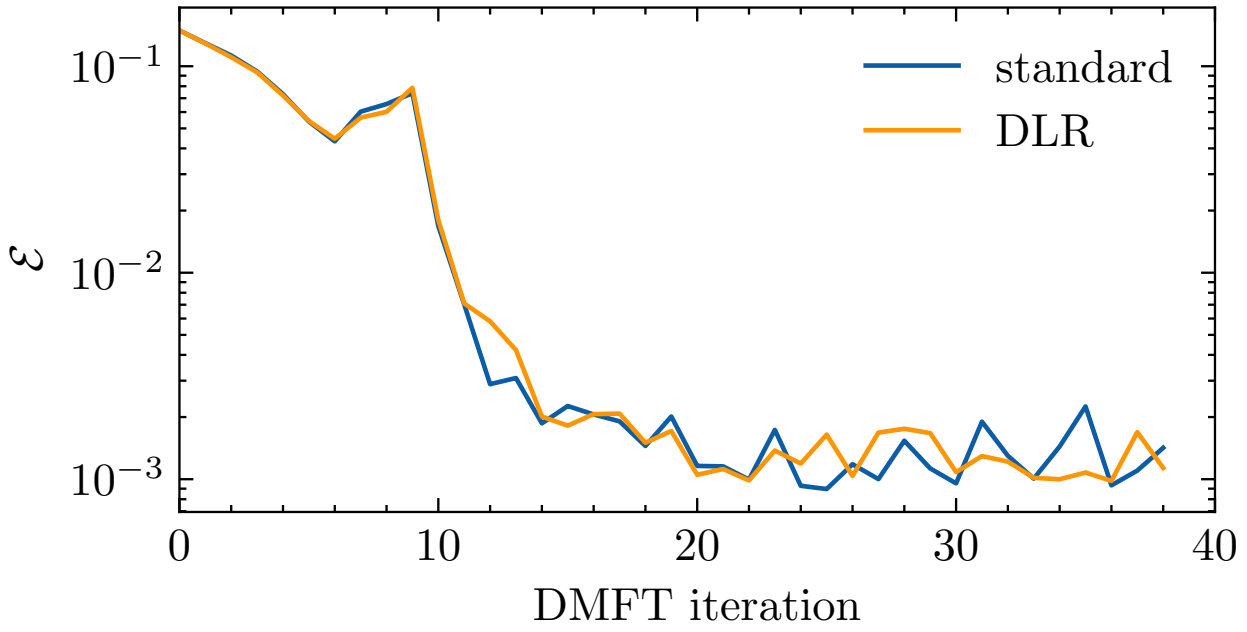

Figure 3.3: Convergence of DMFT self-consistency for the Sr_2RuO_4 example using standard and DLR procedures, measured using (3.14).

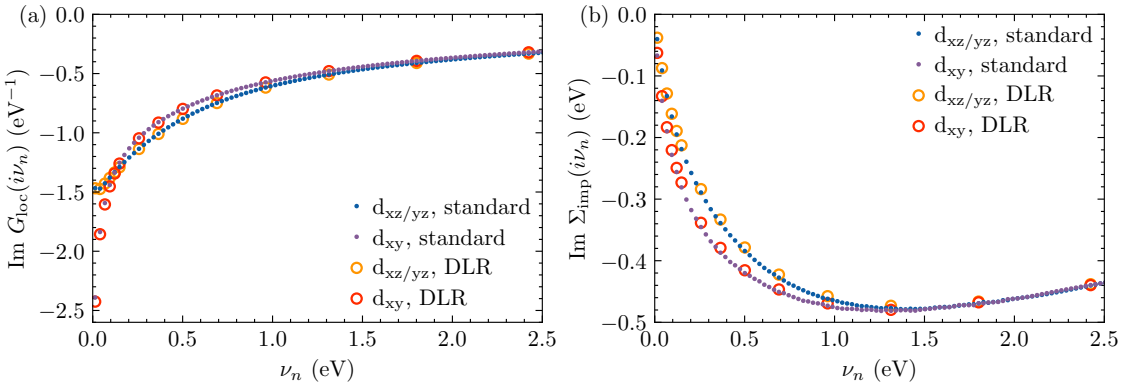

Figure 3.4: Converged results for the Sr_2RuO_4 example using standard and DLR procedures: (a) local Green's function, and (b) impurity self-energy in a low-frequency window.

and the d_{xy} orbital. We recompute the Hamiltonian on a $40 \times 40 \times 40$ k-point grid using Wannier interpolation in order to compute the BZ integrals in (3.3) by equispaced integration. We add a local rotationally invariant Hubbard-Kanamori interaction with $U = 2.3\,\text{eV}$ and $J = 0.4\,\text{eV}$ [84]. The impurity problem is solved using TRIQS/CTHYB [268] in the TRIQS library [229]. To address the well-known numerical instability of computing the self-energy via the Dyson equation in (3.4) in the presence of quantum Monte Carlo (QMC) noise, we replace this formula at high frequencies with an asymptotic expansion. This expansion is given by a polynomial in $(i\nu_n)^{-1}$, fit to Σ_{imp} in a window in which the QMC noise is sufficiently small so that (3.4) is valid.

The DMFT calculation is implemented using the TRIQS library [229], and the Python library `pydlr` provided by `libdlr` [144, 146] is used for DLR calculations. We solve the DMFT equations at $\beta = 232\,\text{eV}^{-1}$, which corresponds to $T = 50\,\text{K}$. At this temperature, without the DLR, approximately 12000 Matsubara frequency nodes are required to adequately capture the slowly-decaying tail of the Green's functions to allow for accurate Fourier transforms. More specifically, in the TRIQS library, the Fourier transform $\Delta(\tau)$ of $\Delta(i\nu_n)$ is obtained by the following procedure: (1) fit an asymptotic expansion in inverse powers of $i\nu_n$ to $\Delta(i\nu_n)$, (2) Fourier transform this asymptotic expansion analytically, (3) Fourier transform the difference between $\Delta(i\nu_n)$ and its asymptotic expansion, which is rapidly decaying, by a discrete Fourier transform on the Matsubara frequency grid, and add the results. Choosing $\omega_{\text{max}} = 12\,\text{eV}$ and $\epsilon = 10^{-6}\,\text{eV}^{-1}$, the number of DLR basis functions and Matsubara frequency nodes is $r = 36$, reducing the number of BZ integrals required to calculate G_{loc} in (3.3) by a factor of over 300. Furthermore, our approach avoids the complicated Fourier transform procedure used with the standard Matsubara frequency grid, since $\Delta(\tau)$ is obtained from the DLR expansion of $\Delta(i\nu_n)$ by analytical Fourier transform.

Fig. 3.2 shows the first iteration of the DMFT loop comparing the hybridization function and the self-energy obtained using the standard method and the DLR approach (shown in

markers/dashed lines and solid lines, respectively). In our scheme, we first compute G_{loc}, $\mathcal{G}_0$, and Δ at the DLR nodes $i\nu_n = i\nu_{n_k}$, using zero self-energy as an initial guess in (3.3). The hybridization function $\Delta(i\nu_n)$ is shown in Fig. 3.2a on the full Matsubara frequency grid, as used in the standard method, with the DLR nodes used in our method indicated. The DLR expansion of $\Delta(\tau)$ obtained from interpolation at these nodes and analytical Fourier transform is shown in Fig. 3.2b. Since no Monte Carlo noise has been introduced at this stage, the DLR expansion of $\Delta(\tau)$ is correct to the DLR tolerance ϵ. We then solve the impurity problem using the DLR expansion of $\Delta(\tau)$ to obtain the impurity Green's function, and subsequently the self-energy $\Sigma(i\nu_n)$, shown in Fig. 3.2c. We see that the self-energies obtained using the hybridization function obtained using the full grid DMFT procedure (shown at all Matsubara frequencies as dots) and the DLR procedure (shown at the DLR nodes as open circles) in the impurity solver agree to within the Monte Carlo noise level.

We next run the standard and modified DMFT loops until self-consistency. Convergence is measured by monitoring the quantity

$$\mathcal{E} = \sqrt{\frac{1}{\beta}\int_0^\beta d\tau \left\| G_{\text{imp}}(\tau) - G_{\text{loc}}(\tau) \right\|_F^2}, \tag{3.14}$$

where $\|\cdot\|_F$ indicates the Frobenius norm, and the normalization prevents a trivial scaling of the error with β, assuming a uniform distribution of Monte Carlo error. Fig. 3.3 shows that the convergence behavior is nearly identical for the two approaches, with both reaching self-consistency after after approximately 20 iterations. Finally, Fig. 3.4 shows $G_{\text{loc}}(i\nu_n)$ and $\Sigma_{\text{imp}}(i\nu_n)$ at convergence, demonstrating that the final results of the two calculations agree to within the Monte Carlo noise level.

3.5 Conclusion

Our proposed method improves the efficiency of the DMFT procedure by replacing the standard full Matsubara frequency grid with a highly compact grid compatible with interpolation using the DLR basis. We demonstrate the effectiveness of this approach for a DMFT calculation of Sr_2RuO_4 using CTQMC as the impurity solver. In general, our results suggest that the standard representations of quantities appearing in the DMFT loop can be replaced by much more efficient representations, such as the DLR, without incurring a penalty in accuracy or stability. We note that the same approach should be applicable to other impurity solvers, in particular fast approximate solvers used in real materials applications.

CHAPTER 4

GREEN'S FUNCTION FORMULATION OF QUANTUM DEFECT EMBEDDING THEORY

This chapter was previously published as Ref. 273.

4.1 Introduction

Electronic structure calculations of solids and molecules rely on the solution of approximate forms of the Schrödinger equation, for example using density functional theory [124, 155, 216, 192, 134, 36], many-body perturbation theory [286, 195, 94], or quantum chemistry methods [16, 343, 115] and, in some cases, quantum Monte Carlo [195]. Employing theoretical approximations is almost always necessary, as the solution of the electronic structure problem using the full many-body Hamiltonian of the system is still prohibitive, from a computational standpoint, for most molecules and solids, even in the case of the time independent Schröedinger equation.

Interestingly, there are important problems in condensed matter physics, materials science and chemistry for which a specific region of interest may be identified, a so-called active region, surrounded by a host medium, and for which the electronic structure problem can be solved at a high level of theory, for example, by exact diagonalization. An active region may be associated, for instance, to point defects in materials, active site of catalysts or nanoparticles embedded in soft or hard matrices. All of these problems may then be addressed using embedding theories [289, 133, 312] which separate the electronic structure problem of the active region from that of the host environment. Each part of the system is described at the quantum-mechanical level [289], at variance with quantum embedding models, e.g. QM/MM, where only the active space or region is described with quantum-mechanical methods, while the environment is treated classically [265, 181].

Several embedding techniques have been proposed in the literature in recent years, which may be classified by the level of theory chosen to describe the different portions of the system. Density-based theories encompass density-functional-theory embedding in-density- functional-theory (DFT-in-DFT) and wavefunction embedding in-DFT (WF-in-DFT) [173, 95, 96]. In these schemes the environment is described within DFT and the active region with a level of DFT higher than that adopted for the environment or with quantum-chemical, wave-function based methods. Density-matrix embedding theory (DMET) [335, 153, 154, 57, 238, 117, 237] employs instead the density matrix of the system to define an embedding protocol. Finally, Green's (G) function-based quantum embedding methods include the self-energy embedding [164, 342, 250] , dynamical mean field (DMFT) [82, 83, 81, 8, 156] and the quantum defect embedding theories (QDET) [185, 188, 312].

QDET is a theory we have recently proposed for the calculation of defect properties in solids, with the goal of computing strongly correlated states which may not be accurately obtained using mean field theories, such as DFT, when using large supercells. However, the applicability of the theory is not restricted to defects in solids and QDET may be used to study, in general, a small guest region embedded in a large host condensed system. Similar to all Green's function based methods, in QDET the active space is defined by a set of single-particle electronic states. The set includes the states localized in proximity of the defect or impurity and, in some cases, contains additional single-particle orbitals.

The embedding protocol used in QDET leads to a delicate problem that many embedding theories have in common, at least conceptually: the presence of "double counting" terms in the effective Hamiltonian of the active regions. These are terms that are computed both at the level of theory chosen for the active region and at the lower level chosen for the environment. Hence corrections (often called double counting corrections) are required to restore the accuracy of the effective Hamiltonian.

In the original formulation of QDET presented in Ref. 188, we adopted an approximate

double counting correction based on Hartree-Fock theory. Here we present a more rigorous derivation of QDET based on Green's functions and we derive a double counting correction that is exact within the G_0W_0 approximation and when retardation effects are neglected. We call this correction EDC@G_0W_0 (*exact* double counting at G_0W_0 level of theory). We then apply QDET with the EDC@G_0W_0 scheme to several spin defects in solids and we present a strategy to systematically converge the results as a function of the composition and size of the active space. Finally we show that using the EDC@G_0W_0, we obtain results for the electronic structure of spin defects consistent with experiments and in good agreement with results obtained with other embedding theories [207].

The rest of the chapter is organized as follows. Section 4.2 presents the formulation of QDET and Section 4.3 its implementation. Our results are presented in Section 4.4 and conclusions in Section 4.5.

4.2 Formulation of quantum defect embedding theory (QDET)

In Ref. 185, 188 we introduced the Quantum Defect Embedding Theory (QDET), an embedding scheme that describes a condensed system where the electronic excitations of interest occur within a small subspace (denoted as the active space A) of the full Hilbert space of the system. The formulation is based on the description of the system using periodic DFT and assumes that the interaction between active regions belonging to periodic replicas may be neglected (*i.e* the dilute limit). We summarize below the original formulation of the QDET method, including the approximate double counting scheme used in Ref. 185, 188. We then present a Green's function formulation of QDET which enables the definition of an improved correction to the double counting scheme originally adopted, which is exact within the G_0W_0 approximation.

In QDET an active space is defined as the space spanned by an orthogonal set of functions $\{\zeta_i\}$, for instance, selected eigenstates of the Kohn-Sham (KS) Hamiltonian describing a solid,

or localized functions, *e.g.*, Wannier orbitals constructed from Kohn-Sham eigenstates through a unitary transformation. Within the Born-Oppenheimer and nonrelativisitic approximations, the many-body effective Hamiltonian of a system of interacting electrons within a given active space takes the following form:

$$H^{\text{eff}} = \sum_{ij}^{A} t_{ij}^{\text{eff}} a_i^\dagger a_j + \frac{1}{2} \sum_{ijkl}^{A} v_{ijkl}^{\text{eff}} a_i^\dagger a_j^\dagger a_l a_k, \tag{4.1}$$

where t^{eff} and v^{eff} are one- and two-body terms that include the influence of the environment on the chosen active space. In QDET, these terms are determined by first carrying out a mean-field calculation of the full solid using, *e.g.*, DFT. Once the KS eigenstates and eigenvalues of the full system are obtained, the two-body terms v^{eff} are computed as the matrix elements of the partially screened static Coulomb potential W_0^R, *i.e.*,

$$v_{ijkl}^{\text{eff}} = \left[W_0^R\right]_{ijkl} := \int d\mathbf{x} d\mathbf{x}' \zeta_i(\mathbf{x}) \zeta_k(\mathbf{x}) W_0^R(\mathbf{x}, \mathbf{x}'; \omega = 0) \zeta_j(\mathbf{x}') \zeta_l(\mathbf{x}'). \tag{4.2}$$

The term W_0^R in Eq. 4.2 is obtained by screening the bare Coulomb potential v with the reduced polarizability P_0^R, defined by the following equation:

$$W_0^R = v + v P_0^R W_0^R. \tag{4.3}$$

The reduced polarizability may be obtained by subtracting from the total irreducible polarizability of the periodic system the contribution from the active space, namely $P_0^R = P_0 - P_0^A$. Within the Random-Phase Approximation (RPA), the active space polarizability P_0^A is given

by

$$P_0^A(\mathbf{x}_1,\mathbf{x}_2;\omega) = \sum_i^{\text{occ}} \sum_j^{\text{unocc}} \left(f^A\psi_i^{\text{KS}}\right)(\mathbf{x}_1)\left(f^A\psi_j^{\text{KS}}\right)(\mathbf{x}_1)\left(f^A\psi_j^{\text{KS}}\right)(\mathbf{x}_2)\left(f^A\psi_i^{\text{KS}}\right)(\mathbf{x}_2) \times \left(\frac{1}{\omega-(\epsilon_j^{\text{KS}}-\epsilon_i^{\text{KS}})+\mathrm{i}\eta}+\frac{1}{\omega+(\epsilon_j^{\text{KS}}-\epsilon_i^{\text{KS}})-\mathrm{i}\eta}\right), \tag{4.4}$$

where ψ_i^{KS} and ϵ_i^{KS} are the Kohn-Sham eigenfunctions and -values, respectively and "occ" and "unocc" denote sums over occupied and empty states, respectively. Here, we have introduced the projector $f^A = \sum_i^A |\zeta_i\rangle\langle\zeta_i|$ on the active space. An expression of the total irreducible polarizability may be obtained by omitting the projectors f^A on the RHS of Eq. 4.4. In Refs. 185, 188 we proposed an efficient implementation of Eq. 4.4 that does not require any explicit summation over unoccupied states, thus enabling the application of QDET to large systems.

The definition of v^{eff} given above includes contributions to the Hartree and exchange correlation energies that are also included in the DFT calculations for the whole solid, *i.e.*, it contains so-called double counting (dc) terms. The latter are subtracted (that is corrections to double counting contributions are applied) when defining the one-body terms t^{eff},

$$t_{ij}^{\text{eff}} = H_{ij}^{\text{KS}} - t_{ij}^{\text{dc}}, \tag{4.5}$$

where H^{KS} is the Kohn-Sham Hamiltonian.

4.2.1 QDET based on density functional theory

In previous applications of QDET, the double counting term t^{dc} was approximated, since within a DFT formulation of the theory, one cannot define an explicit expression for the exchange and correlation potential for a subset of electronic states. Therefore, an approximate

form of t^{dc} inspired by Hartree-Fock was used, given by:

$$t_{ij}^{\mathrm{dc}} \approx \sum_{kl}^{A} \left(\left[W_0^R(\omega = 0) \right]_{ikjl} - \left[W_0^R(\omega = 0) \right]_{ijkl} \right) \rho_{kl}^{A}, \tag{4.6}$$

where the reduced density matrix of the active space A is given by $\rho_{ij}^{A} = \sum_{k}^{\mathrm{occ}} \langle \zeta_i | \psi_k \rangle \langle \psi_k | \zeta_j \rangle$.

Once the terms in the Hamiltonian of Eq. 4.1 are defined, the electronic structure of the correlated states in the active space A is obtained from an exact diagonalization procedure, using the full configuration interaction (FCI) method.

We note that within Hartree-Fock theory, the expression of t^{dc}, where v replaces W_0^R on the RHS of Eq. 4.6, is exact; however Eq. 6 turns out to be an approximate expression when used within DFT. While QDET with an approximate double counting scheme has been successfully applied to a range of defects in diamond and SiC, the influence of the approximation used for t^{dc} deserves further scrutiny. Most importantly, a formulation without double counting approximations is desirable.

In the next section, we present a Green's function formulation of QDET and we derive an analytical expression for t^{eff} that in turns leads to an expression for the double counting term t^{dc} which is exact within the G_0W_0 approximation.

4.2.2 Green's function formulation of QDET

Instead of starting by a DFT formulation, we describe the interacting electrons in a solid by defining the one-body Green's function G and the screened Coulomb potential W. The reason to introduce a Green's function description stems from the fact that the self-energy Σ and its irreducible polarizability P can be written as sums of contributions from different

portions of the entire system. The basic equations relating G, W, Σ and P are:

$$G^{-1} = g^{-1} - \Sigma \tag{4.7}$$

$$W^{-1} = v^{-1} - P, \tag{4.8}$$

where v is the bare Coulomb potential; the bare Green's function $g = (\omega - h)^{-1}$ with $h = -\frac{1}{2}\nabla^2 + v_{\text{ion}}$, where v_{ion} is the electrostatic potential of the nuclei.

We chose two different levels of theory to describe different portions of the system, namely we describe the active space with a so-called higher level theory (high) than that applied to the whole system (low). We write the self-energy and polarizability of the whole system as:

$$\Sigma = \Sigma^{\text{low}} + \left(\Sigma^{\text{high}} - \Sigma^{\text{dc}}\right)_A \tag{4.9}$$

$$P = P^{\text{low}} + \left(P^{\text{high}} - P^{\text{dc}}\right)_A. \tag{4.10}$$

Here, we introduced the double counting terms Σ^{dc} and P^{dc} that correct for the contributions to the self-energy and polarizability of the active space A, which are included both in the high- and low-level descriptions of A. The terms with subscript A in Eqs. 4.9 and 4.10 are defined in the subspace A. Inserting Eqs. 4.9 and 4.10 into Eq. 4.7 and 4.8, respectively, leads to

$$G^{-1} = \left[G^R\right]^{-1} - \Sigma_A^{\text{high}} \tag{4.11}$$

$$W^{-1} = \left[W^R\right]^{-1} - P_A^{\text{high}}, \tag{4.12}$$

where we have defined the renormalized Green's function G^R and partially screened potential

W^R as:

$$\left[G^R\right]^{-1} = g^{-1} - \Sigma^{\text{low}} + \Sigma_A^{\text{dc}} \tag{4.13}$$

$$\left[W^R\right]^{-1} = v^{-1} - P^{\text{low}} + P_A^{\text{dc}}. \tag{4.14}$$

Comparing Eq. 4.11 and 4.12 with Eq. 4.7 and 4.8, we find that the problem of determing G and W for the total system $A + E$ has been simplified: only a solution with the high-level method within A is necessary to obtain G and W. To obtain such solution, the bare Green's function g and bare Coulomb potential v should be replaced by their renormalized counterparts G^R and W^R, respectively. We now turn to derive expressions for Σ^{low} and P^{low}, and Σ^{high} and P^{high}, which will then allow for the definition of all terms entering the effective Hamiltonian of the active space.

Effective Hamiltonian Under the assumption that retardation effects may be neglected, *i.e.*, assuming that one- and two-body interactions within A are instantaneous, we can derive a simple equation relating G^R and W^R and the parameters of the effective Hamiltonian in Eq. 4.1. In the absence of retardation effects, the effective Green's function G^R is given by the Lehmann representation and we have:

$$G^R(\omega) \approx \left[\omega - t^{\text{eff}}\right]^{-1}. \tag{4.15}$$

Note that the validity of this equation rests on the assumption that the non-diagonal terms of the self-energy coupling the active space and the environment are negligible, i.e. $\left(\Sigma^{\text{low}}\right)_{AE} = 0$. Eq. 4.15 defines the one-body terms t^{eff} of Eq. 4.1. To derive the two-body terms, we neglect the frequency dependence of the screened Coulomb interaction and write:

$$v_{ijkl}^{\text{eff}} \approx \int d\mathbf{x} d\mathbf{x}' \zeta_i(\mathbf{x}) \zeta_k(\mathbf{x}) W^R(\mathbf{x}, \mathbf{x}', \omega = 0) \zeta_j(\mathbf{x}') \zeta_l(\mathbf{x}'). \tag{4.16}$$

We note that the static approximation of the screened Coulomb interaction is commonly employed to calculate neutral excitations in solids and molecules within many-body perturbation theory (MBPT) [195], and it has been shown to yield neutral excitations in a wide range of materials with excellent accuracy. In order to obtain the expressions of t^{eff} and v^{eff} for which an analytic expression of t^{dc} can be derived, we turn to the G_0W_0 approximation, which we use as low level of theory for the entire system. Such a choice of low-level theory enables the separation of the self-energy as required by Eq. 4.9.

G_0W_0 approximation as low-level theory We use the G_0W_0 approximation and write $\Sigma^{\text{low}} = \Sigma^{G_0W_0}$ with

$$\Sigma^{G_0W_0} = V_{\text{H}} + \Sigma_{\text{xc}} = v\rho + \mathrm{i}G_0W_0. \tag{4.17}$$

We evaluate the Green's function G_0 using the KS Hamiltonian, *i.e.*,

$$G_0(\omega) = (\omega - H^{\text{KS}})^{-1}\,. \tag{4.18}$$

The screened Coulomb potential is obtained as $W_0^{-1} = v^{-1} - P_0$, with

$$P_0 = -\mathrm{i}G_0G_0. \tag{4.19}$$

Double counting correction To derive the double counting terms Σ^{dc} and P^{dc}, we require that the chain rule be satisfied, *i.e.*, that when using the low-level of theory to describe both the total system (A+E) and the active space (A), the total self-energy and the total polarizability on the LHS of Eq. 4.9 and 4.10 are the same as Σ^{low} and P^{low}, respectively. This requirement implies that Σ^{dc} and P^{dc} coincide with the self-energy and the polarizability derived from the effective Hamiltonian expressed at the low-level of theory. Within the G_0W_0 approximation, this requirement leads to the following expressions

$$\Sigma^{\rm dc} = \Sigma^{\rm eff}_{G_0W_0} \tag{4.20}$$

$$P^{\rm dc} = P^{\rm eff}_0. \tag{4.21}$$

Here the superscript 'eff' indicates that the the self-energy and polarizabilities are computed for $H^{\rm eff}$; these quantities are different from the corresponding ones evaluated for H projected onto A. The double counting contribution to the polarizability, $P^{\rm dc}$, is obtained with Eq. 4.19 after restricting the Green's function to A, *i.e.*,

$$P^{\rm dc} = P^A_0 = -{\rm i}G^A_0 G^A_0, \tag{4.22}$$

with $G^A_0 = f^A G_0 f^A$. Eq. 4.14 and 4.22 allow us to determine the partially screened Coulomb potential W^R_0 as

$$\left[W^R_0\right]^{-1} = v^{-1} - \left(G^A_0 G^R_0 + G^R_0 G^A_0 + G^R_0 G^R_0\right) = v^{-1} - P^R_0, \tag{4.23}$$

where we have defined the reduced Kohn-Sham Green's function $G^R_0 = G_0 - G^A_0$. The matrix elements of W^R_0 thus enter the definition of the two-body terms of the effective Hamiltonian. Hence we have shown that by framing QDET within the context of Green's embedding theories we recover Eq. 4.3.

Similar to the derivation of $P^{\rm dc}$, the double counting contribution to the self-energy, $\Sigma^{\rm dc}$, is given by the G_0W_0 self-energy associated to $H^{\rm eff}$, *i.e.*, $\Sigma^{\rm eff}_{G_0W_0} = v^{\rm eff}\rho^A + {\rm i}G^A_0 W^{\rm eff}_0$, where $v^{\rm eff} = W^R$, $\rho^{\rm eff} = \rho^A$, $G^{\rm eff}_0 = G^A_0$, and $W^{\rm eff}_0 = W_0$. The final result reads

$$\Sigma^{\rm dc} = W^R_0 \rho^A + {\rm i}G^A_0 W_0. \tag{4.24}$$

We note that in the second term of Eq. 4.24, the screened Coulomb potential in A is obtained

by adding to W_0^R the screening potential generated by the polarizability P_0^A. This addition yields by definition the total screened Coulomb potential, since $W_0^{-1} = \left[W_0^R\right]^{-1} - P_0^A$. We note that the chain rule by construction leads to a Hartree double-counting self-energy (the first term of Eq. 4.24) that is defined in terms of the partially screened Coulomb potential. This is essential to remove the Hartree self-energy of the effective Hamiltonian that is already accounted for in the G_0W_0 calculation of the total system (A+E). Equivalently, the second term in Eq. 4.24 removes the exchange-correlation self-energy of the effective Hamiltonian at the G_0W_0 level, as this self-energy has already been accounted for in the G_0W_0 calculation of the total system.

Having obtained explicit expressions for the double counting terms, we can finally determine the one-body parameters of the effective Hamiltonian. We write G^R as:

$$\begin{aligned}\left[G^R\right]^{-1} &= g^{-1} - [V_{\mathrm{H}} + \mathrm{i}G_0W_0] + \left[W_0^R(\omega=0)\rho + \mathrm{i}G_0^AW_0\right] \\ &= \omega - H^{\mathrm{KS}} + V_{\mathrm{xc}} + W_0^R\rho^A - \mathrm{i}G_0^RW_0.\end{aligned} \tag{4.25}$$

By comparing the equation above with Eqs. 4.5 and 4.15, we obtain the double counting contribution to the effective one-body terms as:

$$t^{\mathrm{dc}} = V_{\mathrm{xc}} + W_0^R(\omega=0)\rho^A - \mathrm{i}G_0^RW_0. \tag{4.26}$$

In general, the one-body terms should be frequency-dependent, due to the frequency dependency of $G_0^R(\omega)$ and $W_0(\omega)$. To obtain static expressions for the one-body terms, we evaluate $\mathrm{i}G_0^RW_0$ at the quasi-particle energies. More details are provided in Sec. 4.3.

As we will see in Sec. 4.4, the double counting scheme defined here yields more accurate results that the Hartee-Fock one, since it satisfies the chain rule by construction. On the contrary, the Hartree-Fock double counting scheme used in Ref. 25, 187, 185, 188, 213, 236 does not satisfy the chain rule and thus may introduce errors originating from the separation

between active space and environment.

4.3 Implementation

The QDET method and the double counting scheme of Eq. 4.26 are implemented in the WEST [99] (Without Empty States) code, a massively parallel open-source code designed for large-scale MBPT calculations of complex condensed-phase systems, such as defective solids. In the WEST code, a separable form of W_0 is obtained using the projected eigen-decomposition of the dielectric matrix (PDEP) [331, 99], which avoids the inversion and storage of large dielectric matrices. Importantly, explicit summations over empty KS orbitals entering the expressions of P_0 and G_0 are eliminated using density functional perturbation theory (DFPT) [15] and the Lanczos method [303, 217], respectively. The implementation of W_0^R in WEST has been reported previously [188]. In the following, we focus on the implementation of the double counting term entering Eq. 4.26.

In our current implementation, the active space A is defined by a set of Kohn-Sham eigenstates, and G_0^R is given by

$$G_0^R(\mathbf{x}, \mathbf{x}'; \omega) = \sum_i^E \frac{\psi_i^{\mathrm{KS}}(\mathbf{x})\psi_i^{\mathrm{KS}}(\mathbf{x}')}{\omega - \epsilon_i^{\mathrm{KS}} + \mathrm{i}\eta\ \mathrm{sgn}(\epsilon_i^{\mathrm{KS}} - \epsilon_{\mathrm{F}})}, \tag{4.27}$$

where E is the environment, sgn is the sign function and ϵ_{F} is the Fermi energy. The term $\Delta\Sigma_{\mathrm{xc}} = \mathrm{i}G_0^R W_0$ in Eq. 4.26 is given by

$$\Delta\Sigma_{\mathrm{xc}}(\omega) = \mathrm{i}\int \frac{d\omega'}{2\pi} G_0^R(\omega + \omega')W_0(\omega'), \tag{4.28}$$

where the integration is performed using a contour deformation technique [91, 89, 99]. Finally, to obtain static double counting terms, we evaluate Eq. 4.28 at the quasiparticle energies

ϵ_i^{QP}, *i.e.*,

$$[\Delta\Sigma_{\mathrm{xc}}]_{ij} = \frac{1}{2}\mathrm{Re}\left[[\Delta\Sigma_{\mathrm{xc}}]_{ij}\left(\epsilon_i^{\mathrm{QP}}\right) + [\Delta\Sigma_{\mathrm{xc}}]_{ij}\left(\epsilon_j^{\mathrm{QP}}\right)\right], \tag{4.29}$$

where the quasi-particle energies are obtained by solving iteratively the equation $\epsilon_i^{\mathrm{QP}} = \epsilon_i^{\mathrm{KS}} + \langle\psi_i^{\mathrm{KS}}|\Sigma_{\mathrm{xc}}(\epsilon_i^{\mathrm{QP}}) - V_{\mathrm{xc}}|\psi_i^{\mathrm{KS}}\rangle$. We note that Eq. 4.29 has also been used in Ref. 305 to implement the self-consistent *GW* method.

4.4 Results

4.4.1 Computational setup

The electronic structure of a supercell representing a defect within a periodic solid is initially obtained by restricted close-shell DFT calculations, with an optimized geometry from unrestricted open-shell calculations. We use the Quantum Espresso [88] code, with the PBE [232] or DDH functional [279], SG15 norm-conserving pseudopotentials [262] and a 50 Ry kinetic energy cutoff for the plane wave basis set. Only the Γ-point is employed to sample the Brillouin zone of the supercell.

The selection of the defect orbitals defining the active space may be performed by manually identifying a set of KS eigenstates localized around the defect of interest [187, 185, 188] or by using Wannier functions [213]. However these procedures do not offer a systematic means to verify convergence as a function of the composition and size of the active space.

Here we introduce a localization factor, a scalar L_V, associated to each KS orbital:

$$L_V(\psi_n^{\mathrm{KS}}) = \int_{V\subseteq\Omega} |\psi_n^{\mathrm{KS}}(\mathbf{x})|^2 \mathrm{d}\mathbf{x}, \tag{4.30}$$

where V is a chosen volume including the defect, smaller than the supercell volume Ω. The value of L_V varies between 0 and 1. The active space for a given defect is then defined by those KS orbitals for which L_V is larger than a given threshold. Decreasing the value of the

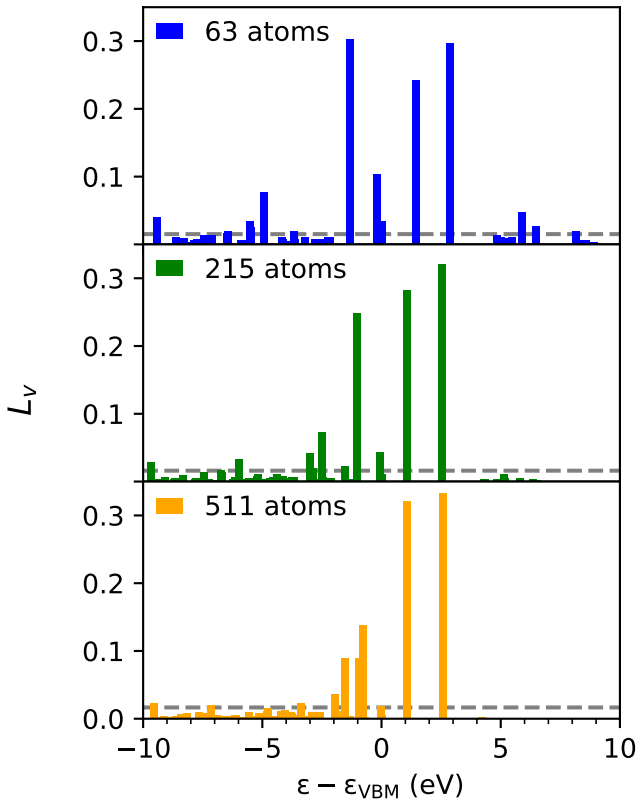

Figure 4.1: Localization factor (L_V, see Eq. 4.30) as a function of the energy of the Kohn-Sham orbitals, relative to the energy of the valence band maximum (VBM), for a NV^- center in diamond. We present results for supercells of three different sizes. The threshold used to define the active space is 5% (see text).

threshold allows for a systematic change in the composition and number of orbitals belonging to the active space.

In our calculations, the parameters of the effective Hamiltonian are obtained using constrained RPA (cRPA) calculations with the double counting correction of Eq. 4.26, called EDC@G_0W_0. The number of eigenpotentials N_{PDEP} used for the spectral decomposition of the polarizability is set to 512 in all calculations. Eigenvalues and eigenvectors of the active-space Hamiltonian are obtained with full-configuration interaction (FCI) calculations as implemented in the PySCF [288] code.

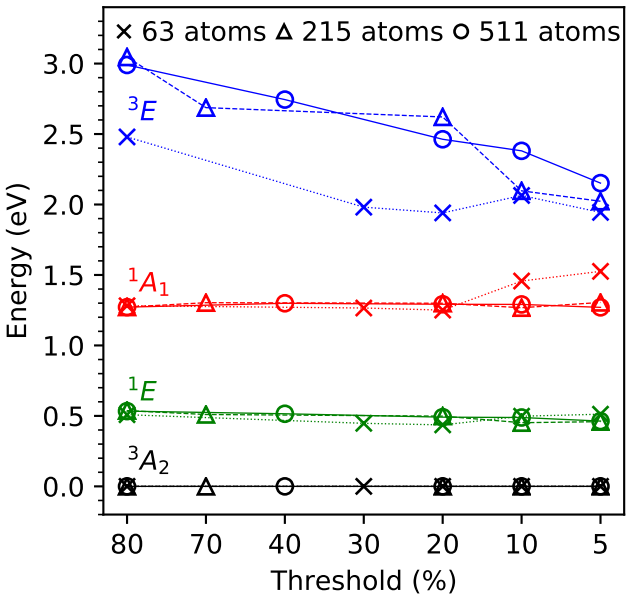

Figure 4.2: Computed vertical excitation energies of the NV^- center in diamond as a function of the chosen threshold of the localization factor L_V (see Eq. 4.30). States are labeled using the irreducible representation of the C_{3v} point group. We present results obtained with the PBE functional for cells of three different sizes. We note that 80% corresponds to a (4o, 6e), (3o, 4e) or (3o, 4e) active space for a 63-, 215- or 511-atom supercell respectively, and 5% corresponds to a (22o, 42e), (14o, 26e) or (12o, 22e) active space for a 63-, 215- or 511-atom supercell respectively.

4.4.2 Negatively-charged nitrogen vacancy center in diamond

As a prototypical spin qubit for quantum information science [60, 246, 93], the NV^- center in diamond has been extensively studied on different levels of theory [65, 197, 49, 25, 185, 187]. It is generally recognized [183, 66] that the four dangling bonds around the defect form a minimal model for the active space, with two non-degenerate a_1 orbitals, and two degenerate orbitals with e character.

Instead of constructing a model with a priori knowledge of the defect electronic structure, we determine the active-space composition and size with the help of the localization factor defined in Eq. 4.30, as shown in Fig. 4.1. When using 63-, 215- and 511-atom supercells, irrespective of the threshold used to define L_V, we find three defect orbitals with energies within the band gap of diamond, corresponding to the two degenerate e orbitals and to one

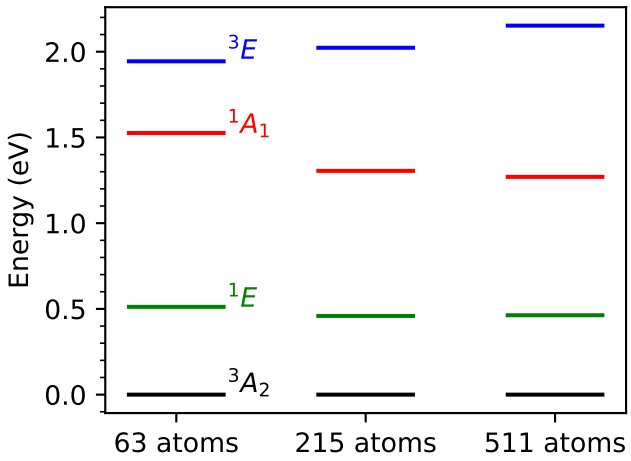

Figure 4.3: Computed vertical excitation energies for the NV^- in diamond. We show converged results (see Fig. 4.2) at 5% localization threshold as a function of the supercell size, obtained with the PBE functional.

of the a_1 orbital of the minimal model. In the 63- and 215-atom supercells, we find that one of the a_1 orbitals belonging to the minimal model is below the VBM of diamond; in the 511-atom cell we find instead that three localized orbitals are below the VBM, indicating that at least 6 orbitals are required to define the active space. This suggests that the minimal model with a fixed number of orbitals may be insufficient to accurately describe the system with a large supercell.

In Fig. 4.2 we show the vertical excitation energies of the NV^- center obtained by diagonalizing the effective Hamiltonian (Eq. 4.1), as a function of the localization threshold chosen to define L_V. Irrespective of the chosen threshold, we find that the ground state has $^3A_1$ symmetry. We also find that the lowest excited states with ^1E and $^1A_1$ symmetry converge much faster as a function of the L_V threshold than ^3E, since ^3E arises from $a_1^1e^3$ configurations rather than a $a_1^2e^2$ configurations, as in the case of $^3A_2$, ^1E and $^1A_1$. Most orbitals added to the active space when decreasing the localization threshold exhibit a_1 character. We note that the convergence of the $^1A_1$ state in the 63-atom cell is not smooth, probably due to orbitals with e character being part of the active space as the threshold value is decreased. Overall our results point at the need to converge the composition and size of the

active space both as a function of L_V and cell size. In Fig. 4.3 we show the vertical excitation energies of the NV^- center as a function of supercell size, and the values are summarized in Tab. 4.1. We chose a 5% L_V threshold, i.e. all orbitals with $L_V \geq 0.05$ are included in the active space A. As shown in Tab. 4.1, results obtained using the EDC@G_0W_0 correction are much closer to the experimental values than those computed using the original Hartree-Fock double counting correction (see Section 4.2.2), which we call here HFDC. Furthermore, we find unphysical excitations (i.e. states that do not have any experimental counterpart) with HFDC; however such unphysical states are not present when we use the EDC@G_0W_0 correction.

In our previous work, using HFDC corrrections we found substantial differences between results obtained with the PBE or the hybrid functional DDH [279, 280, 33, 32, 85, 345]. Hence we analyze the influence of the chosen functional when using the EDC@G_0W_0 correction. In Fig. 4.4 and 4.5, we compare PBE and DDH results for the NV^- center, for converged active space in a 215-atom cell. Our results indicate that, except for a widening of the bandgap, the electronic structure is almost insensitive to the choice of the functional. The order of localized defect states within the gap and their localization properties are nearly identical when using PBE and DDH, and the shift of the position of the defect orbitals relative to the band edges is mostly due to the difference in the PBE and DDH bandgaps. The excitation energies of DDH calculations are less than 0.1 eV higher than their PBE counterparts. It is reasonable to expect that the insensitivity to the functional found here in the case of the NV^- center may apply more generally to other classes of covalently bonded semiconductors; it appears that the sensitivity observed with the HFDC scheme may have been caused by the incomplete double counting correction of the DFT exchange-correlation effects. However obtaining results for additional defects and solids will be necessary to come to a firm conclusion.

Table 4.1: Computed vertical excitation energies (eV) for the NV^- in diamond for three states (see Fig. 4.3) obtained with QDET, the PBE functional and 511-atom supercells. We show results using the Hartree-Fock double counting (HFDC) and exact double counting (EDC@G_0W_0) schemes (see text). We also report experimental results (Exp), including results for zero-phonon lines (ZPL), and results obtained using GW and the Bethe-Salpeter Equation (BSE), model fit from GW solved by configuration interaction (CI), model obtained from constrained random phase approximation (cRPA) solved by CI, and quantum chemistry results on clusters from complete active space self-consistent field (CASSCF), multireference configuration interaction (MRCI) and Monte Carlo configuration interaction (MCCI).

Reference\Electronic States	^1E	$^1A_1$	^3E
Exp [60]			2.18
Exp ZPL[60, 246, 148, 93, 92]	0.34–0.43	1.51–1.60	1.945
QDET (EDC@G_0W_0)	0.463	1.270	2.152
QDET (HFDC)	0.375	1.150	1.324
GW + BSE [189]	0.40	0.99	2.32
Model fit from GW + CI [49]	0.5	1.5	2.1
Model from CRPA + CI [25]	0.49	1.41	2.02
$C_{85}H_{76}N^-$ CASSCF(6,6)[22]	0.25	1.60	2.14
$C_{49}H_{52}N^-$ CASSCF(6,8)[175]			2.57
$C_{19}H_{28}N^-$ MRCI(8,10)[349]	0.50	1.23	1.36
$C_{42}H_{42}N^-$ MCCI [63]	0.63	2.06	1.96

4.4.3 Neutral group-IV vacancy centers in diamond

In the last decade, a number of studies have investigated group-IV vacancy centers in diamond [78, 295, 102, 296, 344, 185, 187], using either a four-orbital [296] or a nine-orbital minimal model[187].

Similar to the case of the NV^- in diamond, we determine the active space using the localization factor shown in Fig. 4.6. We find a considerable number of localized orbitals. We exclude from the active space the localized conduction band orbitals, which are around 5 eV in SiV^0, since we found their contribution to the excitation energies to be negligible. We also exclude the defect atom's strongly-bound atomic orbitals, present at about -20 eV in GeV^0, SnV^0 and PbV^0, which have almost no hybridization with the host orbitals.

The vertical excitation energies of SiV^0 as a function of the localization threshold is reported in Fig. 4.7. In all three supercells we find a slow convergence of the excitation

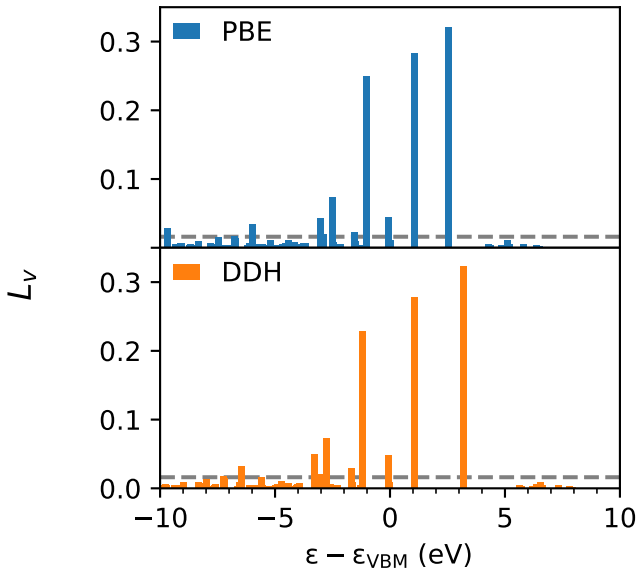

Figure 4.4: Localization factor (L_V, see Eq. 4.30) as a function of the energy of the Kohn-Sham orbitals, relative to the energy of the valence band maximum (VBM), for a NV^- center in diamond. We present results for 215-atom cell obtained with the PBE and DDH functionals. The threshold used to define the active space is 5% (see text).

energies, indicating that the excited states of this system are the result of the combination of many single-particle orbitals, and that a minimal model may be insufficient to obtain reliable excitation energies. Using the converged excitation energies for a given supercell, we show the convergence with supercell size in Fig. 4.8. Similar to the case of the NV^- center, the low-energy excitations are well converged with a 63-atom supercell, while the convergence of the $^3A_{2u}$, ^3E_u, $^1A_{1u}$, and $^3A_{1u}$ states is slower. In Tab. 4.2, we compare our best converged values obtained with the EDC@G_0W_0 correction with those obtained with the HFDC correction, as well as with available experimental and theoretical data. In general, the energies predicted using EDC@G_0W_0 are higher than those obtained with HFDC, and in better agreement with those of quantum chemical cluster calculations [207]. We note that the experimental zero phonon line (ZPL) corresponding to the ^3E_u level is 1.31 eV, but the contribution from the dynamical Jahn-Teller effect is unknown. Furthermore, the excitation energies computed with EDC@G_0W_0 show faster convergence compared to those with HFDC.

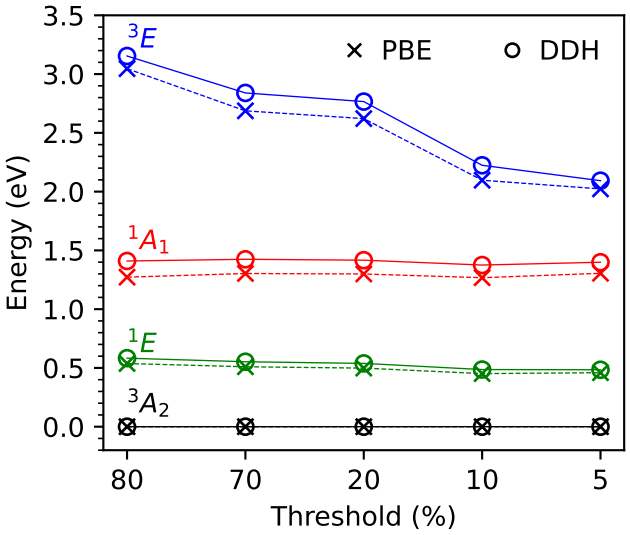

Figure 4.5: Computed vertical excitation energies of the NV^- center in diamond as a function of the chosen threshold of the localization factor L_V (see Eq. 4.30) to define the active space. States are labeled using the irreducible representation of the C_{3v} point group. We present results for 215-atom cell obtained with the PBE and DDH functionals. We note that 80% threshold corresponds to a (3o, 4e) active space, and 5% threshold corresponds to a (14o, 26e) or (15o, 28e) active space for PBE or DDH respectively.

For example, using EDC@G_0W_0 (HFDC) we find a difference of 0.15 (0.65) eV with 63-atom and 215-atom cells. As shown in Figs. 4.9 and 4.10, our results with the EDC@G_0W_0 scheme showed insensitivity to the choice of the functional. Our results for GeV^0, SnV^0 and PbV^0 are similar to those of SiV^0 and are summarized in Tab. 4.2.

4.5 Conclusion

In summary, in this work we presented a Green's function formulation of the quantum defect embedding theory (QDET) that enables the definition of an improved correction to the double counting scheme originally adopted in Refs 185, 188. We defined an effective Hamiltonian for the active space within a Green's function formalism, where the effective interaction is static and the self-energy cross-terms between the active space and the environment are neglected. Our results show that these approximations are appropriate to describe the localized defect

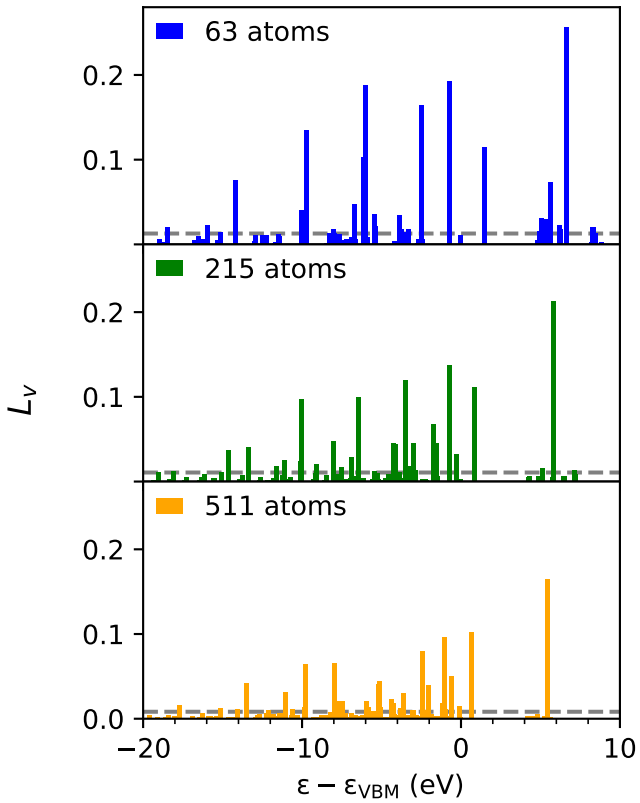

Figure 4.6: Localization factor (L_V, see Eq. 4.30) as a function of the energy of the Kohn-Sham orbitals, relative to the energy of the valence band maximum (VBM), for a SiV^0 center in diamond. We present results for supercells of three different sizes. The threshold used to define the active space is 5% (see text).

states in semiconductors investigated in this work. Within the Green's function formalism adopted here, we derived an exact double counting scheme (EDC@G_0W_0) replacing the approximate scheme originally adopted in Refs 185, 188. We emphasize that the double counting correction EDC@G_0W_0 enables the removal of any double counting terms arising from the separation of the whole system into active space and environment. We then described the implementation of the scheme within the WEST code [99], including a strategy to ensure convergence of our calculations with respect to the size and composition of the active space. Further, we demonstrated that QDET with exact double counting provides reliable results for several defects in diamond, with negligible dependence on the functional chosen for the underlying DFT calculations of the defects. Work is in progress to apply QDET with the

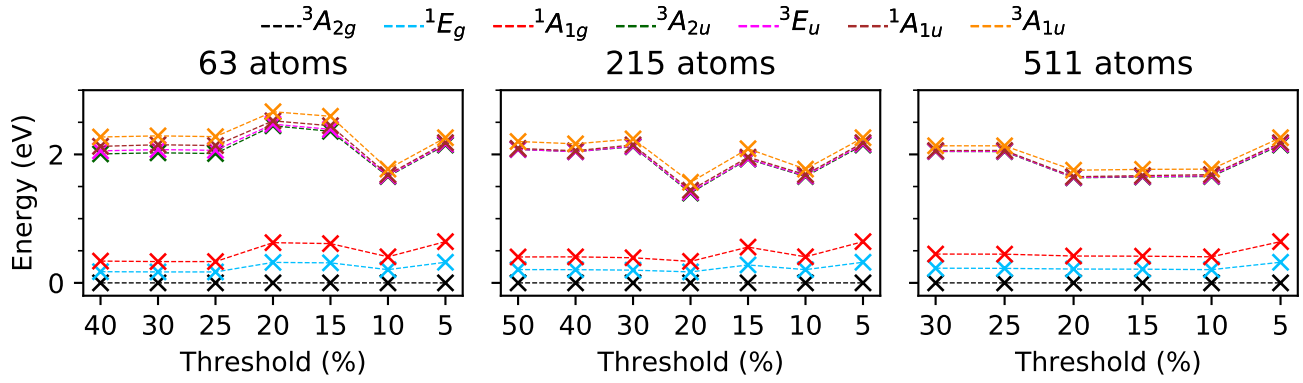

Figure 4.7: Computed vertical excitation energies of the SiV^0 center in diamond as a function of the chosen threshold of the localization factor L_V (see Eq. 4.30) to define the active space. States are labeled using the irreducible representation of the D_{3d} point group. We present results obtained with the PBE functional for cells of three different sizes. We note that a 40%, 50% or 30% threshold corresponds to a (7o, 12e), (5o, 8e) or (9o, 16e) active space for a 63-, 215- or 511-atom supercell respectively, and 5% threshold corresponds to a (32o, 62e), (40o, 78e) or (48o, 94e) active space for a 63-, 215- or 511-atom supercell respectively.

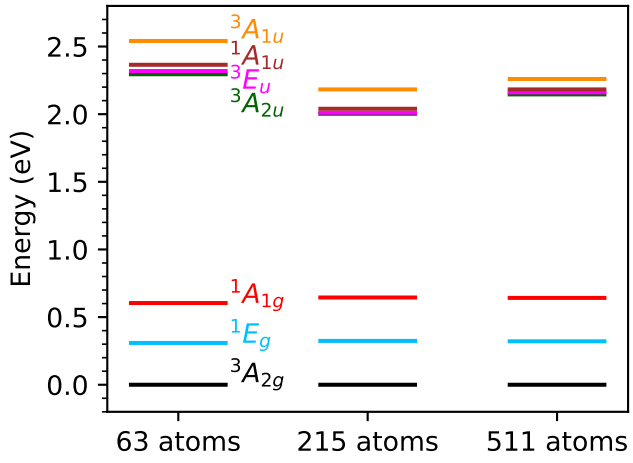

Figure 4.8: Computed vertical excitation energies for the SiV^0 in diamond. We show converged results (see Fig. 4.2) at 5% localization threshold, as a function of the supercell size, obtained with the PBE functional.

EDC@G_0W_0 scheme to more complex systems, such as defects in oxides and molecules on surfaces.

Table 4.2: Computed vertical excitation energies (eV) for the SiV^0, GeV^0, SnV^0 and PbV^0 in diamond for six states (see also Fig. 4.8 for the SiV^0 results) obtained with QDET, the PBE functional and 511-atom supercells. We show results using the Hartree-Fock double counting (HFDC) and exact double counting (EDC@G_0W_0) schemes (see text). We also report experimental results for zero-phonon lines (ZPL), and results obtained with a combination of second-order N-electron valence state perturbation theory (NEVPT2) and density matrix embedding theory (DMET), and quantum chemistry calculations on clusters from NEVPT2.

System	Reference\Electronic States	^1E_g	$^1A_{1g}$	$^3A_{2u}$	^3E_u	$^1A_{1u}$	$^3A_{1u}$
SiV^0	Exp ZPL				1.31		
	QDET (EDC@G_0W_0)	0.321	0.642	2.146	2.161	2.183	2.260
	QDET (HFDC)	0.236	0.435	1.098	1.096	1.111	1.188
	NEVPT2-DMET(10,12)[207]	0.51	1.14	2.39	2.47		2.61
	$C_{84}H_{78}Si_0$ NEVPT2(10,12)[207]	0.54	1.10	2.10	2.16		2.14
GeV^0	QDET (EDC@G_0W_0)	0.357	0.717	2.924	2.925	2.940	2.970
	QDET (HFDC)	0.289	0.554	1.456	1.443	1.443	1.495
SnV^0	QDET (EDC@G_0W_0)	0.295	0.596	2.590	2.571	2.561	2.616
	QDET (HFDC)	0.276	0.551	1.459	1.444	1.436	1.491
PbV^0	QDET (EDC@G_0W_0)	0.319	0.640	3.095	3.072	3.056	3.099
	QDET (HFDC)	0.302	0.600	1.788	1.768	1.755	1.796

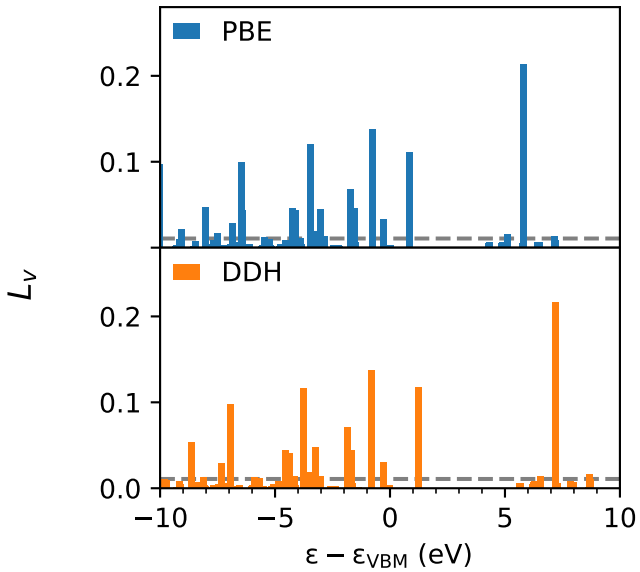

Figure 4.9: Localization factor (L_V, see Eq. 4.30) as a function of the energy of the Kohn-Sham orbitals, relative to the energy of the valence band maximum (VBM), for a SiV^0 center in diamond. We present results for a 215-atom cell obtained with the PBE and DDH functionals. The threshold used to define the active space is 5% (see text).

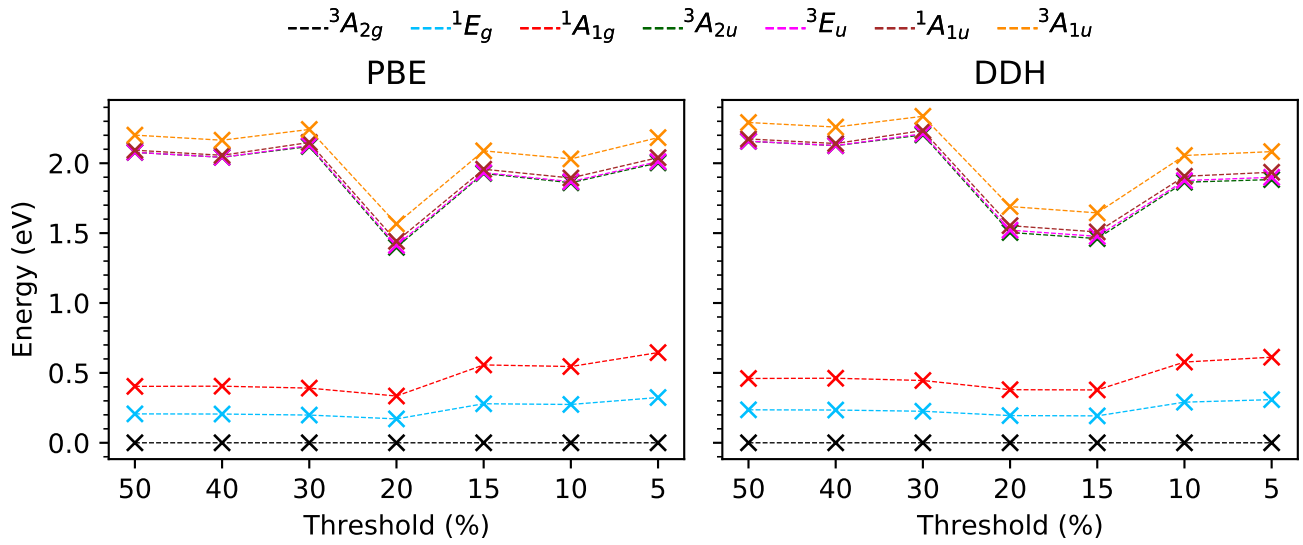

Figure 4.10: Computed vertical excitation energies (eV) of the NV^- center in diamond as a function of the chosen threshold of the localization factor L_V (see Eq. 4.30). States are labeled using the irreducible representation of the D_{3d} point group. We present results for a 215-atom cell obtained with the PBE and DDH functionals.

CHAPTER 5

CONCLUSION AND OUTLOOK

In this thesis I discussed three different approaches to understanding quantum many-body systems.

In the first approach, I develop two novel multiscale initialization methods top-down and bottom-up, following the spirit of multigrid method and mean-field theory respectively, to solve large-scale eigenvalue problems. I test the algorithm using 1D periodic transverse-field Ising model and high-dimensional Fokker-Planck equations. The results demonstrates good accuracy and advantage of the algorithms compared to density-matrix renormalization group. The algorithms are promising for solving high-dimensional partial differential equations and 2D/3D quantum systems and these would be future works.

In the second approach, I apply a newly developed low-rank Green's function representation, *i.e.* the discrete Lehmann representation (DLR), to dynamical mean-field theory (DMFT), which is a key theory understanding properties of strongly correlated materials. With the low-rank representation, we reduce two orders of magnitude of the number of frequency points in the whole DMFT loop and thus allowing great acceleration. Since DLR is a general representation for all finite-temperature Green's function theories, in the future I plan to apply the method to other methods such as finite-temperature GW method.

In the third approach, I develop a new quantum embedding framework, called quantum defect embedding theory (QDET), to study strongly correlated electronic states in materials. The embedding is theoretically equivalent to GW+DMFTΓ but focusing on different applications. Prototypical systems include spin defects in materials, heterogeneous center in liquids, molecules on surface etc. We test the applicability of the method using a few spin qubit candidates. The results show good comparison to experimental data, indicating good accuracy and excellent convergence of the method. The effects of frequency-dependent effects can possibly be studied for QDET.

APPENDIX A

PUBLICATION LIST

1. **Sheng, N.**, Yang, S., Chen, Y., & Khoo, Y. (2023). Multiscale initialization methods for high-dimensional partial differential equations. In preparation.

2. **Sheng, N.**, Hampel, A., Beck, S., Parcollet, O., Wentzell, N., Kaye, J., & Chen, K. (2023). Low-rank Green's function representations applied to dynamical mean-field theory. Physical Review B, 107(24), 245123.

3. Huang, B., **Sheng, N.**, Govoni, M., & Galli, G. (2023). Quantum simulations of Fermionic Hamiltonians with efficient encoding and ansatz schemes. Journal of Chemical Theory and Computation, 19(5), 1487-1498.

4. Vorwerk, C., **Sheng, N.***, Govoni, M., Huang, B., & Galli, G. (2022). Quantum embedding theories to simulate condensed systems on quantum computers. Nature Computational Science, 2(7), 424-432.

5. **Sheng, N.***, Vorwerk, C., Govoni, M., & Galli, G. (2022). Green's function formulation of quantum defect embedding theory. Journal of Chemical Theory and Computation, 18(6), 3512-3522.

6. Ma, H., **Sheng, N.**, Govoni, M., & Galli, G. (2021). Quantum embedding theory for strongly correlated states in materials. Journal of Chemical Theory and Computation, 17(4), 2116-2125.

7. Ma, H., **Sheng, N.**, Govoni, M., & Galli, G. (2020). First-principles studies of strongly correlated states in defect spin qubits in diamond. Physical Chemistry Chemical Physics, 22(44), 25522-25527.

BIBLIOGRAPHY

[1] S. L. Adler. Quantum theory of the dielectric constant in real solids. Phys. Rev., 126(2):413–420, April 1962.

[2] A. Agrawal and A. Choudhary. Perspective: Materials informatics and big data: Realization of the "fourth paradigm" of science in materials science. APL Mater., 4(5):053208, Apr. 2016.

[3] S. Ahn, M. Hong, M. Sundararajan, D. H. Ess, and M.-H. Baik. Design and optimization of catalysts based on mechanistic insights derived from quantum chemical reaction modeling. Chem. Rev., 119(11):6509–6560, 2019.

[4] I. Aleiner, F. Arute, K. Arya, J. Atalaya, R. Babbush, J. C. Bardin, R. Barends, A. Bengtsson, S. Boixo, A. Bourassa, M. Broughton, B. B. Buckley, D. A. Buell, B. Burkett, N. Bushnell, Y. Chen, Z. Chen, B. Chiaro, R. Collins, W. Courtney, S. Demura, A. R. Derk, A. Dunsworth, D. Eppens, C. Erickson, E. Farhi, A. G. Fowler, B. Foxen, C. Gidney, M. Giustina, J. A. Gross, M. P. Harrigan, S. D. Harrington, J. Hilton, A. Ho, S. Hong, T. Huang, W. J. Huggins, L. B. Ioffe, S. V. Isakov, E. Jeffrey, Z. Jiang, C. Jones, D. Kafri, K. Kechedzhi, J. Kelly, S. Kim, P. V. Klimov, A. N. Korotkov, F. Kostritsa, D. Landhuis, P. Laptev, E. Lucero, O. Martin, J. R. McClean, T. McCourt, M. McEwen, A. Megrant, X. Mi, K. C. Miao, M. Mohseni, W. Mruczkiewicz, J. Mutus, O. Naaman, M. Neeley, C. Neill, H. Neven, M. Newman, M. Y. Niu, T. E. O'Brien, A. Opremcak, E. Ostby, B. Pató, A. Petukhov, C. Quintana, N. Redd, P. Roushan, N. C. Rubin, D. Sank, K. J. Satzinger, V. Shvarts, V. Smelyanskiy, D. Strain, M. Szalay, M. D. Trevithick, B. Villalonga, T. White, Z. J. Yao, P. Yeh, and A. Zalcman. Accurately computing electronic properties of materials using eigenenergies. arXiv:2012.00921 [quant-ph], Dec. 2020.

[5] G. Aleksandrowicz, T. Alexander, P. Barkoutsos, L. Bello, Y. Ben-Haim, D. Bucher, F. Cabrera-Hernández, J. Carballo-Franquis, A. Chen, C. Chen, et al. Qiskit: An open-source framework for quantum computing. Accessed on: Mar, 16, 2019.

[6] C. P. Anderson, A. Bourassa, K. C. Miao, G. Wolfowicz, P. J. Mintun, A. L. Crook, H. Abe, J. U. Hassan, N. T. Son, T. Ohshima, and D. D. Awschalom. Electrical and optical control of single spins integrated in scalable semiconductor devices. Science, 366(6470):1225–1230, Dec. 2019.

[7] P. W. Anderson. Localized magnetic states in metals. Phys. Rev., 124(1):41–53, Oct. 1961.

[8] V. I. Anisimov, A. I. Poteryaev, M. A. Korotin, A. O. Anokhin, and G. Kotliar. First-principles calculations of the electronic structure and spectra of strongly correlated systems: Dynamical mean-field theory. J. Phys. Condens. Matter, 9(35):7359–7367, Sept. 1997.

[9] F. Aryasetiawan and O. Gunnarsson. The GW method. Rep. Prog. Phys., 61(3):237–312, Mar. 1998.

[10] F. Aryasetiawan, M. Imada, A. Georges, G. Kotliar, S. Biermann, and A. I. Lichtenstein. Frequency-dependent local interactions and low-energy effective models from electronic structure calculations. Phys. Rev. B, 70(19):195104, Nov. 2004.

[11] F. Aryasetiawan, J. M. Tomczak, T. Miyake, and R. Sakuma. Downfolded self-energy of many-electron systems. Phys. Rev. Lett., 102(17):176402, Apr. 2009.

[12] A. Aspuru-Guzik, A. D. Dutoi, P. J. Love, and M. Head-Gordon. Simulated quantum computation of molecular energies. Science, 309(5741):1704–1707, Sept. 2005.

[13] T. Ayral, T.-H. Lee, and G. Kotliar. Dynamical mean-field theory, density-matrix embedding theory, and rotationally invariant slave bosons: A unified perspective. Phys. Rev. B, 96(23):235139, Dec. 2017.

[14] R. Babbush, N. Wiebe, J. McClean, J. McClain, H. Neven, and G. K.-L. Chan. Low-depth quantum simulation of materials. Phys. Rev. X, 8(1):011044, Mar. 2018.

[15] S. Baroni, S. de Gironcoli, A. Dal Corso, and P. Giannozzi. Phonons and related crystal properties from density-functional perturbation theory. Rev. Mod. Phys., 73(2):515–562, July 2001.

[16] R. J. Bartlett and M. Musiał. Coupled-cluster theory in quantum chemistry. Rev. Mod. Phys., 79(1):291–352, Feb. 2007.

[17] L. Bassman, M. Urbanek, M. Metcalf, J. Carter, A. F. Kemper, and W. de Jong. Simulating quantum materials with digital quantum computers. arXiv:2101.08836 [quant-ph], Feb. 2021.

[18] B. Bauer, S. Bravyi, M. Motta, and G. Kin-Lic Chan. Quantum algorithms for quantum chemistry and quantum materials science. Chem. Rev., 120(22):12685–12717, Nov. 2020.

[19] B. Bauer, D. Wecker, A. J. Millis, M. B. Hastings, and M. Troyer. Hybrid quantum-classical approach to correlated materials. Phys. Rev. X, 6(3):031045, Sept. 2016.

[20] A. D. Becke. Perspective: Fifty years of density-functional theory in chemical physics. J. Chem. Phys., 140(18):18A301, Apr. 2014.

[21] A. T. Bell and M. Head-Gordon. Quantum mechanical modeling of catalytic processes. Annu. Rev. Chem. Biomol. Eng., 2(1):453–477, July 2011.

[22] C. Bhandari, A. L. Wysocki, S. E. Economou, P. Dev, and K. Park. Multiconfigurational study of the negatively charged nitrogen-vacancy center in diamond. Phys. Rev. B, 103(1):014115, Jan. 2021.

[23] S. Biermann. Dynamical screening effects in correlated electron materials—a progress report on combined many-body perturbation and dynamical mean field theory: 'GW+DMFT'. J. Phys. Condens. Matter, 26(17):173202, Apr. 2014.

[24] S. Biermann, F. Aryasetiawan, and A. Georges. First-principles approach to the electronic structure of strongly correlated systems: Combining the GW approximation and dynamical mean-field theory. Phys. Rev. Lett., 90(8):086402, Feb. 2003.

[25] M. Bockstedte, F. Schütz, T. Garratt, V. Ivády, and A. Gali. Ab initio description of highly correlated states in defects for realizing quantum bits. npj Quantum Mater., 3(1):1–6, June 2018.

[26] L. Boehnke, H. Hafermann, M. Ferrero, F. Lechermann, and O. Parcollet. Orthogonal polynomial representation of imaginary-time Green's functions. Phys. Rev. B, 84:075145, 2011.

[27] L. Boehnke, F. Nilsson, F. Aryasetiawan, and P. Werner. When strong correlations become weak: Consistent merging of GW and DMFT. Phys. Rev. B, 94(20):201106, Nov. 2016.

[28] M. Bogojeski, L. Vogt-Maranto, M. E. Tuckerman, K.-R. Müller, and K. Burke. Quantum chemical accuracy from density functional approximations via machine learning. Nat. Comm., 11(1):5223, Oct. 2020.

[29] D. W. Boukhvalov, L. I. Vergara, V. V. Dobrovitski, M. I. Katsnelson, A. I. Lichtenstein, P. Kögerler, J. L. Musfeldt, and B. N. Harmon. Correlation effects in the electronic structure of the Mn_4 molecular magnet. Phys. Rev. B, 77(18):180402, May 2008.

[30] S. Bravyi, D. Gosset, R. König, and M. Tomamichel. Quantum advantage with noisy shallow circuits. Nat. Phys., 16(10):1040–1045, Oct. 2020.

[31] S. B. Bravyi and A. Y. Kitaev. Fermionic quantum computation. Ann. Phys., 298(1):210–226, May 2002.

[32] N. P. Brawand, M. Govoni, M. Vörös, and G. Galli. Performance and self-consistency of the generalized dielectric dependent hybrid functional. J. Chem. Theory Comput., 13(7):3318–3325, 2017. PMID: 28537727.

[33] N. P. Brawand, M. Vörös, M. Govoni, and G. Galli. Generalization of dielectric-dependent hybrid functionals to finite systems. Phys. Rev. X, 6:041002, Oct 2016.

[34] A. Bruix, J. T. Margraf, M. Andersen, and K. Reuter. First-principles-based multiscale modelling of heterogeneous catalysis. Nat. Catal., 2(8):659–670, Aug. 2019.

[35] I. W. Bulik, W. Chen, and G. E. Scuseria. Electron correlation in solids via density embedding theory. J. Chem. Phys., 141(5):054113, Aug. 2014.

[36] K. Burke. Perspective on density functional theory. J. Chem. Phys., 136(15):150901, Apr. 2012.

[37] M. Caffarel and W. Krauth. Exact diagonalization approach to correlated fermions in infinite dimensions: Mott transition and superconductivity. Phys. Rev. Lett., 72(10):1545–1548, Mar. 1994.

[38] X. Cai, T. Wang, N. V. Prokof'ev, B. V. Svistunov, and K. Chen. Superconductivity in the uniform electron gas: Irrelevance of the Kohn-Luttinger mechanism. Phys. Rev. B, 106:L220502, 2022.

[39] Y. Cao, J. Romero, J. P. Olson, M. Degroote, P. D. Johnson, M. Kieferová, I. D. Kivlichan, T. Menke, B. Peropadre, N. P. D. Sawaya, S. Sim, L. Veis, and A. Aspuru-Guzik. Quantum chemistry in the age of quantum computing. Chem. Rev., 119(19):10856–10915, Oct. 2019.

[40] M. E. Casida and T. A. Wesołowski. Generalization of the Kohn-Sham equations with constrained electron density formalism and its time-dependent response theory formulation. Int. J. Quantum Chem., 96(6):577–588, 2004.

[41] M. Casula, A. Rubtsov, and S. Biermann. Dynamical screening effects in correlated materials: Plasmon satellites and spectral weight transfers from a Green's function ansatz to extended dynamical mean field theory. Phys. Rev. B, 85(3):035115, Jan. 2012.

[42] D. Ceperley and B. Alder. Quantum monte carlo. Science, 231(4738):555–560, feb 1986.

[43] F. T. Cerasoli, K. Sherbert, J. Sławińska, and M. B. Nardelli. Quantum computation of silicon electronic band structure. Phys. Chem. Chem. Phys., 22(38):21816–21822, Oct. 2020.

[44] Y. Chen and Y. Khoo. Combining particle and tensor-network methods for partial differential equations via sketching. arXiv:2305.17884 [cs, math, stat], 2023.

[45] H. Cheng, Z. Gimbutas, P.-G. Martinsson, and V. Rokhlin. On the compression of low rank matrices. SIAM J. Sci. Comput., 26(4):1389–1404, 2005.

[46] H.-P. Cheng, E. Deumens, J. K. Freericks, C. Li, and B. A. Sanders. Application of Quantum Computing to Biochemical Systems: A Look to the Future. Front. Chem., 8, 2020.

[47] W. Chibani, X. Ren, M. Scheffler, and P. Rinke. Self-consistent Green's function embedding for advanced electronic structure methods based on a dynamical mean-field concept. Phys. Rev. B, 93(16):165106, Apr. 2016.

[48] N. Chikano, J. Otsuki, and H. Shinaoka. Performance analysis of a physically constructed orthogonal representation of imaginary-time Green's function. Phys. Rev. B, 98(3):035104, 2018.

[49] S. Choi, M. Jain, and S. G. Louie. Mechanism for optical initialization of spin in NV-center in diamond. Phys. Rev. B, 86(4):041202, jul 2012.

[50] S. Choi, A. Kutepov, K. Haule, M. van Schilfgaarde, and G. Kotliar. First-principles treatment of Mott insulators: Linearized QSGW+DMFT approach. npj Quantum Mater., 1(1):1–6, July 2016.

[51] S. Choi, P. Semon, B. Kang, A. Kutepov, and G. Kotliar. ComDMFT: A massively parallel computer package for the electronic structure of correlated-electron systems. Comput. Phys. Commun., 244:277–294, Nov. 2019.

[52] K. Choudhary. Quantum computation for predicting solids-state material properties. arXiv:2102.11452 [cond-mat], Feb. 2021.

[53] A. Cichocki. Tensor networks for big data analytics and large-scale optimization problems. arXiv:1407.3124 [cs, math], 2014.

[54] M. Cini. Topics and methods in condensed matter theory: from basic quantum mechanics to the forefront of research. Springer, 2007. OCLC: ocn123375609.

[55] J. I. Colless, V. V. Ramasesh, D. Dahlen, M. S. Blok, M. E. Kimchi-Schwartz, J. R. McClean, J. Carter, W. A. de Jong, and I. Siddiqi. Computation of molecular spectra on a quantum processor with an error-resilient algorithm. Phys. Rev. X, 8(1):011021, Feb. 2018.

[56] P. M. Q. Cruz, G. Catarina, R. Gautier, and J. Fernández-Rossier. Optimizing quantum phase estimation for the simulation of Hamiltonian eigenstates. Quantum Sci. Technol., 5(4):044005, Aug. 2020.

[57] Z.-H. Cui, T. Zhu, and G. K.-L. Chan. Efficient implementation of ab initio quantum embedding in periodic systems: Density matrix embedding theory. J. Chem. Theory Comput., 16(1):119–129, 2020.

[58] Z.-H. Cui, T. Zhu, and G. K.-L. Chan. Efficient implementation of ab initio quantum embedding in periodic systems: Density matrix embedding theory. J. Chem. Theory Comput., 16(1):119–129, Jan. 2020.

[59] S. Curtarolo, W. Setyawan, G. L. W. Hart, M. Jahnatek, R. V. Chepulskii, R. H. Taylor, S. Wang, J. Xue, K. Yang, O. Levy, M. J. Mehl, H. T. Stokes, D. O. Demchenko, and D. Morgan. AFLOW: An automatic framework for high-throughput materials discovery. Computational Materials Science, 58:218–226, June 2012.

[60] G. Davies, M. F. Hamer, and W. C. Price. Optical studies of the 1.945 eV vibronic band in diamond. Proc. R. Soc. London A, 348(1653):285–298, Feb. 1976.

[61] L. De Leo, M. Civelli, and G. Kotliar. Cellular dynamical mean-field theory of the periodic Anderson model. Phys. Rev. B, 77(7):075107, Feb. 2008.

[62] J. J. de Pablo, N. E. Jackson, M. A. Webb, L.-Q. Chen, J. E. Moore, D. Morgan, R. Jacobs, T. Pollock, D. G. Schlom, E. S. Toberer, J. Analytis, I. Dabo, D. M. DeLongchamp, G. A. Fiete, G. M. Grason, G. Hautier, Y. Mo, K. Rajan, E. J. Reed, E. Rodriguez, V. Stevanovic, J. Suntivich, K. Thornton, and J.-C. Zhao. New frontiers for the materials genome initiative. NPJCM, 5(1):1–23, Apr. 2019.

[63] P. Delaney, J. C. Greer, and J. A. Larsson. Spin-Polarization Mechanisms of the Nitrogen-Vacancy Center in Diamond. Nano Lett., 10(2):610–614, Feb. 2010.

[64] D. Dhawan, M. Metcalf, and D. Zgid. Dynamical self-energy mapping (DSEM) for quantum computing. arXiv:2010.05441 [physics, physics:quant-ph], Feb. 2021.

[65] M. W. Doherty, N. B. Manson, P. Delaney, and L. C. L. Hollenberg. The negatively charged nitrogen-vacancy centre in diamond: the electronic solution. New J. Phys., 13(2):025019, feb 2011.

[66] M. W. Doherty, N. B. Manson, P. Delaney, F. Jelezko, J. Wrachtrup, and L. C. L. Hollenberg. The nitrogen-vacancy colour centre in diamond. Phys. Rep., 528(1):1–45, 2013.

[67] X. Dong, D. Zgid, E. Gull, and H. U. R. Strand. Legendre-spectral Dyson equation solver with super-exponential convergence. J. Chem. Phys., 152(13):134107, 2020.

[68] U. F. S. D′Haenens-Johansson, A. M. Edmonds, B. L. Green, M. E. Newton, G. Davies, P. M. Martineau, R. U. A. Khan, and D. J. Twitchen. Optical properties of the neutral silicon split-vacancy center in diamond. Phys. Rev. B, 84:245208, Dec 2011.

[69] C. E. Dreyer, A. Alkauskas, J. L. Lyons, A. Janotti, and C. G. Van de Walle. First-principles calculations of point defects for quantum technologies. Annu. Rev. Mater. Res., 48(1):1–26, 2018.

[70] M. Dvorak, D. Golze, and P. Rinke. Quantum embedding theory in the screened Coulomb interaction: Combining configuration interaction with GW-BSE. Phys. Rev. Mater., 3(7):070801, July 2019.

[71] M. Dvorak and P. Rinke. Dynamical configuration interaction: Quantum embedding that combines wave functions and Green's functions. Phys. Rev. B, 99(11):115134, Mar. 2019.

[72] W. E. Principles of Multiscale Modeling. Cambridge University Press, 2011.

[73] E. Eidelstein, E. Gull, and G. Cohen. Multiorbital quantum impurity solver for general interactions and hybridizations. Phys. Rev. Lett., 124(20):206405, May 2020.

[74] V. E. Elfving, B. W. Broer, M. Webber, J. Gavartin, M. D. Halls, K. P. Lorton, and A. Bochevarov. How will quantum computers provide an industrially relevant computational advantage in quantum chemistry? arXiv:2009.12472 [physics, physics:quant-ph], Sept. 2020.

[75] D. A. Fedorov, M. J. Otten, S. K. Gray, and Y. Alexeev. Ab initio molecular dynamics on quantum computers. J. Chem. Phys., 154(16):164103, Apr. 2021.

[76] A. P. Gaiduk, M. Govoni, R. Seidel, J. H. Skone, B. Winter, and G. Galli. Photoelectron spectra of aqueous solutions from first principles. J. Am. Chem. Soc., 138(22):6912–6915, June 2016.

[77] F. Gaitan. Quantum Error Correction and Fault Tolerant Quantum Computing. CRC Press, Feb. 2008.

[78] A. Gali and J. R. Maze. Ab initio study of the split silicon-vacancy defect in diamond: Electronic structure and related properties. Phys. Rev. B, 88:235205, Dec 2013.

[79] Q. Gao, H. Nakamura, T. P. Gujarati, G. O. Jones, J. E. Rice, S. P. Wood, M. Pistoia, J. M. Garcia, and N. Yamamoto. Computational investigations of the lithium superoxide dimer rearrangement on noisy quantum devices. J. Phys. Chem. A, 125(9):1827–1836, Mar. 2021.

[80] K. F. Garrity, J. W. Bennett, K. M. Rabe, and D. Vanderbilt. Pseudopotentials for high-throughput DFT calculations. Comput. Mater. Sci., 81:446–452, 2014.

[81] A. Georges. Strongly correlated electron materials: Dynamical mean-field theory and electronic structure. AIP Conf. Proc., 715(1):3–74, Aug. 2004.

[82] A. Georges and G. Kotliar. Hubbard model in infinite dimensions. Phys. Rev. B, 45(12):6479–6483, Mar. 1992.

[83] A. Georges, G. Kotliar, W. Krauth, and M. J. Rozenberg. Dynamical mean-field theory of strongly correlated fermion systems and the limit of infinite dimensions. Rev. Mod. Phys., 68(1):13–125, Jan. 1996.

[84] A. Georges, L. d. Medici, and J. Mravlje. Strong correlations from Hund's coupling. Annu. Rev. Condens. Matter Phys., 4(1):137–178, 2013.

[85] M. Gerosa, C. E. Bottani, C. D. Valentin, G. Onida, and G. Pacchioni. Accuracy of dielectric-dependent hybrid functionals in the prediction of optoelectronic properties of metal oxide semiconductors: a comprehensive comparison with many-body gw and experiments. J. Phys.: Condens. Matter, 30(4):044003, dec 2017.

[86] M. Gerosa, F. Gygi, M. Govoni, and G. Galli. The role of defects and excess surface charges at finite temperature for optimizing oxide photoabsorbers. Nature Materials, 17(12):1122–1127, Dec. 2018.

[87] P. Giannozzi, S. Baroni, N. Bonini, M. Calandra, R. Car, C. Cavazzoni, D. Ceresoli, G. L. Chiarotti, M. Cococcioni, I. Dabo, A. D. Corso, S. de Gironcoli, S. Fabris, G. Fratesi, R. Gebauer, U. Gerstmann, C. Gougoussis, A. Kokalj, M. Lazzeri, L. Martin-Samos, N. Marzari, F. Mauri, R. Mazzarello, S. Paolini, A. Pasquarello, L. Paulatto,

C. Sbraccia, S. Scandalo, G. Sclauzero, A. P. Seitsonen, A. Smogunov, P. Umari, and R. Wentzcovitch. Quantum ESPRESSO: a modular and open-source software project for quantum simulations of materials. J. Phys. Condens. Matter, 21:395502, 2009.

[88] P. Giannozzi, S. Baroni, N. Bonini, M. Calandra, R. Car, C. Cavazzoni, D. Ceresoli, G. L. Chiarotti, M. Cococcioni, I. Dabo, A. D. Corso, S. de Gironcoli, S. Fabris, G. Fratesi, R. Gebauer, U. Gerstmann, C. Gougoussis, A. Kokalj, M. Lazzeri, L. Martin-Samos, N. Marzari, F. Mauri, R. Mazzarello, S. Paolini, A. Pasquarello, L. Paulatto, C. Sbraccia, S. Scandolo, G. Sclauzero, A. P. Seitsonen, A. Smogunov, P. Umari, and R. M. Wentzcovitch. QUANTUM ESPRESSO: a modular and open-source software project for quantum simulations of materials. J. Phys.: Condens. Matter, 21(39):395502, sep 2009.

[89] M. Giantomassi, M. Stankovski, R. Shaltaf, M. Grüning, F. Bruneval, P. Rinke, and G.-M. Rignanese. Electronic properties of interfaces and defects from many-body perturbation theory: Recent developments and applications. Phys. Status Solidi B, 248(2):275–289, 2011.

[90] S. C. Glotzer. Assembly engineering: Materials design for the 21st century (2013 P.V. Danckwerts lecture). Chem. Eng. Sci., 121:3–9, Jan. 2015.

[91] R. W. Godby, M. Schlüter, and L. J. Sham. Self-energy operators and exchange-correlation potentials in semiconductors. Phys. Rev. B, 37(17):10159–10175, June 1988.

[92] M. L. Goldman, M. W. Doherty, A. Sipahigil, N. Y. Yao, S. D. Bennett, N. B. Manson, A. Kubanek, and M. D. Lukin. State-selective intersystem crossing in nitrogen-vacancy centers. Phys. Rev. B, 91(16):165201, Apr. 2015.

[93] M. L. Goldman, A. Sipahigil, M. W. Doherty, N. Y. Yao, S. D. Bennett, M. Markham, D. J. Twitchen, N. B. Manson, A. Kubanek, and M. D. Lukin. Phonon-Induced Population Dynamics and Intersystem Crossing in Nitrogen-Vacancy Centers. Phys. Rev. Lett., 114(14):145502, Apr. 2015.

[94] D. Golze, M. Dvorak, and P. Rinke. The GW compendium: A practical guide to theoretical photoemission spectroscopy. Front. Chem., 7:377, 2019.

[95] A. S. P. Gomes, C. R. Jacob, and L. Visscher. Calculation of local excitations in large systems by embedding wave-function theory in density-functional theory. Phys. Chem. Chem. Phys., 10(35):5353–5362, Aug. 2008.

[96] J. D. Goodpaster, T. A. Barnes, F. R. Manby, and T. F. Miller. Density functional theory embedding for correlated wavefunctions: Improved methods for open-shell systems and transition metal complexes. J. Chem. Phys., 137(22):224113, Dec. 2012.

[97] Google AI Quantum, F. Arute, K. Arya, R. Babbush, D. Bacon, J. C. Bardin, R. Barends, S. Boixo, M. Broughton, B. B. Buckley, D. A. Buell, B. Burkett, N. Bushnell, Y. Chen, Z. Chen, B. Chiaro, R. Collins, W. Courtney, S. Demura, A. Dunsworth, E. Farhi, A. Fowler, B. Foxen, C. Gidney, M. Giustina, R. Graff, S. Habegger, M. P. Harrigan, A. Ho, S. Hong, T. Huang, W. J. Huggins, L. Ioffe, S. V. Isakov, E. Jeffrey, Z. Jiang, C. Jones, D. Kafri, K. Kechedzhi, J. Kelly, S. Kim, P. V. Klimov, A. Korotkov, F. Kostritsa, D. Landhuis, P. Laptev, M. Lindmark, E. Lucero, O. Martin, J. M. Martinis, J. R. McClean, M. McEwen, A. Megrant, X. Mi, M. Mohseni, W. Mruczkiewicz, J. Mutus, O. Naaman, M. Neeley, C. Neill, H. Neven, M. Y. Niu, T. E. O'Brien, E. Ostby, A. Petukhov, H. Putterman, C. Quintana, P. Roushan, N. C. Rubin, D. Sank, K. J. Satzinger, V. Smelyanskiy, D. Strain, K. J. Sung, M. Szalay, T. Y. Takeshita, A. Vainsencher, T. White, N. Wiebe, Z. J. Yao, P. Yeh, and A. Zalcman. Hartree-Fock on a superconducting qubit quantum computer. Science, 369(6507):1084–1089, Aug. 2020.

[98] M. S. Gordon, D. G. Fedorov, S. R. Pruitt, and L. V. Slipchenko. Fragmentation methods: A route to accurate calculations on large systems. Chem. Rev., 112(1):632–672, Jan. 2012.

[99] M. Govoni and G. Galli. Large scale GW calculations. J. Chem. Theory Comput., 11(6):2680–2696, June 2015.

[100] M. Govoni and G. Galli. GW100: Comparison of methods and accuracy of results obtained with the WEST code. J. Chem. Theory Comput., 14(4):1895–1909, Apr. 2018.

[101] M. Govoni, J. Whitmer, J. de Pablo, F. Gygi, and G. Galli. Code interoperability extends the scope of quantum simulations. npj Comput. Mater., 7(1):1–10, Feb. 2021.

[102] B. L. Green, M. W. Doherty, E. Nako, N. B. Manson, U. F. S. D'Haenens-Johansson, S. D. Williams, D. J. Twitchen, and M. E. Newton. Electronic structure of the neutral silicon-vacancy center in diamond. Phys. Rev. B, 99(16):161112, Apr. 2019.

[103] E. Gull, S. Iskakov, I. Krivenko, A. A. Rusakov, and D. Zgid. Chebyshev polynomial representation of imaginary-time response functions. Phys. Rev. B, 98:075127, 2018.

[104] E. Gull, A. J. Millis, A. I. Lichtenstein, A. N. Rubtsov, M. Troyer, and P. Werner. Continuous-time Monte Carlo methods for quantum impurity models. Rev. Mod. Phys., 83(2):349–404, May 2011.

[105] E. Gull, A. J. Millis, A. I. Lichtenstein, A. N. Rubtsov, M. Troyer, and P. Werner. Continuous-time Monte Carlo methods for quantum impurity models. Rev. Mod. Phys., 83:349–404, 2011.

[106] F. Gygi. Architecture of Qbox: A scalable first-principles molecular dynamics code. IBM J. Res. Dev., 52(1.2):137–144, Jan. 2008.

[107] Q. Han, B. Chakrabarti, and K. Haule. Investigation into the inadequacy of crpa in reproducing screening in strongly correlated systems. arXiv:1810.06116, 2018.

[108] J. N. Harvey, F. Himo, F. Maseras, and L. Perrin. Scope and challenge of computational methods for studying mechanism and reactivity in homogeneous catalysis. ACS Catal., 9(8):6803–6813, 2019.

[109] K. Haule. Exact double counting in combining the dynamical mean field theory and the density functional theory. Phys. Rev. Lett., 115(19):196403, Nov. 2015.

[110] N. He and F. A. Evangelista. A zeroth-order active-space frozen-orbital embedding scheme for multireference calculations. J. Chem. Phys., 152(9):094107, Mar. 2020.

[111] K. Head-Marsden, J. Flick, C. J. Ciccarino, and P. Narang. Quantum information and algorithms for correlated quantum matter. Chem. Rev., 121(5):3061–3120, Mar. 2021.

[112] L. Hedin. New method for calculating the one-particle green's function with application to the electron-gas problem. Phys. Rev., 139:A796–A823, Aug 1965.

[113] L. Hedin. On correlation effects in electron spectroscopies and the GW approximation. J. Phys. Condens. Matter, 11(42):R489–R528, Oct. 1999.

[114] K. Held. Electronic structure calculations using dynamical mean field theory. Adv. Phys., 56(6):829–926, 2007.

[115] T. Helgaker, P. Jorgensen, and J. Olsen. Molecular electronic-structure theory. John Wiley & Sons, 2014.

[116] C. Hempel, C. Maier, J. Romero, J. McClean, T. Monz, H. Shen, P. Jurcevic, B. P. Lanyon, P. Love, R. Babbush, A. Aspuru-Guzik, R. Blatt, and C. F. Roos. Quantum chemistry calculations on a trapped-ion quantum simulator. Phys. Rev. X, 8(3):031022, July 2018.

[117] M. R. Hermes and L. Gagliardi. Multiconfigurational self-consistent field theory with density matrix embedding: The localized active space self-consistent field method. J. Chem. Theory Comput., 15(2):972–986, Feb. 2019.

[118] O. Higgott, D. Wang, and S. Brierley. Variational quantum computation of excited states. Quantum, 3:156, July 2019.

[119] L. Himanen, A. Geurts, A. S. Foster, and P. Rinke. Data-driven materials science: Status, challenges, and perspectives. Adv. Sci., 6(21):1900808, 2019.

[120] M. Hirayama, T. Miyake, and M. Imada. Derivation of static low-energy effective models by an ab initio downfolding method without double counting of Coulomb correlations: Application to $SrVO_3$, FeSe, and FeTe. Phys. Rev. B, 87(19):195144, May 2013.

[121] M. Hirayama, T. Miyake, M. Imada, and S. Biermann. Low-energy effective Hamiltonians for correlated electron systems beyond density functional theory. Phys. Rev. B, 96(7):075102, Aug. 2017.

[122] J. E. Hirsch. Dynamic Hubbard model. Phys. Rev. Lett., 87(20):206402, Oct. 2001.

[123] K.-H. Hoffmann and Q. Tang. Ginzburg-Landau Phase Transition Theory and Superconductivity. Birkhäuser, 2012.

[124] P. Hohenberg and W. Kohn. Inhomogeneous electron gas. Phys. Rev., 136(3B):B864–B871, Nov. 1964.

[125] Y. H. Hur, J. G. Hoskins, M. Lindsey, E. M. Stoudenmire, and Y. Khoo. Generative modeling via tensor train sketching. arXiv:2202.11788 [cs, math], 2022.

[126] M. Imada, A. Fujimori, and Y. Tokura. Metal-insulator transitions. Rev. Mod. Phys., 70(4):1039–1263, 1998.

[127] S. Iskakov, C.-N. Yeh, E. Gull, and D. Zgid. Ab initio self-energy embedding for the photoemission spectra of NiO and MnO. Phys. Rev. B, 102(8):085105, Aug. 2020.

[128] V. Ivády, I. A. Abrikosov, and A. Gali. First principles calculation of spin-related quantities for point defect qubit research. npj Comput. Mater., 4(1):1–13, Dec. 2018.

[129] C. R. Jacob and J. Neugebauer. Subsystem density-functional theory. WIREs Comput. Mol. Sci., 4(4):325–362, 2014.

[130] B. Jaderberg, A. Agarwal, K. Leonhardt, M. Kiffner, and D. Jaksch. Minimum hardware requirements for hybrid quantum–classical DMFT. Quantum Sci. Technol., 5(3):034015, June 2020.

[131] A. Janotti and C. G. V. de Walle. LDA + U and hybrid functional calculations for defects in ZnO, SnO_2, and TiO_2. Phys. Status Solidi B, 248(4):799–804, 2011.

[132] G. Jindal, H. K. Kisan, and R. B. Sunoj. Mechanistic insights on cooperative catalysis through computational quantum chemical methods. ACS Catal., 5(2):480–503, 2015.

[133] L. O. Jones, M. A. Mosquera, G. C. Schatz, and M. A. Ratner. Embedding methods for quantum chemistry: Applications from materials to life sciences. J. Am. Chem. Soc., 142(7):3281–3295, Feb. 2020.

[134] R. O. Jones. Density functional theory: Its origins, rise to prominence, and future. Rev. Mod. Phys., 87(3):897–923, Aug. 2015.

[135] P. Jordan, J. v. Neumann, and E. Wigner. On an algebraic generalization of the quantum mechanical formalism. Ann. Math., 35(1):29–64, 1934.

[136] M. P. Kaicher, S. B. Jäger, P.-L. Dallaire-Demers, and F. K. Wilhelm. Roadmap for quantum simulation of the fractional quantum Hall effect. Phys. Rev. A, 102(2):022607, Aug. 2020.

[137] A. A. Kananenka, E. Gull, and D. Zgid. Systematically improvable multiscale solver for correlated electron systems. Phys. Rev. B, 91(12):121111, Mar. 2015.

[138] A. A. Kananenka, J. J. Phillips, and D. Zgid. Efficient temperature-dependent Green's functions methods for realistic systems: Compact grids for orthogonal polynomial transforms. J. Chem. Theory Comput., 12(2):564–571, 2016.

[139] A. Kandala, A. Mezzacapo, K. Temme, M. Takita, M. Brink, J. M. Chow, and J. M. Gambetta. Hardware-efficient variational quantum eigensolver for small molecules and quantum magnets. Nature, 549(7671):242–246, Sept. 2017.

[140] A. Kandala, K. Temme, A. D. Córcoles, A. Mezzacapo, J. M. Chow, and J. M. Gambetta. Error mitigation extends the computational reach of a noisy quantum processor. Nature, 567(7749):491–495, Mar. 2019.

[141] M. Karolak, G. Ulm, T. Wehling, V. Mazurenko, A. Poteryaev, and A. Lichtenstein. Double counting in LDA+DMFT—The example of NiO. J. Electron Spectrosc. Relat. Phenom., 181(1):11–15, July 2010.

[142] Y. Kawashima, M. P. Coons, Y. Nam, E. Lloyd, S. Matsuura, A. J. Garza, S. Johri, L. Huntington, V. Senicourt, A. O. Maksymov, J. H. V. Nguyen, J. Kim, N. Alidoust, A. Zaribafiyan, and T. Yamazaki. Efficient and accurate electronic structure simulation demonstrated on a trapped-ion quantum computer. arXiv:2102.07045 [quant-ph], Feb. 2021.

[143] J. Kaye, K. Chen, and O. Parcollet. Discrete Lehmann representation of imaginary time Green's functions. Phys. Rev. B, 105:235115, 2022.

[144] J. Kaye, K. Chen, and H. U. R. Strand. libdlr: Efficient imaginary time calculations using the discrete Lehmann representation. Comput. Phys. Commun., 280:108458, 2022.

[145] J. Kaye and H. U. R. Strand. A fast time domain solver for the equilibrium Dyson equation. arXiv:2110.06120, 2021.

[146] J. Kaye and H. U. R. Strand. libdlr v1.0.0. GitHub repository, 2022.

[147] T. Keen, T. Maier, S. Johnston, and P. Lougovski. Quantum-classical simulation of two-site dynamical mean-field theory on noisy quantum hardware. Quantum Sci. Technol., 5(3):035001, Apr. 2020.

[148] P. Kehayias, M. W. Doherty, D. English, R. Fischer, A. Jarmola, K. Jensen, N. Leefer, P. Hemmer, N. B. Manson, and D. Budker. Infrared absorption band and vibronic

structure of the nitrogen-vacancy center in diamond. Phys. Rev. B, 88(16):165202, Oct. 2013.

[149] P. R. C. Kent and G. Kotliar. Toward a predictive theory of correlated materials. Science, 361(6400):348–354, July 2018.

[150] Y. Khoo, M. Lindsey, and H. Zhao. Tensorizing flows: a tool for variational inference. arXiv:2305.02460, 2023.

[151] M. Kinza and C. Honerkamp. Low-energy effective interactions beyond the constrained random-phase approximation by the functional renormalization group. Phys. Rev. B, 92(4):045113, July 2015.

[152] I. D. Kivlichan, C. Gidney, D. W. Berry, N. Wiebe, J. McClean, W. Sun, Z. Jiang, N. Rubin, A. Fowler, A. Aspuru-Guzik, H. Neven, and R. Babbush. Improved fault-tolerant quantum simulation of condensed-phase correlated electrons via trotterization. Quantum, 4:296, July 2020.

[153] G. Knizia and G. K.-L. Chan. Density matrix embedding: A simple alternative to dynamical mean-field theory. Phys. Rev. Lett., 109(18):186404, Nov. 2012.

[154] G. Knizia and G. K.-L. Chan. Density matrix embedding: A strong-coupling quantum embedding theory. J. Chem. Theory Comput., 9(3):1428–1432, Mar. 2013.

[155] W. Kohn and L. J. Sham. Self-consistent equations including exchange and correlation effects. Phys. Rev., 140(4A):A1133–A1138, Nov. 1965.

[156] G. Kotliar, S. Y. Savrasov, K. Haule, V. S. Oudovenko, O. Parcollet, and C. A. Marianetti. Electronic structure calculations with dynamical mean-field theory. Rev. Mod. Phys., 78(3):865–951, Aug. 2006.

[157] G. Kotliar, S. Y. Savrasov, G. Pálsson, and G. Biroli. Cellular Dynamical Mean Field Approach to Strongly Correlated Systems. Phys. Rev. Lett., 87(18):186401, Oct. 2001.

[158] J. M. Kreula, L. García-Álvarez, L. Lamata, S. R. Clark, E. Solano, and D. Jaksch. Few-qubit quantum-classical simulation of strongly correlated lattice fermions. EPJ Quantum Technol., 3(1):1–19, Dec. 2016.

[159] I. S. Krivenko and S. Biermann. Slave rotor approach to dynamically screened Coulomb interactions in solids. Phys. Rev. B, 91(15):155149, Apr. 2015.

[160] A. Krylov, T. L. Windus, T. Barnes, E. Marin-Rimoldi, J. A. Nash, B. Pritchard, D. G. A. Smith, D. Altarawy, P. Saxe, C. Clementi, T. D. Crawford, R. J. Harrison, S. Jha, V. S. Pande, and T. Head-Gordon. Perspective: Computational chemistry software and its advancement as illustrated through three grand challenge cases for molecular science. J. Chem. Phys., 149(18):180901, Nov. 2018.

[161] W. Ku and A. G. Eguiluz. Band-gap problem in semiconductors revisited: Effects of core states and many-body self-consistency. Phys. Rev. Lett., 89:126401, 2002.

[162] T. N. Lan, A. A. Kananenka, and D. Zgid. Communication: Towards ab initio self-energy embedding theory in quantum chemistry. J. Chem. Phys., 143(24):241102, Dec. 2015.

[163] T. N. Lan, A. Shee, J. Li, E. Gull, and D. Zgid. Testing self-energy embedding theory in combination with GW. Phys. Rev. B, 96(15):155106, Oct. 2017.

[164] T. N. Lan and D. Zgid. Generalized self-energy embedding theory. J. Chem. Phys. Lett., 8(10):2200–2205, May 2017.

[165] B. P. Lanyon, J. D. Whitfield, G. G. Gillett, M. E. Goggin, M. P. Almeida, I. Kassal, J. D. Biamonte, M. Mohseni, B. J. Powell, M. Barbieri, A. Aspuru-Guzik, and A. G. White. Towards quantum chemistry on a quantum computer. Nat. Chem., 2(2):106–111, Feb. 2010.

[166] B. T. G. Lau, G. Knizia, and T. C. Berkelbach. Regional embedding enables high-level quantum chemistry for surface science. J. Chem. Phys. Lett., 12(3):1104–1109, Jan. 2021.

[167] J. Lebreuilly, K. Noh, C.-H. Wang, S. M. Girvin, and L. Jiang. Autonomous quantum error correction and quantum computation. arXiv:2103.05007 [quant-ph], Mar. 2021.

[168] J. Lee and K. Haule. Diatomic molecule as a testbed for combining DMFT with electronic structure methods such as GW and DFT. Phys. Rev. B, 95(15):155104, Apr. 2017.

[169] P. A. Lee, N. Nagaosa, and X.-G. Wen. Doping a mott insulator: Physics of high-temperature superconductivity. Rev. Mod. Phys., 78(1):17–85, 2006.

[170] J. Li, M. Wallerberger, N. Chikano, C.-N. Yeh, E. Gull, and H. Shinaoka. Sparse sampling approach to efficient ab initio calculations at finite temperature. Phys. Rev. B, 101(3):035144, 2020.

[171] Z. Li, X. Liu, H. Wang, S. Ashhab, J. Cui, H. Chen, X. Peng, and J. Du. Quantum simulation of resonant transitions for solving the eigenproblem of an effective water Hamiltonian. Phys. Rev. Lett., 122(9):090504, Mar. 2019.

[172] Z. Li, M.-H. Yung, H. Chen, D. Lu, J. D. Whitfield, X. Peng, A. Aspuru-Guzik, and J. Du. Solving quantum ground-state problems with nuclear magnetic resonance. Sci. Rep., 1(1):88, Sept. 2011.

[173] F. Libisch, C. Huang, and E. A. Carter. Embedded correlated wavefunction schemes: Theory and applications. Acc. Chem. Res., 47(9):2768–2775, Sept. 2014.

[174] A. I. Lichtenstein and M. I. Katsnelson. Ab initio calculations of quasiparticle band structure in correlated systems: LDA++ approach. Phys. Rev. B, 57(12):6884–6895, Mar. 1998.

[175] C.-K. Lin, Y.-H. Wang, H.-C. Chang, M. Hayashi, and S. H. Lin. One- and two-photon absorption properties of diamond nitrogen-vacancy defect centers: A theoretical study. J. Chem. Phys., 129(12):124714, Sept. 2008.

[176] H. Lin and D. G. Truhlar. QM/MM: What have we learned, where are we, and where do we go from here? Theor. Chem. Acc., 117(2):185, July 2006.

[177] N. Lin. Dynamical mean-field theory for quantum chemistry. Phys. Rev. Lett., 106(9), 2011.

[178] H. Lischka, D. Nachtigallová, A. J. A. Aquino, P. G. Szalay, F. Plasser, F. B. C. Machado, and M. Barbatti. Multireference approaches for excited states of molecules. Chem. Rev., 118(15):7293–7361, jul 2018.

[179] H. Liu, G. H. Low, D. S. Steiger, T. Häner, M. Reiher, and M. Troyer. Prospects of quantum computing for molecular sciences. arXiv:2102.10081 [quant-ph], Feb. 2021.

[180] J. Liu, L. Wan, Z. Li, and J. Yang. Simulating periodic systems on a quantum computer using molecular orbitals. J. Chem. Theory Comput., 16(11):6904–6914, Nov. 2020.

[181] M. Liu, Y. Wang, Y. Chen, M. J. Field, and J. Gao. QM/MM through the 1990s: The First Twenty Years of Method Development and Applications. Isr. J. Chem., 54(8-9):1250–1263, 2014.

[182] Y. Liu and Z.-Q. Mao. Unconventional superconductivity in Sr_2RuO_4. Phys. C: Supercond. Appl., 514:339–353, 2015.

[183] J. H. N. Loubser and J. A. van Wyk. Electron spin resonance in the study of diamond. Rep. Prog. Phys., 41(8):1201–1248, Aug. 1978.

[184] C. Lupo, F. Jamet, T. Tse, I. Rungger, and C. Weber. Maximally Localized Dynamical Quantum Embedding for Solving Many-Body Correlated Systems. arXiv:2008.04281 [cond-mat], Feb. 2021.

[185] H. Ma, M. Govoni, and G. Galli. Quantum simulations of materials on near-term quantum computers. npj Comput. Mater., 6(1):1–8, July 2020.

[186] H. Ma, M. Govoni, F. Gygi, and G. Galli. A finite-field approach for GW calculations beyond the random phase approximation. J. Chem. Theory Comput., 15(1):154–164, Jan. 2019.

[187] H. Ma, N. Sheng, M. Govoni, and G. Galli. First-principles studies of strongly correlated states in defect spin qubits in diamond. Phys. Chem. Chem. Phys., 22(44):25522–25527, Nov. 2020.

[188] H. Ma, N. Sheng, M. Govoni, and G. Galli. Quantum embedding theory for strongly correlated states in materials. J. Chem. Theory Comput., 17(4):2116–2125, Apr. 2021.

[189] Y. Ma, M. Rohlfing, and A. Gali. Excited states of the negatively charged nitrogen-vacancy color center in diamond. Phys. Rev. B, 81(4):041204, Jan. 2010.

[190] A. Macridin, P. Spentzouris, J. Amundson, and R. Harnik. Electron-phonon systems on a universal quantum computer. Phys. Rev. Lett., 121(11):110504, Sept. 2018.

[191] F. Mancini, M. Marinaro, and Y. Nakano. Exact results for the Anderson model in the limit of zero-width conduction band. Physica B: Condens. Matter., 159(3):330–360, Sept. 1989.

[192] N. Mardirossian and M. Head-Gordon. Thirty years of density functional theory in computational chemistry: An overview and extensive assessment of 200 density functionals. Mol. Phys., 115(19):2315–2372, Oct. 2017.

[193] F. Marsiglio, R. Teshima, and J. E. Hirsch. Dynamic Hubbard model: Effect of finite boson frequency. Phys. Rev. B, 68(22):224507, Dec. 2003.

[194] R. M. Martin. Electronic structure: basic theory and practical methods. Cambridge university press, 2020.

[195] R. M. Martin, L. Reining, and D. M. Ceperley. Interacting electrons. Cambridge University Press, 2016.

[196] R. J. Maurer, C. Freysoldt, A. M. Reilly, J. G. Brandenburg, O. T. Hofmann, T. Björkman, S. Lebègue, and A. Tkatchenko. Advances in density-functional calculations for materials modeling. Annu. Rev. Mater. Res., 49(1):1–30, 2019.

[197] J. R. Maze, A. Gali, E. Togan, Y. Chu, A. Trifonov, E. Kaxiras, and M. D. Lukin. Properties of nitrogen-vacancy centers in diamond: the group theoretic approach. New J. Phys., 13(2):025025, feb 2011.

[198] S. McArdle, S. Endo, A. Aspuru-Guzik, S. C. Benjamin, and X. Yuan. Quantum computational chemistry. Rev. Mod. Phys., 92(1):015003, Mar. 2020.

[199] A. J. McCaskey, Z. P. Parks, J. Jakowski, S. V. Moore, T. D. Morris, T. S. Humble, and R. C. Pooser. Quantum chemistry as a benchmark for near-term quantum computers. Npj Quantum Inf., 5(1):1–8, Nov. 2019.

[200] J. R. McClean, J. Romero, R. Babbush, and A. Aspuru-Guzik. The theory of variational hybrid quantum-classical algorithms. New. J. Phys., 18(2):023023, Feb. 2016.

[201] J. R. McClean, N. C. Rubin, K. J. Sung, I. D. Kivlichan, X. Bonet-Monroig, Y. Cao, C. Dai, E. S. Fried, C. Gidney, B. Gimby, P. Gokhale, T. Häner, T. Hardikar, V. Havlíček, O. Higgott, C. Huang, J. Izaac, Z. Jiang, X. Liu, S. McArdle, M. Neeley, T. O'Brien, B. O'Gorman, I. Ozfidan, M. D. Radin, J. Romero, N. P. D. Sawaya, B. Senjean,

K. Setia, S. Sim, D. S. Steiger, M. Steudtner, Q. Sun, W. Sun, D. Wang, F. Zhang, and R. Babbush. OpenFermion: The electronic structure package for quantum computers. Quantum Sci. Technol., 5(3):034014, June 2020.

[202] D. Medvedeva, S. Iskakov, F. Krien, V. V. Mazurenko, and A. I. Lichtenstein. Exact diagonalization solver for extended dynamical mean-field theory. Phys. Rev. B, 96(23):235149, Dec. 2017.

[203] F. Mei, Q. Guo, Y.-F. Yu, L. Xiao, S.-L. Zhu, and S. Jia. Digital Simulation of Topological Matter on Programmable Quantum Processors. Phys. Rev. Lett., 125(16):160503, Oct. 2020.

[204] C. Mejuto-Zaera, L. Zepeda-Núñez, M. Lindsey, N. Tubman, B. Whaley, and L. Lin. Efficient hybridization fitting for dynamical mean-field theory via semi-definite relaxation. Phys. Rev. B, 101(3):035143, Jan. 2020.

[205] C. Melnick, P. Sémon, K. Yu, N. D'Imperio, A.-M. Tremblay, and G. Kotliar. Accelerated impurity solver for DMFT and its diagrammatic extensions. Comput. Phys. Commun., 267:108075, Oct. 2021.

[206] M. Metcalf, N. P. Bauman, K. Kowalski, and W. A. de Jong. Resource-efficient chemistry on quantum computers with the variational quantum eigensolver and the double unitary coupled-cluster approach. J. Chem. Theory Comput., 16(10):6165–6175, Oct. 2020.

[207] A. Mitra, H. Q. Pham, R. Pandharkar, M. R. Hermes, and L. Gagliardi. Excited States of Crystalline Point Defects with Multireference Density Matrix Embedding Theory. J. Phys. Chem. Lett., 12(48):11688–11694, Dec. 2021.

[208] T. Miyake and F. Aryasetiawan. Screened Coulomb interaction in the maximally localized Wannier basis. Phys. Rev. B, 77(8):085122, Feb. 2008.

[209] K. Mizuta, M. Fujii, S. Fujii, K. Ichikawa, Y. Imamura, Y. Okuno, and Y. O. Nakagawa. Deep variational quantum eigensolver for excited states and its application to quantum chemistry calculation of periodic materials. arXiv:2104.00855 [cond-mat, physics:quant-ph], Apr. 2021.

[210] A. Montanaro and S. Stanisic. Compressed variational quantum eigensolver for the Fermi-Hubbard model. arXiv:2006.01179 [quant-ph], June 2020.

[211] A. A. Mostofi, J. R. Yates, Y.-S. Lee, I. Souza, D. Vanderbilt, and N. Marzari. wannier90: A tool for obtaining maximally-localised Wannier functions. Comput. Phys. Commun., 178(9):685 – 699, 2008.

[212] M. Motta, C. Sun, A. T. K. Tan, M. J. O'Rourke, E. Ye, A. J. Minnich, F. G. S. L. Brandão, and G. K.-L. Chan. Determining eigenstates and thermal states on a quantum computer using quantum imaginary time evolution. Nat. Phys., 16(2):205–210, Feb. 2020.

[213] L. Muechler, D. I. Badrtdinov, A. Hampel, J. Cano, M. Rösner, and C. E. Dreyer. Quantum embedding methods for correlated excited states of point defects: Case studies and challenges. Phys. Rev. B, 105(23):235104, 2022.

[214] Y. Nagai and H. Shinaoka. Sparse modeling approach for quasiclassical theory of superconductivity. arXiv:2205.14800, 2022.

[215] Y. Nam, J.-S. Chen, N. C. Pisenti, K. Wright, C. Delaney, D. Maslov, K. R. Brown, S. Allen, J. M. Amini, J. Apisdorf, K. M. Beck, A. Blinov, V. Chaplin, M. Chmielewski, C. Collins, S. Debnath, K. M. Hudek, A. M. Ducore, M. Keesan, S. M. Kreikemeier, J. Mizrahi, P. Solomon, M. Williams, J. D. Wong-Campos, D. Moehring, C. Monroe, and J. Kim. Ground-state energy estimation of the water molecule on a trapped-ion quantum computer. Npj Quantum Inf., 6(1):1–6, Apr. 2020.

[216] J. Neugebauer and T. Hickel. Density functional theory in materials science. WIREs Comput. Mol. Sci., 3(5):438–448, 2013.

[217] H.-V. Nguyen, T. A. Pham, D. Rocca, and G. Galli. Improving accuracy and efficiency of calculations of photoemission spectra within the many-body perturbation theory. Phys. Rev. B, 85(8):081101, Feb. 2012.

[218] N. L. Nguyen, H. Ma, M. Govoni, F. Gygi, and G. Galli. Finite-field approach to solving the Bethe-Salpeter equation. Phys. Rev. Lett., 122(23):237402, June 2019.

[219] M. A. Nielsen and I. L. Chuang. Quantum Computation and Quantum Information: 10th Anniversary Edition. Cambridge University Press, Cambridge, 2010.

[220] F. Nilsson and F. Aryasetiawan. Recent progress in first-principles methods for computing the electronic structure of correlated materials. Computation, 6(1):26, Mar. 2018.

[221] F. Nilsson, L. Boehnke, P. Werner, and F. Aryasetiawan. Multitier self-consistent GW+EDMFT. Phys. Rev. Mater., 1(4):043803, Sept. 2017.

[222] P. J. J. O'Malley, R. Babbush, I. D. Kivlichan, J. Romero, J. R. McClean, R. Barends, J. Kelly, P. Roushan, A. Tranter, N. Ding, B. Campbell, Y. Chen, Z. Chen, B. Chiaro, A. Dunsworth, A. G. Fowler, E. Jeffrey, E. Lucero, A. Megrant, J. Y. Mutus, M. Neeley, C. Neill, C. Quintana, D. Sank, A. Vainsencher, J. Wenner, T. C. White, P. V. Coveney, P. J. Love, H. Neven, A. Aspuru-Guzik, and J. M. Martinis. Scalable quantum simulation of molecular energies. Phys. Rev. X, 6(3):031007, July 2016.

[223] G. Onida, L. Reining, and A. Rubio. Electronic excitations: Density-functional versus many-body Green's-function approaches. Rev. Mod. Phys., 74(2):601–659, June 2002.

[224] G. Onida, L. Reining, and A. Rubio. Electronic excitations: density-functional versus many-body Green's-function approaches. Rev. Mod. Phys., 74(2):601–659, June 2002.

[225] G. Ortiz, J. E. Gubernatis, E. Knill, and R. Laflamme. Quantum algorithms for fermionic simulations. Phys. Rev. A, 64(2):022319, July 2001.

[226] R. Orús. A practical introduction to tensor networks: Matrix product states and projected entangled pair states. Ann. Phys., 349:117–158, 2014.

[227] R. Orús. Tensor networks for complex quantum systems. Nat. Rev. Phys., 1(9):538–550, 2019. Number: 9 Publisher: Nature Publishing Group.

[228] I. V. Oseledets. Tensor-train decomposition. SIAM J. Sci. Comput., 33(5):2295–2317, 2011. Publisher: Society for Industrial and Applied Mathematics.

[229] O. Parcollet, M. Ferrero, T. Ayral, H. Hafermann, I. Krivenko, L. Messio, and P. Seth. TRIQS: A toolbox for research on interacting quantum systems. Comput. Phys. Commun., 196:398–415, 2015.

[230] E. Pavarini. Electronic structure calculations with LDA+DMFT. In V. Bach and L. Delle Site, editors, Many-Electron Approaches in Physics, Chemistry and Mathematics: A Multidisciplinary View, Mathematical Physics Studies, pages 321–341. Springer International Publishing, Cham, 2014.

[231] Y. Peng, Y. Chen, E. M. Stoudenmire, and Y. Khoo. Generative modeling via hierarchical tensor sketching. arXiv:2304.05305 [cs, math, stat], 2023.

[232] J. P. Perdew, K. Burke, and M. Ernzerhof. Generalized gradient approximation made simple. Phys. Rev. Lett., 77(18):3865–3868, oct 1996.

[233] A. Peruzzo, J. McClean, P. Shadbolt, M.-H. Yung, X.-Q. Zhou, P. J. Love, A. Aspuru-Guzik, and J. L. O'Brien. A variational eigenvalue solver on a photonic quantum processor. Nat. Comm., 5(1):4213, July 2014.

[234] F. Petocchi, F. Nilsson, F. Aryasetiawan, and P. Werner. Screening from e_g states and antiferromagnetic correlations in $d^{(1,2,3)}$ perovskites: A GW+EDMFT investigation. Phys. Rev. Res., 2(1):013191, Feb. 2020.

[235] S. Pezeshki and H. Lin. Recent developments in QM/MM methods towards open-boundary multi-scale simulations. Mol. Simul., 41(1-3):168–189, Feb. 2015.

[236] W. Pfäffle, D. Antonov, J. Wrachtrup, and G. Bester. Screened configuration interaction method for open-shell excited states applied to NV centers. Phys. Rev. B, 104(10):104105, Sept. 2021.

[237] H. Q. Pham, V. Bernales, and L. Gagliardi. Can density matrix embedding theory with the complete activate space self-consistent field solver describe single and double bond breaking in molecular systems? J. Chem. Theory Comput., 14(4):1960–1968, Apr. 2018.

[238] H. Q. Pham, M. R. Hermes, and L. Gagliardi. Periodic electronic structure calculations with the density matrix embedding theory. J. Chem. Theory Comput., 16(1):130–140, Jan. 2020.

[239] T. A. Pham, M. Govoni, R. Seidel, S. E. Bradforth, E. Schwegler, and G. Galli. Electronic structure of aqueous solutions: Bridging the gap between theory and experiments. Science Advances, 3(6):e1603210, June 2017.

[240] T. A. Pham, H.-V. Nguyen, D. Rocca, and G. Galli. GW calculations using the spectral decomposition of the dielectric matrix: Verification, validation, and comparison of methods. Phys. Rev. B, 87(15):155148, Apr. 2013.

[241] J. Preskill. Quantum computing in the NISQ era and beyond. Quantum, 2:79, Aug. 2018.

[242] D. Y. Qiu, F. H. da Jornada, and S. G. Louie. Solving the Bethe-Salpeter equation on a subspace: Approximations and consequences for low-dimensional materials. Phys. Rev. B, 103(4):045117, Jan. 2021.

[243] A. Rahmani, K. J. Sung, H. Putterman, P. Roushan, P. Ghaemi, and Z. Jiang. Creating and Manipulating a Laughlin-Type $\nu = 1/3$ Fractional Quantum Hall State on a Quantum Computer with Linear Depth Circuits. PRX Quantum, 1(2):020309, Nov. 2020.

[244] L. Reining. The GW approximation: Content, successes and limitations. WIREs Comput. Mol. Sci., 8(3):e1344, 2018.

[245] Y. Ren, H. Zhao, Y. Khoo, and L. Ying. High-dimensional density estimation with tensorizing flow. arXiv:2212.00759 [physics, stat], 2022.

[246] L. J. Rogers, S. Armstrong, M. J. Sellars, and N. B. Manson. Infrared emission of the NV centre in diamond: Zeeman and uniaxial stress studies. New J. Phys., 10(10):103024, oct 2008.

[247] M. Rossmannek, P. K. Barkoutsos, P. J. Ollitrault, and I. Tavernelli. Quantum HF/DFT-embedding algorithms for electronic structure calculations: Scaling up to complex molecular systems. J. Chem. Phys., 154(11):114105, Mar. 2021.

[248] N. C. Rubin. A hybrid classical/quantum approach for large-scale studies of quantum systems with density matrix embedding theory. arXiv:1610.06910 [cond-mat, physics:quant-ph], Oct. 2016.

[249] I. Rungger, N. Fitzpatrick, H. Chen, C. H. Alderete, H. Apel, A. Cowtan, A. Patterson, D. M. Ramo, Y. Zhu, N. H. Nguyen, E. Grant, S. Chretien, L. Wossnig, N. M. Linke, and R. Duncan. Dynamical mean field theory algorithm and experiment on quantum computers. arXiv:1910.04735 [cond-mat, physics:quant-ph], Jan. 2020.

[250] A. A. Rusakov, S. Iskakov, L. N. Tran, and D. Zgid. Self-energy embedding theory (SEET) for periodic systems. J. Chem. Theory Comput., 15(1):229–240, Jan. 2019.

[251] I. G. Ryabinkin, T.-C. Yen, S. N. Genin, and A. F. Izmaylov. Qubit coupled cluster method: A systematic approach to quantum chemistry on a quantum computer. J. Chem. Theory Comput., 14(12):6317–6326, Dec. 2018.

[252] S. S. Dong, M. Govoni, and G. Galli. Machine learning dielectric screening for the simulation of excited state properties of molecules and materials. Chem. Sci., 12(13):4970–4980, 2021.

[253] R. Sagastizabal, X. Bonet-Monroig, M. Singh, M. A. Rol, C. C. Bultink, X. Fu, C. H. Price, V. P. Ostroukh, N. Muthusubramanian, A. Bruno, M. Beekman, N. Haider, T. E. O'Brien, and L. DiCarlo. Experimental error mitigation via symmetry verification in a variational quantum eigensolver. Phys. Rev. A, 100(1):010302, July 2019.

[254] R. Sakuma, C. Martins, T. Miyake, and F. Aryasetiawan. Ab initio study of the downfolded self-energy for correlated systems: Momentum dependence and effects of dynamical screening. Phys. Rev. B, 89(23):235119, June 2014.

[255] R. Sakuma, P. Werner, and F. Aryasetiawan. Electronic structure of $SrVO_3$ within GW+DMFT. Phys. Rev. B, 88(23):235110, Dec. 2013.

[256] E. E. Salpeter and H. A. Bethe. A Relativistic Equation for Bound-State Problems. Phys. Rev., 84(6):1232–1242, Dec. 1951.

[257] R. Santagati, J. Wang, A. A. Gentile, S. Paesani, N. Wiebe, J. R. McClean, S. Morley-Short, P. J. Shadbolt, D. Bonneau, J. W. Silverstone, D. P. Tew, X. Zhou, J. L. O'Brien, and M. G. Thompson. Witnessing eigenstates for quantum simulation of Hamiltonian spectra. Science Advances, 4(1):eaap9646, Jan. 2018.

[258] D. Savostyanov and I. Oseledets. Fast adaptive interpolation of multi-dimensional arrays in tensor train format. In The 2011 International Workshop on Multidimensional (nD) Systems, pages 1–8, 2011.

[259] T. Schäfer, F. Libisch, G. Kresse, and A. Grüneis. Local embedding of coupled cluster theory into the random phase approximation using plane waves. J. Chem. Phys., 154(1):011101, Jan. 2021.

[260] P. Scherpelz, M. Govoni, I. Hamada, and G. Galli. Implementation and validation of fully relativistic GW calculations: Spin-orbit coupling in molecules, nanocrystals, and solids. J. Chem. Theory Comput., 12(8):3523–3544, Aug. 2016.

[261] G. R. Schleder, A. C. M. Padilha, C. M. Acosta, M. Costa, and A. Fazzio. From DFT to machine learning: Recent approaches to materials science–a review. J. Phys. Mater., 2(3):032001, May 2019.

[262] M. Schlipf and F. Gygi. Optimization algorithm for the generation of ONCV pseudopotentials. Comput. Phys. Commun., 196:36–44, nov 2015.

[263] U. Schollwöck. The density-matrix renormalization group. Rev. Mod. Phys., 77(1):259–315, 2005.

[264] U. Schollwöck. The density-matrix renormalization group in the age of matrix product states. Ann. Phys., 326(1):96–192, 2011.

[265] H. M. Senn and W. Thiel. QM/MM Methods for Biomolecular Systems. Angew. Chem. Int. Ed., 48(7):1198–1229, 2009.

[266] H. Seo, M. Govoni, and G. Galli. Design of defect spins in piezoelectric aluminum nitride for solid-state hybrid quantum technologies. Sci. Rep., 6(1):20803, Feb. 2016.

[267] H. Seo, H. Ma, M. Govoni, and G. Galli. Designing defect-based qubit candidates in wide-gap binary semiconductors for solid-state quantum technologies. Phys. Rev. Mater., 1(7):075002, Dec. 2017.

[268] P. Seth, I. Krivenko, M. Ferrero, and O. Parcollet. TRIQS/CTHYB: A continuous-time quantum Monte Carlo hybridisation expansion solver for quantum impurity problems. Comput. Phys. Commun., 200:274 – 284, 2016.

[269] P. Seth, I. Krivenko, M. Ferrero, and O. Parcollet. TRIQS/CTHYB: A continuous-time quantum Monte Carlo hybridisation expansion solver for quantum impurity problems. Comput. Phys. Commun., 200:274–284, Mar. 2016.

[270] A. Shee and D. Zgid. Coupled cluster as an impurity solver for Green's function embedding methods. J. Chem. Theory Comput., 15(11):6010–6024, Nov. 2019.

[271] Y. Shen, X. Zhang, S. Zhang, J.-N. Zhang, M.-H. Yung, and K. Kim. Quantum implementation of the unitary coupled cluster for simulating molecular electronic structure. Phys. Rev. A, 95(2):020501, Feb. 2017.

[272] N. Sheng, A. Hampel, S. Beck, O. Parcollet, N. Wentzell, J. Kaye, and K. Chen. Low-rank green's function representations applied to dynamical mean-field theory. Phys. Rev. B, 107(24):245123, 2023.

[273] N. Sheng, C. Vorwerk, M. Govoni, and G. Galli. Green's function formulation of quantum defect embedding theory. J. Chem. Theory Comput., 18(6):3512–3522, 2022.

[274] A. Sherman. Hubbard-Kanamori model: Spectral functions, negative electron compressibility, and susceptibilities. Phys. Scr., 95(9):095804, Aug. 2020.

[275] H. Shinaoka, J. Otsuki, M. Ohzeki, and K. Yoshimi. Compressing Green's function using intermediate representation between imaginary-time and real-frequency domains. Phys. Rev. B, 96(3):035147, 2017.

[276] R. N. Silver, D. S. Sivia, and J. E. Gubernatis. Maximum-entropy method for analytic continuation of quantum Monte Carlo data. Phys. Rev. B, 41:2380–2389, 1990.

[277] Simons Collaboration on the Many-Electron Problem, K. T. Williams, Y. Yao, J. Li, L. Chen, H. Shi, M. Motta, C. Niu, U. Ray, S. Guo, R. J. Anderson, J. Li, L. N. Tran, C.-N. Yeh, B. Mussard, S. Sharma, F. Bruneval, M. van Schilfgaarde, G. H. , G. K.-L. Chan, S. Zhang, E. Gull, D. Zgid, A. Millis, C. J. Umrigar, and L. K. Wagner. Direct comparison of many-body methods for realistic electronic Hamiltonians. Phys. Rev. X, 10(1):011041, Feb. 2020.

[278] V. Singh, U. Herath, B. Wah, X. Liao, A. H. Romero, and H. Park. DMFTwDFT: An open-source code combining dynamical mean field theory with various density functional theory packages. arXiv:2002.00068 [cond-mat], Jan. 2020.

[279] J. H. Skone, M. Govoni, and G. Galli. Self-consistent hybrid functional for condensed systems. Phys. Rev. B, 89:195112, May 2014.

[280] J. H. Skone, M. Govoni, and G. Galli. Nonempirical range-separated hybrid functionals for solids and molecules. Phys. Rev. B, 93:235106, Jun 2016.

[281] S. E. Smart and D. A. Mazziotti. Quantum-classical hybrid algorithm using an error-mitigating N-representability condition to compute the Mott metal-insulator transition. Phys. Rev. A, 100(2):022517, Aug. 2019.

[282] J. L. Smith and Q. Si. Spatial correlations in dynamical mean-field theory. Phys. Rev. B, 61(8):5184–5193, Feb. 2000.

[283] J. Souto-Casares, N. A. Spaldin, and C. Ederer. DFT+DMFT study of oxygen vacancies in a Mott insulator. Phys. Rev. B, 100(8):085146, Aug. 2019.

[284] J. Souto-Casares, N. A. Spaldin, and C. Ederer. Oxygen vacancies in strontium titanate: A dft+dmft study. Phys. Rev. Res., 3(2):023027, Apr. 2021.

[285] A. Splendiani, L. Sun, Y. Zhang, T. Li, J. Kim, C.-Y. Chim, G. Galli, and F. Wang. Emerging photoluminescence in monolayer MoS2. Nano Lett., 10(4):1271–1275, Apr. 2010.

[286] G. Strinati. Application of the green's functions method to the study of the optical properties of semiconductors. Riv. Nuovo Cimento, 11(12):1–86, 1988.

[287] P. Sun and G. Kotliar. Extended dynamical mean-field theory and GW method. Phys. Rev. B, 66(8):085120, Aug. 2002.

[288] Q. Sun, T. C. Berkelbach, N. S. Blunt, G. H. Booth, S. Guo, Z. Li, J. Liu, J. D. McClain, E. R. Sayfutyarova, S. Sharma, S. Wouters, and G. K.-L. Chan. PySCF: The Python-based simulations of chemistry framework. WIREs Comput. Mol. Sci., 8(1):e1340, 2018.

[289] Q. Sun and G. K.-L. Chan. Quantum embedding theories. Acc. Chem. Res., 49(12):2705–2712, Dec. 2016.

[290] S. H. Sureshbabu, M. Sajjan, S. Oh, and S. Kais. Implementation of Quantum Machine Learning for Electronic Structure Calculations of Periodic Systems on Quantum Computing Devices. J. Chem. Inf. Model, June 2021.

[291] J. E. Sutton and D. G. Vlachos. Building large microkinetic models with first-principles' accuracy at reduced computational cost. Chem. Eng. Sci., 121:190–199, Jan. 2015.

[292] A. Szabo and N. S. Ostlund. Modern quantum chemistry: introduction to advanced electronic structure theory. Courier Corporation, 2012.

[293] X. Tang, Y. Hur, Y. Khoo, and L. Ying. Generative modeling via tree tensor network states. arXiv:2209.01341 [quant-ph, stat], 2022.

[294] J. Terzic, H. Zheng, F. Ye, H. D. Zhao, P. Schlottmann, L. E. De Long, S. J. Yuan, and G. Cao. Evidence for a low-temperature magnetic ground state in double-perovskite iridates with $Ir^{5+}(5d^4)$ ions. Phys. Rev. B, 96:064436, 2017.

[295] G. Thiering and A. Gali. Ab initio magneto-optical spectrum of group-iv vacancy color centers in diamond. Phys. Rev. X, 8:021063, Jun 2018.

[296] G. Thiering and A. Gali. The (eg $\otimes$ eu) $\otimes$ eg product jahn–teller effect in the neutral group-IV vacancy quantum bits in diamond. npj Comput. Mater., 5(1):18, feb 2019.

[297] J. Tilly, P. V. Sriluckshmy, A. Patel, E. Fontana, I. Rungger, E. Grant, R. Anderson, J. Tennyson, and G. H. Booth. Reduced Density Matrix Sampling: Self-consistent Embedding and Multiscale Electronic Structure on Current Generation Quantum Computers. arXiv:2104.05531 [physics, physics:quant-ph], Apr. 2021.

[298] J. M. Tomczak, M. Casula, T. Miyake, F. Aryasetiawan, and S. Biermann. Combined GW and dynamical mean-field theory: Dynamical screening effects in transition metal oxides. Europhys. Lett., 100(6):67001, Dec. 2012.

[299] J. M. Tomczak, M. Casula, T. Miyake, and S. Biermann. Asymmetry in band widening and quasiparticle lifetimes in $SrVO_3$: Competition between screened exchange and local correlations from combined GW and dynamical mean-field theory GW+DMFT. Phys. Rev. B, 90(16):165138, Oct. 2014.

[300] J. M. Tomczak, P. Liu, A. Toschi, G. Kresse, and K. Held. Merging GW with DMFT and non-local correlations beyond. Eur. Phys. J.: Spec. Top., 226(11):2565–2590, July 2017.

[301] G. Trimarchi, I. Leonov, N. Binggeli, D. Korotin, and V. I. Anisimov. LDA+DMFT implemented with the pseudopotential plane-wave approach. J. Phys. Condens. Matter, 20(13):135227, Mar. 2008.

[302] V. Turkowski, A. Kabir, N. Nayyar, and T. S. Rahman. Dynamical mean-field theory for molecules and nanostructures. J. Chem. Phys., 136(11):114108, Mar. 2012.

[303] P. Umari, G. Stenuit, and S. Baroni. GW quasiparticle spectra from occupied states only. Phys. Rev. B, 81:115104, Mar 2010.

[304] A. Uvarov, J. D. Biamonte, and D. Yudin. Variational quantum eigensolver for frustrated quantum systems. Phys. Rev. B, 102(7):075104, Aug. 2020.

[305] M. van Schilfgaarde, T. Kotani, and S. Faleev. Quasiparticle Self-Consistent G W Theory. Phys. Rev. Lett., 96(22):226402, June 2006.

[306] P. Verma and D. G. Truhlar. Status and challenges of density functional theory. Trends Chem., 2(4):302–318, Apr. 2020.

[307] F. Verstraete and J. I. Cirac. Mapping local Hamiltonians of fermions to local Hamiltonians of spins. J. Stat. Mech. Theory Exp., 2005(09):P09012–P09012, Sept. 2005.

[308] H. Vo, S. Zhang, W. Wang, and G. Galli. Lessons learned from first-principles calculations of transition metal oxides. J. Chem. Phys., 154(17):174704, May 2021.

[309] D. Vollhardt. Dynamical mean-field theory of electronic correlations in models and materials. AIP Conf. Proc., 1297(1):339, Nov. 2010.

[310] D. Vollhardt, K. Byczuk, and M. Kollar. Dynamical mean-field theory. In A. Avella and F. Mancini, editors, Strongly Correlated Systems: Theoretical Methods, Springer Series in Solid-State Sciences, pages 203–236. Springer, Berlin, Heidelberg, 2012.

[311] V. von Burg, G. H. Low, T. Häner, D. S. Steiger, M. Reiher, M. Roetteler, and M. Troyer. Quantum computing enhanced computational catalysis. arXiv:2007.14460 [physics, physics:quant-ph], Mar. 2021.

[312] C. Vorwerk, N. Sheng, M. Govoni, B. Huang, and G. Galli. Quantum embedding theories to simulate condensed systems on quantum computers. Nat. Comput. Sci., 2(7):424–432, 2022.

[313] L. K. Wagner and D. M. Ceperley. Discovering correlated fermions using quantum monte carlo. Rep. Prog. Phys., 79(9):094501, aug 2016.

[314] M. Wallerberger, S. Badr, S. Hoshino, S. Huber, F. Kakizawa, T. Koretsune, Y. Nagai, K. Nogaki, T. Nomoto, H. Mori, J. Otsuki, S. Ozaki, T. Plaikner, R. Sakurai, C. Vogel, N. Witt, K. Yoshimi, and H. Shinaoka. sparse-ir: Optimal compression and sparse sampling of many-body propagators. SoftwareX, 21:101266, 2023.

[315] M. Wallerberger, A. Hausoel, P. Gunacker, A. Kowalski, N. Parragh, F. Goth, K. Held, and G. Sangiovanni. W2dynamics: Local one- and two-particle quantities from dynamical mean field theory. Comput. Phys. Commun., 235:388–399, Feb. 2019.

[316] M. Wallerberger, H. Shinaoka, and A. Kauch. Solving the Bethe-Salpeter equation with exponential convergence. Phys. Rev. Res., 3:033168, 2021.

[317] B. Wang, K. R. Yang, X. Xu, M. Isegawa, H. R. Leverentz, and D. G. Truhlar. Quantum mechanical fragment methods based on partitioning atoms or partitioning coordinates. Acc. Chem. Res., 47(9):2731–2738, Sept. 2014.

[318] T. Wang, X. Cai, K. Chen, B. V. Svistunov, and N. V. Prokof'ev. On the origin of Coulomb pseudopotential: Two wrongs make a "right". arXiv:2207.05238, 2022.

[319] T. Wang, T. Nomoto, Y. Nomura, H. Shinaoka, J. Otsuki, T. Koretsune, and R. Arita. Efficient ab initio Migdal-Eliashberg calculation considering the retardation effect in phonon-mediated superconductors. Phys. Rev. B, 102:134503, 2020.

[320] C. Weber, D. J. Cole, D. D. O'Regan, and M. C. Payne. Renormalization of myoglobin–ligand binding energetics by quantum many-body effects. Proc. Natl. Acad. Sci. USA, 111(16):5790–5795, Apr. 2014.

[321] C. Weber, D. D. O'Regan, N. D. M. Hine, P. B. Littlewood, G. Kotliar, and M. C. Payne. Importance of many-body effects in the kernel of hemoglobin for ligand binding. Phys. Rev. Lett., 110(10):106402, Mar. 2013.

[322] J. R. Weber, W. F. Koehl, J. B. Varley, A. Janotti, B. B. Buckley, C. G. V. de Walle, and D. D. Awschalom. Quantum computing with defects. Proc. Natl. Acad. Sci. USA, 107(19):8513–8518, May 2010.

[323] D. Wecker, B. Bauer, B. K. Clark, M. B. Hastings, and M. Troyer. Gate-count estimates for performing quantum chemistry on small quantum computers. Phys. Rev. A, 90(2):022305, Aug. 2014.

[324] D. Wecker, M. B. Hastings, N. Wiebe, B. K. Clark, C. Nayak, and M. Troyer. Solving strongly correlated electron models on a quantum computer. Phys. Rev. A, 92(6):062318, Dec. 2015.

[325] P. Werner and M. Casula. Dynamical screening in correlated electron systems—from lattice models to realistic materials. J. Phys. Condens. Matter, 28(38):383001, July 2016.

[326] P. Werner and A. J. Millis. Efficient dynamical mean field simulation of the Holstein-Hubbard Model. Phys. Rev. Lett., 99(14):146404, Oct. 2007.

[327] P. Werner and A. J. Millis. Dynamical screening in correlated electron materials. Phys. Rev. Lett., 104(14):146401, Apr. 2010.

[328] T. A. Wesolowski, S. Shedge, and X. Zhou. Frozen-density embedding strategy for multilevel simulations of electronic structure. Chem. Rev., 115(12):5891–5928, June 2015.

[329] S. R. White. Density matrix formulation for quantum renormalization groups. Phys. Rev. Lett., 69(19):2863–2866, 1992.

[330] S. R. White. Density-matrix algorithms for quantum renormalization groups. Phys. Rev. B, 48(14):10345–10356, 1993.

[331] H. F. Wilson, F. Gygi, and G. Galli. Efficient iterative method for calculations of dielectric matrices. Phys. Rev. B, 78(11):113303, Sept. 2008.

[332] H. F. Wilson, F. Gygi, and G. Galli. Efficient iterative method for calculations of dielectric matrices. Phys. Rev. B, 78(11):113303, Sept. 2008.

[333] N. Wiser. Dielectric constant with local field effects included. Phys. Rev., 129(1):62–69, January 1963.

[334] G. Wolfowicz, F. J. Heremans, C. P. Anderson, S. Kanai, H. Seo, A. Gali, G. Galli, and D. D. Awschalom. Quantum guidelines for solid-state spin defects. Nat. Rev. Mater., pages 1–20, Apr. 2021.

[335] S. Wouters, C. A. Jiménez-Hoyos, Q. Sun, and G. K.-L. Chan. A practical guide to density matrix embedding theory in quantum chemistry. J. Chem. Theory Comput., 12(6):2706–2719, June 2016.

[336] S. Xu and E. A. Carter. Theoretical insights into heterogeneous (photo)electrochemical CO_2 reduction. Chem. Rev., 119(11):6631–6669, June 2019.

[337] Y. Yao, F. Zhang, C.-Z. Wang, K.-M. Ho, and P. P. Orth. Gutzwiller hybrid quantum-classical computing approach for correlated materials. Phys. Rev. Res., 3(1):013184, Feb. 2021.

[338] C.-N. Yeh, S. Iskakov, D. Zgid, and E. Gull. Fully self-consistent finite-temperature GW in Gaussian Bloch orbitals for solids. arXiv:2206.07660, 2022.

[339] C.-N. Yeh, A. Shee, S. Iskakov, and D. Zgid. Testing the Green's function coupled cluster singles and doubles impurity solver on real materials within the framework of self-energy embedding theory. Phys. Rev. B, 103(15):155158, Apr. 2021.

[340] X. Yuan. A quantum-computing advantage for chemistry. Science, 369(6507):1054–1055, Aug. 2020.

[341] D. Zgid and G. K.-L. Chan. Dynamical mean-field theory from a quantum chemical perspective. J. Chem. Phys., 134(9):094115, Mar. 2011.

[342] D. Zgid and E. Gull. Finite temperature quantum embedding theories for correlated systems. New. J. Phys., 19(2):023047, Feb. 2017.

[343] I. Y. Zhang and A. Grüneis. Coupled Cluster Theory in Materials Science. Front. Mater., 6, 2019.

[344] Z.-H. Zhang, P. Stevenson, G. Thiering, B. C. Rose, D. Huang, A. M. Edmonds, M. L. Markham, S. A. Lyon, A. Gali, and N. P. de Leon. Optically Detected Magnetic Resonance in Neutral Silicon Vacancy Centers in Diamond via Bound Exciton States. Phys. Rev. Lett., 125(23):237402, Nov. 2020.

[345] H. Zheng, M. Govoni, and G. Galli. Dielectric-dependent hybrid functionals for heterogeneous materials. Phys. Rev. Mater., 3:073803, Jul 2019.

[346] Y. Zhou, K. Kanoda, and T.-K. Ng. Quantum spin liquid states. Rev. Mod. Phys., 89(2):025003, 2017.

[347] T. Zhu, Z.-H. Cui, and G. K.-L. Chan. Efficient formulation of ab initio quantum embedding in periodic systems: Dynamical mean-field theory. J. Chem. Theory Comput., 16(1):141–153, Jan. 2020.

[348] T. Zhu, C. A. Jiménez-Hoyos, J. McClain, T. C. Berkelbach, and G. K.-L. Chan. Coupled-cluster impurity solvers for dynamical mean-field theory. Phys. Rev. B, 100(11):115154, Sept. 2019.

[349] A. S. Zyubin, A. M. Mebel, M. Hayashi, H. C. Chang, and S. H. Lin. Quantum chemical modeling of photoadsorption properties of the nitrogen-vacancy point defect in diamond. J. Comput. Chem., 30(1):119–131, 2009.